Alma Mater Studiorum – Università di Bologna

School of Science
Department of Physics and Astronomy
Master Degree Programme in Astrophysics and Cosmology

Modelling 3D galactic gaseous discs with non-isothermal vertical distributions

Graduation Thesis

Presented by:
Cristina Caprioglio

Supervisor:
Chiar.mo Prof. Carlo Nipoti

Co-supervisor:
Dott. Giuliano Iorio

Academic year 2024-2025
Graduation date V

Contents

1 Introduction **1**

1.1 Thickness of gaseous discs . . . 1

1.2 Local Gravitational Instability . . . 2

1.3 The role of the vertical structure . . . 5

1.4 This thesis . . . 6

2 The physical model **9**

2.1 The fluid equations for isotropic systems . . . 9

2.2 The density vertical profile . . . 11

2.3 The gravitational potential . . . 12

2.4 A simplified model: the barotropic distirbution . . . 13

2.5 Rotational and convective stability . . . 14

2.5.1 The Schwarzschild criterion . . . 15

2.5.2 The Solberg-Høiland criterion . . . 16

2.6 The Boltzmann-Jeans equations . . . 17

2.6.1 The equations for axisymmetric systems . . . 17

2.6.2 Systems with $f = f(H, L_z)$ . . . 18

3 The numerical method **19**

3.1 The starting point: `galpynamics` . . . 19

3.1.1 Iterative estimation of the 3D gas distribution . . . 20

3.2 A method to account for $\sigma = \sigma(R, z)$ . . . 22

4 Illustrative models **25**

4.1 The profiles of the mass components . . . 25

4.1.1 The DM halo . . . 25

4.1.2 The stellar disc . . . 26
4.1.3 The bulge . . . 26
4.1.4 The gas density . . . 26
4.1.5 The gas velocity dispersion . . . 26
4.2 Illustrative model I . . . 27
4.2.1 Results for case IC . . . 29
4.2.2 Results for case IR . . . 34
4.3 Illustrative model II . . . 38
4.3.1 Results for case IIC . . . 41
4.3.2 Results for case IIR . . . 45

5 The Milky Way 50
5.1 The method and the model . . . 50
5.1.1 The gas distribution and kinematics by Marasco et al. (2017) . . . 50
5.1.2 Data analysis and method of Kalberla et al. (2007) . . . 51
5.2 The galaxy model . . . 54
5.2.1 The dynamical model . . . 54
5.2.2 The gas velocity dispersion . . . 57
5.3 Our method and models . . . 59
5.4 Results . . . 63
5.4.1 Case A . . . 63
5.4.2 Case B . . . 70
5.4.3 Case C . . . 77
5.4.4 Case D . . . 84
5.5 Discussion . . . 91
5.5.1 The density profile and the disc scale-height . . . 91
5.5.2 The mass discarded: the comparison with Kalberla et al. (2007) . . . 92
5.5.3 The $h(R)$ profile: our models vs the ones by Kalberla et al. (2007) . . . 92
5.5.4 The vertical Brunt-Väisäla frequency . . . 93

6 Summary and conclusions 94

A The best choice to find the vertical density profile 104
A.1 First test: numerical errors on the integration by parts . . . 105

A.2 What is the best method? 107

Abstract

The vertical structure of galactic gaseous discs plays a relevant role in various astrophysical contexts. For example, it is essential to study Local Gravitational Instability (LGI), since, at a given surface density, the conditions for disc fragmentation depend on the disc vertical stratification. Moreover, the 3D density of the gaseous disc has a fundamental correlation with star formation. For simplicity, the disc can be assumed to be thin, but it has been shown that this approximation is rarely justified, and it may lead to bias in the study of the dynamics and kinematics of galaxies; for instance, it has been shown that not taking into account the vertical extent of the disc may lead to bias in the fit of rotation curves and the estimate of the dark matter (DM) mass. Observing the vertical structure is, however, difficult, as it can only be done for edge-on galaxies and the Milky Way. An alternative method to study these structures is thus realizing theoretical models. In order to take into account the vertical extent of the disc, more self-consistent models based on the assumption of vertical hydrostatic equilibrium have been developed, but they usually assume a vertical isothermal distribution. In this thesis project I model thick discs with a generic non-isothermal vertical distribution (i.e. with a velocity dispersion $\sigma = \sigma(R, z)$ as a function of the Galactic cylindrical radius, R, and height with respect to the midplane of the disc, z). I derive the theoretical formalism for these generic models, and developed a numerical approach that can be used to explore gas discs with a generic radial and vertical velocity dispersion profile. Aside from the vertical density profile and the disc scale-height, I present the vertical pressure profile and the vertical Brunt-Väisäla frequency of our models.

I first show two illustrative models, to show the effects that arise when using a velocity dispersion that depends on z. I find that using a $\sigma(R, z)$ that decreases along the vertical axis can cause the peak of the vertical density profile to shift from $z = 0$, as well as result in negative values of the vertical Brunt-Väisäla frequency squared at large radii, which may lead to the violation of the Solberg-Høiland stability criterion.

Finally, I model the vertical distribution of the Hi disc of our galaxy, the Milky Way; I show a total of 16 models, combining 4 different radial profiles with 4 different vertical profiles for the velocity dispersion. I then compare the profiles I obtain for the disc scale-height to the observed $h(R)$ profile shown in Kalberla et al. (2007), and I find that I can reproduce the $h(R)$ profile up to $R \approx 22$ kpc without the need of a DM ring, which was the solution adopted by Kalberla et al. (2007). However, the only way I manage to match the sharp increase in the flaring for larger radii is by using a radial profile for σ only partially based on observational constraints, as I need a radial velocity dispersion that increases for $R \geq 22$ kpc.

Chapter 1

Introduction

In this chapter we introduce the background and aim of this thesis, which is the modelling of galactic gaseous discs. In Section 1.1 we discuss the thin-disc approximation, and the challenges that come with observing the vertical structure of galactic gaseous discs, and we discuss the requirements to build accurate theoretical models. In Section 1.2 we introduce the concept of local gravitational instability and its relevance in gaseous discs. In Section 1.3 we present the relevance of the disc vertical structure in different contexts. Finally, in Section 1.4 we explain the aim and the structure of this thesis.

1.1 Thickness of gaseous discs

From protostellar discs to accretion discs, rotating gaseous discs are common astrophysical systems that exist on a broad range of scales. When modelling discs, a way to simplify the calculations is assuming the disc is thin (see for example Mestel, 1963; Schmitz, 1988)[1], however the approximation of thin disc is rarely justified, both in protostellar discs, where the vertical extent can be substantial (Law et al., 2022), and in gaseous discs of present-day galaxies (Yim et al., 2014), as shown in Fig. 1.1. Realizing accurate theoretical models is important, as observing the vertical density distribution is difficult, as it can be done only for edge-on galaxies and the Milky Way. Moreover, in both cases we still have additional complications, with projection effects contaminating the measurements due to line-of-sight-integration. These observations can also be "model-dependent", especially when studying the Milky Way, as it is usually required to assume a

[1] In both these works, they assume the disc to be infinitely (or razor) thin, so the vertical structure is essentially modelled as a Dirac delta.

rotational curve to obtain the volume density from the sky emission. Theoretical models are thus an alternative method to study these structures, but in order to obtain accurate models of the vertical structure of galactic discs accurate measurements of the gas distribution and kinematics are still required. Often, a constant velocity dispersion σ is assumed (see Aditya, 2023; Mancera Piña et al., 2021; Romeo, 2020), but this is hardly the case, as σ usually decreases with increasing R (e.g. Lelli et al., 2021; Rizzo et al., 2023). Bacchini et al. (2024) derives the vertical structure considering a $\sigma = \sigma(R)$ described by the following profile:

$$\sigma(R) = \sigma_0 \exp\left(-\frac{R}{R_\sigma}\right), \tag{1.1.1}$$

with σ_0 being the gas velocity dispersion at the galaxy centre and with R_σ being a scale radius. These parameters are obtained by fitting Eq. (1.1.1) to the radial profile of the gas velocity dispersion measured from observations.

In addition to the velocity dispersion we need the total gravitational potential of the galaxy $\Phi_{\rm tot}$: this is because one of the fundamental assumptions needed to realize models is the one of vertical hydrostatic equilibrium, which we expect to be true at large scales, as we would otherwise observe large scale motions. Determining $\Phi_{\rm tot}$ is no trivial matter, since it includes not only the potentials of the DM halo and stellar components, but also the gas potential Φ, which, however, depends on the gas distribution itself (we explain this in detail in Section 2.3). To bypass this problem, one can use an iterative method that accounts for the self-gravity of the disc. The total galactic potential is then used to estimate the gas density $\rho = \rho(R, z)$, and from the vertical density profile the disc scale height can be found.

1.2 Local Gravitational Instability

Local gravitational instability (LGI) is a crucial topic in galaxy and star formation; for example, a galactic disc susceptible to LGI could fragment in gas clumps and eventually lead to star formation (see section 8.3 Cimatti, Fraternali, and Nipoti, 2019), while in protostellar discs LGI can contribute directly or indirectly to planet formation (Kratter and Lodato, 2016).

Moreover, observational works (e.g. Fujimoto et al., 2024) have shown that at high redshifts galaxies often host unstable gas discs, and a similar behaviour is found for starburst galaxies (Fisher et al., 2022), their present-day counterpart, thus making LGI a fundamental mechanism for regulating star formation and gas turbulence when looking at galaxy discs at cosmological distances.

Instability criteria for infinitesimally thin discs have been amply studied: in Toomre (1964), a

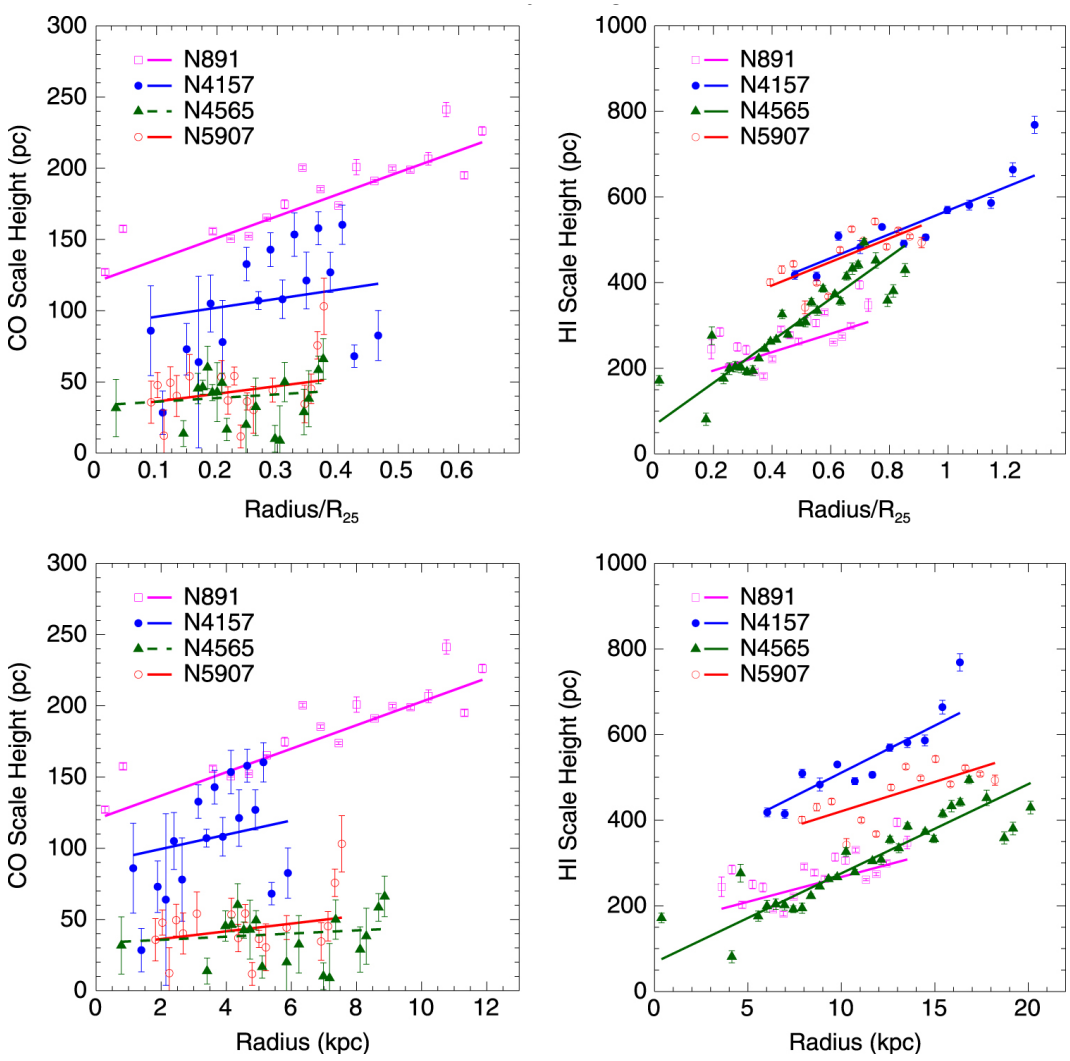

Figure 1.1: Scale height plots of 4 edge-on spiral galaxies by Yim et al. (2014). Top row: scale heights plotted against radius normalized by the optical radius (R_{25}) for CO (left) and HI (right). Bottom row: scale heights plotted against radius in units of kpc for CO and HI. The lines show linear approximations obtained by least-squares fitting.

criterion based on the dimensionless parameter Q is presented, with $Q = (c_s\kappa)/(\pi G\Sigma) < 1$ being a sufficient condition for instability, where c_s is the sound speed, κ is the epicyclic frequency, and Σ is the surface density. However, as we discussed in Section 1.1, the approximation of thin disc is rarely justified. Different authors have tackled the problem of gravitational instability in the case of non-razor-thin discs, obtaining 3D instability criteria that were essentially a modified Q-based criterion that could account for finite thickness (Behrendt et al., 2015; Romeo et al., 2013; Wang et al., 2010). Others have studied specific cases of 3D systems: Bertin et al. (1982) considered homogenous rotating slabs of finite thickness, while Goldreich and Lynden-Bell (1965a,b) assumed a polytropic equation of state with specific values of the polytropic index (see also Meidt, 2022). Similarly, Mamatsashvili and Rice (2010) studied 3D models of discs with polytropic vertical structure and Keplerian rotation. Recently, Nipoti (2023) proposed a 3D instability criterion which can be applied to stratified rotating discs. Similarly to the Toomre criterion, this one is also based on a dimensionless parameter called Q_{3D}, and it gives us a sufficient condition for instability defined by $Q_{3D} < 1$, with

$$Q_{3D} \equiv \frac{\sqrt{\kappa^2 + \nu^2} + c_s + h_z^{-1}}{\sqrt{4\pi G\rho}}, \tag{1.2.1}$$

where ρ is the volume density of the gas disc, h_z is the disc thickness, and ν is a frequency defined by $\nu^2 \equiv (\rho'_z p'_z)/\rho^2$, where $X'_z \equiv \frac{\partial X}{\partial z}$, with z being the coordinate perpendicular to the equatorial plane. This work has already been extended to two-component discs and the criterion was applied to one-component self-gravitating discs with polytropic vertical distributions in Nipoti et al. (2024); moreover, Bacchini et al. (2024) applied the Q_{3D}-based criterion to a sample of 44 star-forming galaxies in the redshift interval $0 \lesssim z \lesssim 5$, all of which are hosting a rotating disc of cold gas. In the aforementioned work, there is a comparison between the results obtained using the classical Toomre criterion and the ones found using the 3D criterion, and the differences are evident. As shown in Fig. 1.2, applying the Q criterion they find 10 unstable systems, however, according to the 3D criterion, for two of the galaxies with $Q < 1$ there is no evidence of instability, and in general the unstable regions are 20% smaller.

The result highlights that the vertical structure of the disc thus plays an important role in the stability of the system.

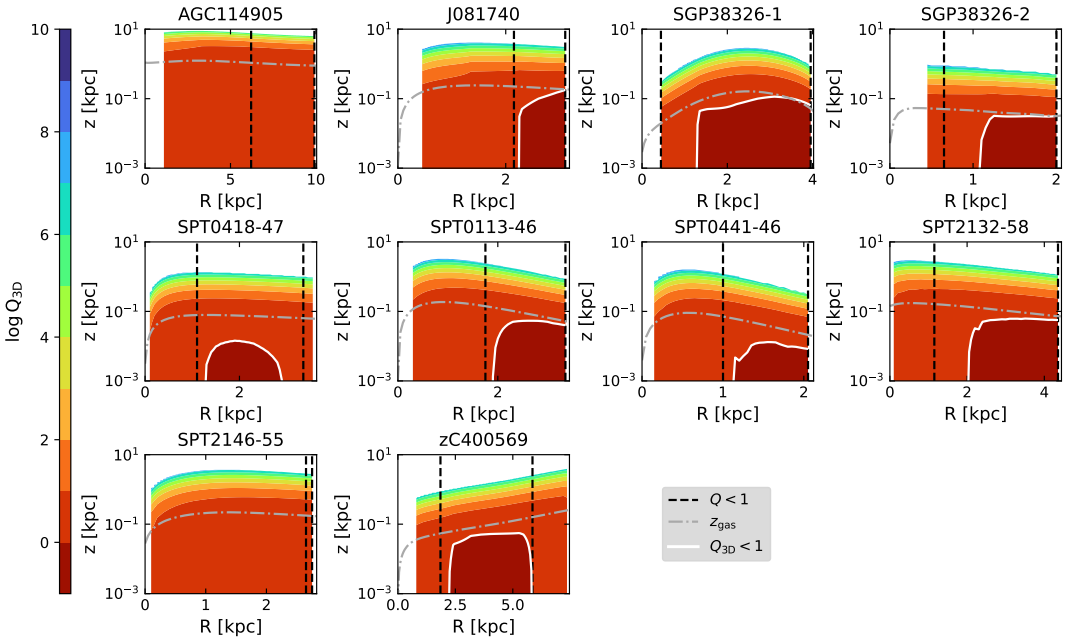

Figure 1.2: Maps of $Q_{3D}(R, z)$ (with R and z being, respectively, the coordinate parallel and perpendicular to the equatorial plane) for the galaxies in the sample of Bacchini et al. (2024) having gravitationally unstable regions (delimited by the black dashed lines) according to the Q criterion. The white contour encompasses the region that is locally unstable when the Q_{3D} criterion is adopted. The gray dash-dotted curve represents the gas disc scale height z_{gas}. This picture was taken from Bacchini et al. (2024).

1.3 The role of the vertical structure

In addition to the role played in setting the disc instability, the vertical structure of gaseous discs is relevant also in other contexts: for example, Bacchini et al. (2019) shows the correlation between star formation and the 3D density is more fundamental than the more common one with the surface density (see Kennicutt, 1998). This suggests a fundamental role of the vertical gas distribution in determining the star formation. Mancera Piña et al. (2022) discusses how not taking the disc vertical structure into consideration can create some bias in the fit of the rotation curves, and, as a consequence, on the study of dynamics of disc galaxies (see Fig. 1.3). Aside from the rotation curve of the gas, we can see in Fig. 1.3 that including the 3D structure of the disc has an impact on the rotation curve of the dark matter (DM), showing that a flared disc allows for a more massive DM halo. The amount of DM present in a galaxy is a crucial quantity that is connected to various scaling relations, such as the star-to-halo mass relation, the baryonic-to-halo mass relation, and

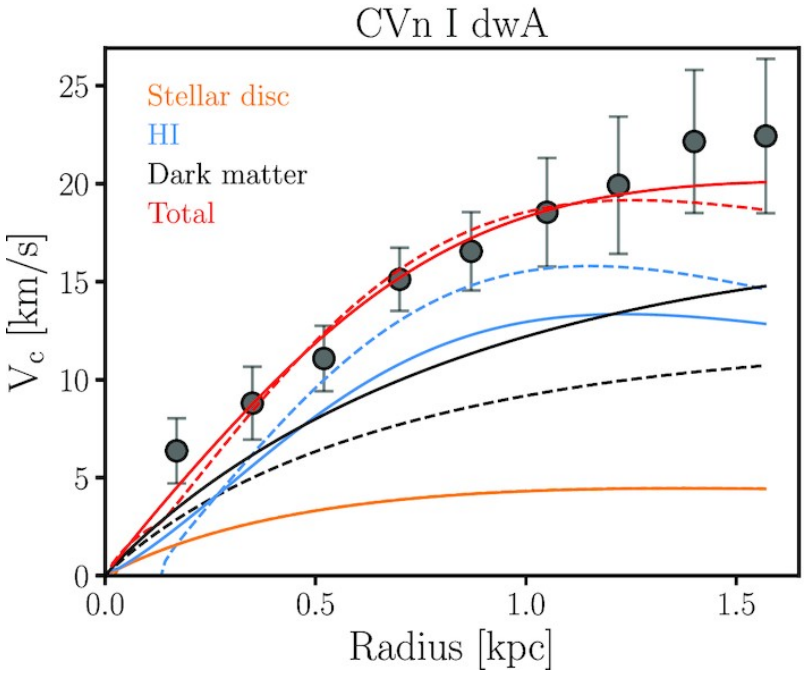

Figure 1.3: From Mancera Piña et al. (2022): mass model of the dwarf galaxy CVn I dwA. The solid (dashed) lines show the mass model when a thick (razor-thin) HI disc is used. The large effect of the vertical structure of the disc on the mass model is clear, especially for the black and blue curves.

the concentration-mass relation, which are revisited in Mancera Piña et al. (2022), and assuming a thin disc may cause some bias in the estimate of the DM mass. This is especially relevant for Dwarf Galaxies, as they are dark matter-dominated.

1.4 This thesis

Classically, discs are either assumed to be thin or with a constant scale-height, however this may lead to bias in the interpretation of the gas dynamics and kinematics. As explained in the previous sections, there are works where the disc thickness is taken into account, usually coupled with the assumption of a radial and vertical isothermal distribution, but models with non-isothermal radial distributions, i.e. with σ dependent on the radial coordinate R, have also been studied (see for instance Afruni et al., 2025; Bacchini et al., 2019). However a vertical isothermal distribution is still usually assumed. This may lead to bias in the estimate of the scale height, which, as we have illustrated in Section 1.3, plays a relevant role in different contexts. For instance, for

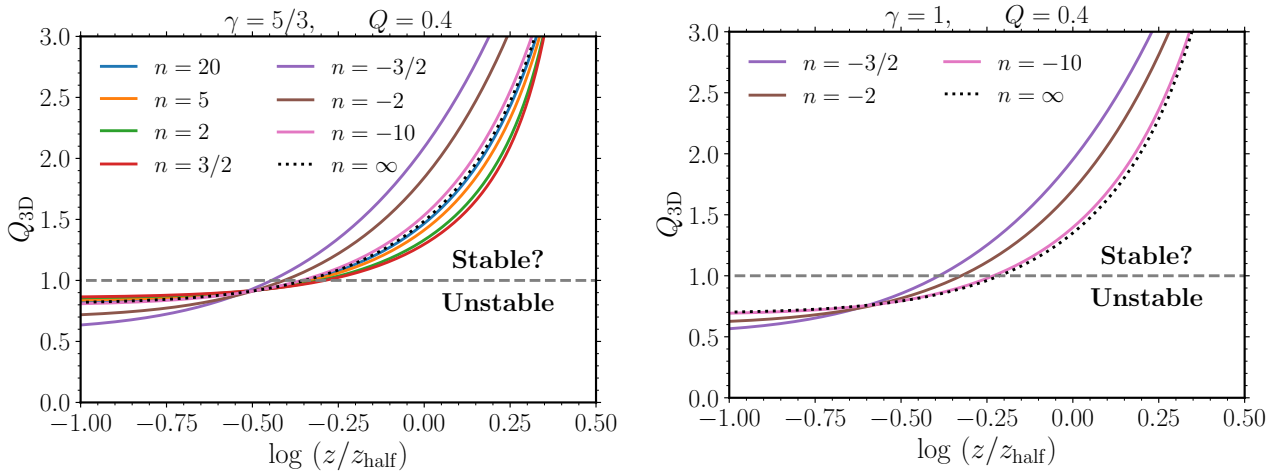

(a) (b)

Figure 1.4: From Nipoti et al. (2024): vertical profiles of the local gravitational instability parameter, Q_{3D}, at a given radius R for discs with polytropic vertical density distributions assuming $Q = 0.4$, when $\gamma = 5/3$ (left panel) or $\gamma = 1$ (right panel). In each panel, the selected values of the polytropic index n are such that the distribution is convectively stable for the assumed adiabatic exponent γ. The case $n = \pm\infty$ is the self gravitating isothermal slab, for which $Q_{3D}(z)$ is analytic. The horizontal dashed line indicates the instability threshold, $Q_{3D} = 1$. The question mark in "Stable?" is used to point out that $Q_{3D} < 1$ is a sufficient condition for instability, so stability is possible but not guaranteed when $Q_{3D} > 1$.

unstable discs, it may lead to an underestimation of the local gravitational instability region. In Nipoti et al. (2024) it is shown that for a fluid with a generic polytropic vertical distribution the instability region grows with the polytropic index n when $0 \leq n < +\infty$, while the opposite is true for $-1 < n < -\infty$, as shown in Fig. 1.4. In general, the profile of the velocity dispersion influences the density and the disc scale height, and it also plays a role in the convective and rotational instability. It is thus fundamental to derive more flexible models, which would allow to explore the influence of the vertical profile of the velocity dispersion. In this thesis, we aim to study the vertical structure of galactic disc models with a generic non-isothermal vertical distribution, allowing the velocity dispersion to vary with both R and z. We first present our physical model in Chapter 2, introducing the equations that we use to determine both the density and the potential, and we also briefly discuss the stability of our system according to the Solberg-Høiland criterion. In Chapter 3 we present the approach we use to build our models, using a Python code based on `galpynamics` (Iorio, 2018), which can create flexible models with a generic velocity dispersion

$\sigma(R, z)$. Then, in Chapter 4 we build models of mock disc galaxies to show the effect of assuming a velocity dispersion not constant along z. Finally, in Chapter 5 we study the vertical structure of the HI disc of the Milky Way, and try to reproduce its $h(R)$ profile, checking how much the velocity dispersion profile, both radial and vertical, can influence the structure, and we compare our results to the ones present in the literature.

Chapter 2

The physical model

In this chapter, we present the equations we use to describe the gaseous discs of galaxies. In Section 2.1, we illustrate the assumptions behind our treatment, and define the relations between the pressure, the density, the velocity dispersion, and the gravitational potential. In Section 2.2, we retrieve the formula we use to calculate the vertical density profile, while in Section 2.3 we describe how to find the gravitational potential for each component of a galaxy. In Section 2.4 we present the conditions required to have a barotropic distribution. In Section 2.5 we briefly introduce the criteria for convective and rotational stability, and finally in Section 2.6 we show how to recover the equations presented in Section 2.1 starting from the distribution function.

2.1 The fluid equations for isotropic systems

In this work, we use cylindrical coordinates $(R,\, \phi,\, z)$ as our coordinate system, where R and z are the distances perpendicular to and parallel to the longitudinal axis, while ϕ is the azimuthal coordinate. We assume our fluid is in vertical hydrostatic equilibrium, and is axisymmetric and in a steady state; that is, all the derivatives with respect to ϕ and t are null. Under all these assumptions, our model is described by

$$\begin{cases} \dfrac{\partial P}{\partial z} = -\rho \dfrac{\partial \Phi}{\partial z}, & \text{(2.1.1a)} \\ \dfrac{\partial P}{\partial R} = -\rho \dfrac{\partial \Phi}{\partial R} + \dfrac{\rho}{R} \bar{v}_\phi^2, & \text{(2.1.1b)} \end{cases}$$

where $\rho = \rho(R, z)$ is the density, $P = P(R, z)$ is the pressure, $\Phi = \Phi(R, z)$ is the total gravitational potential, and $\bar{v}_\phi(R, z) = R\Omega(R, z)$ is the average azimuthal velocity, with $\Omega = \Omega(R, z)$ being the

angular velocity. In Section 2.6, we explain in detail how we find the system of equations (2.1.1), giving a more generic description.

From the system of equations (2.1.1), we can derive a useful relation that we can use to determine whether our system is barotropic. First, we differentiate Eq. (2.1.1a) with respect to z and Eq. (2.1.1b) with respect to R, obtaining

$$\begin{cases} -\frac{1}{\rho^2}\frac{\partial P}{\partial R}\frac{\partial \rho}{\partial z} + \frac{1}{\rho}\frac{\partial^2 P}{\partial R \partial z} = \frac{1}{R}\frac{\partial \bar{v}_\phi^2}{\partial z} - \frac{\partial^2 \Phi}{\partial R \partial z}, & \text{(2.1.2a)} \\ -\frac{1}{\rho^2}\frac{\partial P}{\partial z}\frac{\partial \rho}{\partial R} + \frac{1}{\rho}\frac{\partial^2 P}{\partial R \partial z} = -\frac{\partial^2 \Phi}{\partial R \partial z}. & \text{(2.1.2b)} \end{cases}$$

Then, subtracting Eq. (2.1.2b) from Eq. (2.1.2a) and using $\bar{v}_\phi = \Omega R$ we get:

$$R\frac{\partial \Omega^2}{\partial z} = \frac{1}{\rho^2}\left(\frac{\partial P}{\partial z}\frac{\partial \rho}{\partial R} - \frac{\partial P}{\partial R}\frac{\partial \rho}{\partial z}\right). \tag{2.1.3}$$

From the Poincarè-Wavre theorem (see Tassoul (1978)), $\Omega = \Omega(R)$ is a necessary and sufficient condition to have a barotropic fluid, and this is equivalent to requiring that Ω has no variation along z, that is, that the r.h.s of Eq. (2.1.3) is equal to zero.

We now introduce the velocity dispersion by defining the pressure of the fluid as $P \equiv \sigma^2 \rho$, with ρ being the density of the gas, and σ being the velocity dispersion. We use this definition because the pressure is essentially a combination of both thermal and turbulent pressure, so the velocity dispersion contains both the thermal speed and the turbulent velocity dispersion. We assume an isotropic velocity dispersion that depends on both the radial and vertical coordinates, that is $\sigma = \sigma_z = \sigma_R = \sigma_\phi = \sigma(R, z)$, and then substitute P with its definition in the system of equations (2.1.1), obtaining

$$\begin{cases} \frac{\partial(\rho(R,z)\sigma^2(R,z))}{\partial z} = -\rho(R,z)\frac{\partial \Phi(R,z)}{\partial z}, & \text{(2.1.4a)} \\ \frac{\partial(\rho(R,z)\sigma^2(R,z))}{\partial R} = -\rho(R,z)\frac{\partial \Phi(R,z)}{\partial R} + \frac{\rho(R,z)}{R}\bar{v}_\phi^2(R,z). & \text{(2.1.4b)} \end{cases}$$

2.2 The density vertical profile

When the velocity dispersion depends on the vertical coordinate, Eq. (2.1.4a) can be integrated as follows:

$$\frac{1}{\rho}\frac{\partial \rho\sigma^2}{\partial z} = -\frac{\partial \Phi}{\partial z}, \tag{2.2.1a}$$

$$\frac{\partial \ln \rho}{\partial z} = -\frac{\partial \ln \sigma^2}{\partial z} - \frac{1}{\sigma^2}\frac{\partial \Phi}{\partial z}, \tag{2.2.1b}$$

$$\int \mathrm{d}\ln\rho = -\int \mathrm{d}\ln\sigma^2 - \int \frac{1}{\sigma^2}\frac{\partial\Phi}{\partial z}\,\mathrm{d}z', \tag{2.2.1c}$$

$$\ln\frac{\rho(R,z)}{\rho(R,0)} = -\ln\frac{\sigma^2(R,z)}{\sigma^2(R,0)} - \int_0^z \frac{1}{\sigma^2}\frac{\partial\Phi}{\partial z}\,\mathrm{d}z', \tag{2.2.1d}$$

with $\rho(R,0)$, $\sigma(R,0)$ and $\Phi(R,0)$ being, respectively, the gas volume density, the gas velocity dispersion and the total gravitational potential evaluated in the midplane. In general, the integral (where, in the integrand, $\sigma = \sigma(R,z)$ and $\Phi = \Phi(R,z)$) in Eq. (2.2.1d) cannot be solved analytically because the potential is usually not known and needs to be calculated iteratively. We explain the reason for this in detail in Section 2.3. One might integrate the integral in Eq. (2.2.1d) by parts[1] in order to obtain an expression that does not depend on the derivative of Φ.

The integration by parts gives

$$\int_0^z \frac{1}{\sigma^2}\frac{\partial\Phi}{\partial z}\,\mathrm{d}z' = \frac{\Phi(R,z)}{\sigma^2(R,z)} - \frac{\Phi(R,0)}{\sigma^2(R,0)} + \int_0^z \frac{2\Phi}{\sigma^3}\frac{\partial\sigma}{\partial z}\,\mathrm{d}z'. \tag{2.2.2}$$

Substituting Eq. (2.2.2) in Eq. (2.2.1d) and taking the exponential of both sides of the equation, we finally obtain an expression for the vertical density profile

$$\rho(R,z) = \rho(R,0)\left(\frac{\sigma^2(R,0)}{\sigma^2(R,z)}\right)\exp\left\{-\frac{\Phi(R,z)}{\sigma^2(R,z)} + \frac{\Phi(R,0)}{\sigma^2(R,0)}\right\}\exp\left\{-\int_0^z \frac{2\Phi}{\sigma^3}\frac{\partial\sigma}{\partial z}\,\mathrm{d}z\right\}. \tag{2.2.3}$$

We can then add and subtract $\frac{\Phi(R,z)}{\sigma^2(R,0)}$ from the first exponent to retrieve the following relation:

$$\begin{aligned}\rho(R,z) = \rho(R,0)\exp\left\{-\frac{\Phi(R,z)-\Phi(R,0)}{\sigma^2(R,0)}\right\}\times \\ \times\left(\frac{\sigma^2(R,0)}{\sigma^2(R,z)}\right)\exp\left\{\Phi(R,z)\frac{\sigma^2(R,z)-\sigma^2(R,0)}{\sigma^2(R,z)\sigma^2(R,0)} - \int_0^z \frac{2\Phi}{\sigma^3}\frac{\partial\sigma}{\partial z}\,\mathrm{d}z\right\}.\end{aligned} \tag{2.2.4}$$

When assuming $\sigma = \sigma(R)$, Eq. (2.2.4) is reduced to

$$\rho(R,z) = \rho(R,0)\exp\left[-\frac{\Phi_{tot}(R,z)-\Phi_{tot}(R,0)}{\sigma^2(R)}\right], \tag{2.2.5}$$

[1] This is mathematically possible only as long as σ does not equate to zero at any point.

which is the typical expression used to describe the gas vertical distribution (see Bacchini et al., 2024; Olling, 1995).

2.3 The gravitational potential

As stated in Section 2.2, the potential appearing in Eq. (2.2.4) is not known a priori. When we model the disc as isolated, Φ only contains the contribution from its self-gravity. However, a galaxy is a complex system which contains different components, and typically the gaseous disc is not the dominant dynamical component, so we need to consider the influence of different components, such as a DM halo, a bulge or a stellar disc.

In this case, the potential will be the sum of the potentials of each component. For the treatment of spheroidal systems (namely, the halo and the bulge) we use (see Binney and Tremaine (2008, p.89))

$$\Phi(R,z) = -2\pi G \frac{\sqrt{1-e^2}}{e}\left(\psi(\infty)\sin^{-1}e - \int_{\sinh u_m=\sqrt{1-e^2}/e}^{\infty} \psi(m)\frac{\mathrm{d}(\sinh u_m)}{1+\sinh^2 u_m}\right), \tag{2.3.1}$$

where u is an oblate spheroidal coordinate, e is the eccentricity defined as

$$e \equiv \sqrt{1-q^2} \qquad \text{with} \quad q \equiv \frac{c}{a} \equiv \text{axial ratio}, \tag{2.3.2}$$

while m is the elliptical radius defined as

$$m^2 \equiv R^2 + \frac{z^2}{q^2} \tag{2.3.3}$$

and ψ is

$$\psi(m) \equiv \int_0^{m^2} \mathrm{d}m^2\, \rho_{sph}(m^2). \tag{2.3.4}$$

We can simplify Eq. (2.3.1) by defining a new variable of integration

$$\tau \equiv e^2\left[\sinh^2 u_m - \left(\frac{1}{e^2}-1\right)\right], \tag{2.3.5}$$

which gives us

$$\Phi(R,z) = -2\pi G \frac{\sqrt{1-e^2}}{e}\left(\psi(\infty)\sin^{-1}e - \frac{e}{2}\int_0^{\infty} \mathrm{d}\tau\, \frac{\psi(m_\tau)}{(\tau+1)\sqrt{\tau+q^2}}\right), \tag{2.3.6}$$

with

$$m_\tau \equiv \frac{R^2}{\tau+1} + \frac{z^2}{\tau+q^2}. \tag{2.3.7}$$

For the disc components, we follow Cuddeford (1993), and the potential is evaluated as:

$$\Phi(R,z) = -2\pi G \int_0^\infty J_0(Rk) \int_{-\infty}^\infty \exp(-k|z-z'|) \int_0^\infty \rho(R',z') J_0(R'k) R' \,\mathrm{d}R' \,\mathrm{d}z' \,\mathrm{d}k\,, \tag{2.3.8}$$

where J is the Bessel function of the first kind. We can simplify Eq. (2.3.8) by evaluating the k-dependant part of the integral using the relation given by Byrd and Friedman (1954), page 249, Eq. (560.01):

$$\int_0^\infty \exp(-k|z-z'|) J_0(Rk) J_0(R'k) = \frac{1}{\pi\sqrt{RR'}} Q_{-1/2}(\epsilon) = \frac{\sqrt{y}K(\sqrt{y})}{\pi\sqrt{RR'}}, \tag{2.3.9}$$

where Q_γ is the Legendre function of the second kind of degree γ, K is the complete elliptical integral of the first kind, and

$$\epsilon = \frac{R^2 + R'^2 + (z-z')^2}{2RR'}, \tag{2.3.10}$$

which gives us

$$y = \frac{2}{1+\epsilon}. \tag{2.3.11}$$

While Cuddeford (1993) uses the formulation with the Legendre function, we prefer to use the equivalent one with the elliptical integral. Taking this into consideration, the final expression for the (both stellar and gaseous) disc potential is

$$\Phi(R,z) = -\frac{2G}{\sqrt{R}} \int_{-\infty}^\infty \mathrm{d}z' \int_0^\infty \mathrm{d}R' \sqrt{R'z'} K(\sqrt{y}) \rho(R',z'). \tag{2.3.12}$$

From Eq. (2.3.12), we can see that the right-hand term of Eq. (2.2.4) depends on the gas density, thus making Eq. (2.2.4) a differential equation that must be solved numerically, regardless of the velocity dispersion.

To do so, we use an iterative method, where, starting from a guess potential, at each step we evaluate the density from Eq. (2.2.4) considering as the potential for the gas disc the one obtained from the previous density estimate.

2.4 A simplified model: the barotropic distirbution

To simplify the model described by the system of equations (2.1.1), one can require to have a barotropic distribution, i.e. with $P = P(\rho)$ and $\Omega = \Omega(R)$. Since $P = \sigma^2\rho$, using Eq. (2.1.3), it is sufficient to verify that:

$$\frac{\partial\sigma^2}{\partial z}\frac{\partial\rho}{\partial R} - \frac{\partial\sigma^2}{\partial R}\frac{\partial\rho}{\partial z} = 0. \tag{2.4.1}$$

One may find a solution in the form:

$$\sigma(R,z) = \sqrt{h(R,z)}, \tag{2.4.2a}$$

$$\rho(R,z) = Ce^{h(R,z)}, \tag{2.4.2b}$$

with $h(R,z)$ a generic function of R and z.
If one requires the density to be in the form of $\rho(R,z) = f(R)g(z)$, $h(R,z)$ becomes:

$$h(R,z) = \ln(f(R)) + \ln(g(z)); \tag{2.4.3}$$

this, however, implies having a velocity dispersion $\sigma(R,z) \neq m(R)n(z)$, unless either $f(R)$ or $g(z)$ are assumed to be constant.
One of the simplest solutions that can be found is the one where both $f(R)$ and $g(z)$ are exponentials, where we get:

$$\sigma(R,z) = \sqrt{\alpha R + a + \beta|z| + b}, \tag{2.4.4a}$$

$$\rho(R,z) = e^{\alpha R + a} e^{\beta|z|+b}. \tag{2.4.4b}$$

Due to the fact that we want $\sigma \in \mathbb{R}$ for a realistic physical solution, we need to add some constraints on α, a, β and b:

$$\begin{cases} \alpha,\, \beta \in \mathbb{R}, & \text{(2.4.5a)} \\ a + b \geq \max\left\{(-\alpha R_{\text{cut}} - \beta z_{\text{cut}}), 0\right\}, \quad \text{for } 0 \leq R \leq R_{\text{cut}},\, 0 \leq |z| \leq z_{\text{cut}}, & \text{(2.4.5b)} \end{cases}$$

where R_{cut} and z_{cut} are respectively the radius and the height where $\rho(R > R_{\text{cut}}$ or $|z| > z_{\text{cut}}) = 0$.

2.5 Rotational and convective stability

By construction, our fluid is both rotating and stratified. This means it may be subjected to rotational and convective instability. As we showed in Section 2.4, unless certain specific conditions are met, we usually deal with a baroclinic fluid, so $\Omega = \Omega(R,z)$. While a complete stability analysis is beyond the scope of this work, we still want to present two criteria: the Solberg-Høiland criterion, and the Schwarzschild criterion. The reason for this is that, if one analyses closely Eq. (2.1.4a), it is possible to deduce that, if the vertical gradient of the gravitational potential is positive (as it usually is), then the condition for vertical hydrostatic equilibrium is

$$\frac{\sigma^2}{\rho}\frac{\partial \rho}{\partial z} + \frac{\partial \sigma^2}{\partial z} = -\frac{\partial \Phi}{\partial z} < 0. \tag{2.5.1}$$

If $\sigma(R, z)$ has a positive vertical gradient, it is immediate that the vertical gradient of the density needs to always be negative, which is what we normally find when $\sigma = \sigma(R)$. However, if the velocity dispersion has a negative vertical gradient larger than the vertical gradient of the potential, this would require the vertical gradient of the density to be positive to keep the vertical hydrostatic equilibrium, and this may impact the stability of the system.

2.5.1 The Schwarzschild criterion

Let us consider a system depending on two Cartesian coordinates (x, z). We start by assuming an unperturbed fluid which is inviscid and adiabatic, with $\rho_0 = \rho_0(z)$, $P_0 = P_0(z)$, in hydrostatic equilibrium in a gravitational potential $\Phi_0 = \Phi(z)$, where the subscript 0 indicates the unperturbed quantity. We want to study the effect of a small linear adiabatic perturbation, whose self-gravity is ignored. We first consider the effect of a perturbation in the form of a plane wave (so $\propto \exp(i(\mathbf{kx} - \omega t))$) perpendicular to the gravitational field, so with wave vector $\mathbf{k}$ along the x direction (that is, $k_x \neq 0$ and $k_z = 0$). If we perform a linear perturbation analysis, using the Boussinesq approximation (Balbus et al., 2016), we find the following dispersion relation

$$\omega^2 \gamma + \frac{1}{\rho_0} \frac{\partial P_0}{\partial z} \frac{\partial s_0}{\partial z} = 0, \tag{2.5.2}$$

where ω is the plane wave frequency, γ is the adiabatic index, and $s \equiv \ln(P\rho^{-\gamma})$ is the normalized specific entropy. We can rewrite Eq. (2.5.2) as $\omega^2 = N_z^2$, where

$$N_z^2 \equiv -\frac{1}{\rho_0 \gamma} \frac{\partial P_0}{\partial z} \frac{\partial s}{\partial z} \tag{2.5.3}$$

is the vertical Brunt-Väisäla frequency (or buoyancy frequency) squared. If $N_z^2 > 0$, then ω is real and oscillating, so the system is stable, but if $N_z^2 < 0$ we have that ω is imaginary, so there is a growing mode, and the system is unstable. This translates into a condition for stability against convection that is

$$\frac{\partial P_0}{\partial z} \frac{\partial s_0}{\partial z} < 0, \tag{2.5.4}$$

also called the Schwarzschild criterion for stability against convection. For a more general case with $k_z \neq 0$, the dispersion relation simply becomes

$$\omega^2 = \frac{k_x^2}{k^2} N_z^2, \tag{2.5.5}$$

where $k^2 = k_x^2 + k_z^2$. Having $N_z^2 < 0$ is however not enough to properly affirm if we have convective instability in a disc because of the effect of rotation.

2.5.2 The Solberg-Høiland criterion

We now consider the stability of a fluid in equilibrium with an axisymmetric gravitational potential $\Phi = \Phi(R, z)$, which is rotating and has entropy gradients. The unperturbed system has $\rho_0 = \rho_0(R, z)$, $P_0 = P_0(R, z)$, $s_0 = s_0(R, z)$, and $\bar{v}_{\phi,0} = \Omega(R, z)R$. We assume an axisymmetric perturbation, so considering a generic quantity $q = q(R, z, t)$, which describes a property of the fluid, we have it can be written as $q = q_0 + \delta q$, with $\delta q \propto \exp[i(k_R R + k_z z - \omega t)]$. Working once again in the Boussinesq approximation, we infer the Solberg-Høiland stability criterion:

$$\frac{\boldsymbol{\nabla} P_0 \cdot \boldsymbol{\nabla} s_0}{\gamma \rho_0} - \frac{1}{R^3}\frac{\partial \Omega^2 R^4}{\partial R} < 0, \tag{2.5.6}$$

$$\frac{\partial P_0}{\partial z}\left[\frac{\partial \Omega^2 R^4}{\partial R}\frac{\partial s_0}{\partial z} - \frac{\partial \Omega^2 R^4}{\partial z}\frac{\partial s_0}{\partial R}\right] < 0 \quad \text{(for stability)}. \tag{2.5.7}$$

We first want to focus on Eq. (2.5.7): since we require vertical hydrostatic equilibrium, we can expect $\frac{\partial P_0}{\partial z}$ to always be negative. This means that what we really need to check is the content of the square bracket, which we want to have a positive sign. For simplicity, we are assume (as it is usual)

$$\frac{\partial \Omega^2 R^4}{\partial R} > 0. \tag{2.5.8}$$

Having established this, we now want to focus on the other three terms. The simplest case is to have

$$\frac{\partial \Omega^2 R^4}{\partial z}\frac{\partial s_0}{\partial R} < 0; \tag{2.5.9}$$

if this condition is respected, then all we need is for s_0 to have a positive gradient along z and the inequality of Eq. (2.5.7) is respected. Unfortunately, depending on the profile of the velocity dispersion, this might not always be true. As we discussed above, the vertical density gradient can be positive, which can result in a negative gradient for the normalized specific entropy. The quickest way we can check whether this happens is by exploiting Eq. (2.5.2), and verify if the Brunt-Väisäla frequency N_z squared can be negative. If that happens, in order to respect the inequality in Eq. (2.5.7), we need to have

$$\left|\frac{\partial s_0}{\partial R}\right| \gg \left|\frac{\partial s_0}{\partial z}\right| \quad \text{or} \quad \left|\frac{\partial \Omega^2 R^4}{\partial R}\right| \ll \left|\frac{\partial \Omega^2 R^4}{\partial z}\right|. \tag{2.5.10}$$

We have a similar condition if we want to respect the inequality in Eq. (2.5.6), in the sense that we need for it to hold true to have strong radial gradients for the pressure and/or s_0 if $N_z^2 < 0$. However, here we study the vertical structure of the disc, so finding the radial gradients extends

past the scope of this work, so we simply focus on the vertical Brunt-Väisäla frequency. We want to point out that, while Eq. (2.5.8) usually is true, if one wanted to do a full stability analysis it would need to be checked, as we have no information on $\Omega(R, z)$, and $N_z^2 > 0$ is not a sufficient condition for stability for rotating discs.

2.6 The Boltzmann-Jeans equations

We present here a more general case of the systems presented in Section 2.1 by following the approach used in Binney and Tremaine (2008). We refer in particular to Chapter 4, sections 1, 2, and 8.

2.6.1 The equations for axisymmetric systems

When modelling a gaseous disc, we can also work with the distribution function f, which is defined such that $f(\mathbf{x}, \mathbf{v}, t)\, \mathrm{d}^3\mathbf{x}\, \mathrm{d}^3\mathbf{v}$ is the probability of finding a randomly chosen particle at a given time t in the phase-space volume $\mathrm{d}^3\mathbf{x}\, \mathrm{d}^3\mathbf{v}$ around the position $\mathbf{x}$ and velocity $\mathbf{v}$. By assumption all particles are identical, which means that the probability for each is the same. We normalize f such that:

$$\int \mathrm{d}^3\mathbf{x}\, \mathrm{d}^3\mathbf{v}\, f(\mathbf{x}, \mathbf{v}, t) = 1, \tag{2.6.1}$$

where the integral is over the entire phase-space. Moreover, it can be shown that f has the same numerical value at a given point in any canonical coordinate system (see Binney et al., 2008, pg. 275). The equation for the conservation of probability in phase space is the following:

$$\frac{\partial f}{\partial t} + \frac{\partial}{\partial \mathbf{w}}(f\dot{\mathbf{w}}) = 0, \tag{2.6.2}$$

with $\mathbf{w} = (\mathbf{q}, \mathbf{p})$ an arbitral system of canonical coordinates. Using Hamilton's equations, we can simplify Eq. (2.6.2) and obtain the **collisionless Boltzmann equation**:

$$\frac{\partial f}{\partial t} + \dot{\mathbf{q}}\frac{\partial \mathbf{q}}{\partial f} + \dot{\mathbf{p}}\frac{\partial \mathbf{p}}{\partial f} = 0, \tag{2.6.3}$$

which is equivalent to:

$$\frac{\partial f}{\partial t} + [f, H] = 0, \tag{2.6.4}$$

where [...] denotes the Poisson bracket.

In cylindrical coordinates $H = \frac{1}{2}(p_R^2 + p_\phi^2/R^2 + p_z^2) + \Phi$, so if we substitute it in Eq. (2.6.4) we

obtain

$$\frac{\partial f}{\partial t} + p_R \frac{\partial f}{\partial R} + \frac{p_\phi}{R^2}\frac{\partial f}{\partial \phi} + p_z \frac{\partial f}{\partial z} - \left(\frac{\partial \Phi}{\partial R} - \frac{p_\phi^2}{R^3}\right)\frac{\partial f}{\partial p_R} - \frac{\partial \Phi}{\partial \phi}\frac{\partial f}{\partial p_\phi} - \frac{\partial \Phi}{\partial z}\frac{\partial f}{\partial p_z} = 0, \tag{2.6.5}$$

which is the **collisionless Boltzmann equation in cylindrical coordinates**. If we assume our system is axisymmetric and in a steady state, Eq. (2.6.5) becomes

$$p_R \frac{\partial f}{\partial R} + p_z \frac{\partial f}{\partial z} - \left(\frac{\partial \Phi}{\partial R} - \frac{p_\phi^2}{R^3}\right)\frac{\partial f}{\partial p_R} - \frac{\partial \Phi}{\partial z}\frac{\partial f}{\partial p_z} = 0. \tag{2.6.6}$$

Multiplying by either p_R, p_z or p_ϕ and integrating over the momenta $p_R = v_R$, $p_z = v_z$ and $p_\phi = Rv_\phi$, and express them as function of the velocities, we obtain

$$\frac{\partial(\rho\overline{v_R^2})}{\partial R} + \frac{\partial(\rho\overline{v_R v_z})}{\partial z} + \rho\left(\frac{\overline{v_R^2} - \overline{v_\phi^2}}{R}\frac{\partial \Phi}{\partial R}\right) = 0 \tag{2.6.7a}$$

$$\frac{\partial(\rho\overline{v_z^2})}{\partial z} + \frac{1}{R}\frac{\partial(R\rho\overline{v_R v_z})}{\partial R} + \rho\frac{\partial \Phi}{\partial z} = 0 \tag{2.6.7b}$$

$$\frac{\partial(\rho\overline{v_z v_\phi})}{\partial z} + \frac{1}{R^2}\frac{\partial(R^2\rho\overline{v_R v_\phi})}{\partial R} = 0, \tag{2.6.7c}$$

which are the **Jeans equations for axisymmetric systems**. However, without further constraints, these three equations are not closed.

2.6.2 Systems with $f = f(H, L_z)$

When we have a distribution function in the form of $f(H, L_z)$, which means that $\overline{v_R^2} = \overline{v_z^2}$, all mixed moments present in Eqs. (2.6.7a)–(2.6.7c) vanish, and Eq. (2.6.7c) becomes trivial. Defining the velocity dispersion $\sigma(R, z)$ through the relation $\sigma^2(R, z) = \overline{v_R^2}(R, z) = \overline{v_z^2}(R, z)$, our fluid is thus described by the following equations:

$$\begin{cases} \dfrac{\partial(\rho\sigma^2)}{\partial z} = -\rho\dfrac{\partial \Phi}{\partial z}, & \text{(2.6.8a)} \\ \dfrac{\partial(\rho\sigma^2)}{\partial R} = -\rho\dfrac{\partial \Phi}{\partial R} + \dfrac{\rho}{R}\left(\overline{v_\phi^2} - \sigma^2\right), & \text{(2.6.8b)} \end{cases}$$

where $\rho = \rho(R, z)$ is the density of the gas, $\Phi = \Phi(R, z)$ is the total gravitational potential, and $\overline{v_\phi^2} = \bar{v}_\phi^2 + \sigma_\phi^2$ is the average of the squared azimuthal velocity v_ϕ, while $\bar{v}_\phi(R, z) = R\Omega(R, z)$ is the average azimuthal velocity and σ_ϕ is the azimuthal velocity dispersion.
If one assumes that $\sigma_\phi = \sigma$ one obtains the system of equations (2.1.1).

Chapter 3

The numerical method

In this chapter, we are going to give a brief explanation of how we implement a numerical method to estimate the vertical structure of gaseous discs, by expanding the Python module `galpynamics`. We focus in particular on the iterative part of the code, responsible for the study of galaxy dynamics. We then introduce our own set of Python scripts, highlighting the similarities and the differences with `galpynamics`. Finally, we explain how to use our code and what a single run consists of.

3.1 The starting point: `galpynamics`

`Galpynamics` is a Python module freely available on GitLab which is used to study the properties of spheroidal and disc galactic components, as well as the dynamics of galactic gaseous discs, taking into account for the disc self-gravity. The module includes various analytical models of spherical halos and surface densities of discs (that can be used to model either stellar or gaseous ones). We show some examples of haloes models in Fig. 3.1a, where we plot their volume density ρ against the elliptical radius defined in Eq. (2.3.3); for each profile, we set the central density ρ_0 to 10^7 $M_\odot kpc^{-3}$, and the scale length to $r_s = 10$ kpc. In Fig. 3.1b, we present some examples of disc models, where we plot their surface density against the cylindrical radius, setting for every profile the central surface density Σ_0 to 10^6 $M_\odot kpc^{-2}$, and the scale length to $R_d = 10$ kpc. When working with thick discs, the vertical structure $z_d(R)$ can be either constant or be described by

one of the following profiles:

$$z_d(R) = \sum_{i=0}^{7} p_i R^i, \tag{3.1.1}$$

$$z_d(R) = h_0 + c(\text{asinh}(R^2/R_f^2)), \tag{3.1.2}$$

$$z_d(R) = h_0 + c(\tanh\big(R^2/R_f^2\big)), \tag{3.1.3}$$

where p_i are the coefficients of the polynomial, c is a constant, h_0 is the central height and R_f is the flaring scale length. Moreover, we use it to calculate the gravitational potential of our components, following the treatment discussed in Section 2.3. We mentioned that, unlike Cuddeford (1993), we prefer to use the formulation with the elliptical integral: this is because it is already included in the gsl library we use in the code.
This module is at the base of our study of the dynamics of galactic gaseous discs: we explain in detail our approach in Section 3.1.1.

3.1.1 Iterative estimation of the 3D gas distribution

`Galpynamics` implements an iterative method that accounts for the self-gravity of the disc. Basically, given a galaxy model, `galpynamics` can be used to calculate through numerical integration the potential, which is then used to determine the vertical profile of the density of the gas discs. Then the radial profile of the scale height is found fitting at each value of the radius the gas vertical distribution. The module relies on a few assumptions:

1. The gas disc is in vertical hydrostatic equilibrium.

2. The fluid and the potential are axisymmetric (so no dependence on the azimuthal angle), and the system is assumed to be symmetric to the plane $z = 0$.

3. The gas disc is assumed to stationary rotate with $V_{\text{rot}} = v_\phi = v_\phi(R)$, and the velocity dispersion is isotropic and independent of z, thus $\sigma = \sigma(R)$.

4. The density is defined as
$$\rho(R, z) = \Sigma_{\text{int}}(R)\frac{\zeta(z, z_d(R))}{z_d(R)k}, \tag{3.1.4}$$
where Σ_{int} is the intrinsic surface density, ζ is the functional form depending on the scale height z_d and k is a constant such that the integral of ρ along the vertical layer is exactly Σ_{int}.

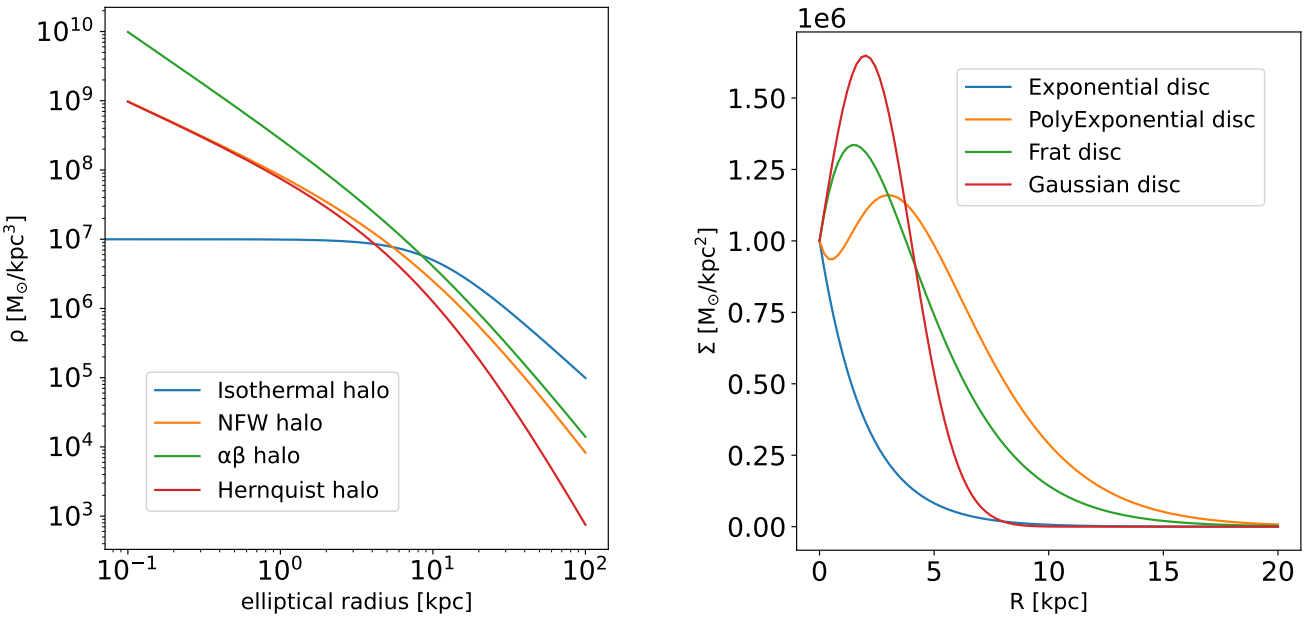

(a) Models of spherical haloes.

(b) Models of surface density of discs.

Figure 3.1: Various models of haloes (Fig. 3.1a), and surface density of discs (Fig. 3.1b) present in `galpynamics`. In Fig. 3.1a, for all the profiles, we set the central density ρ_0 to 10^7 $M_\odot kpc^{-3}$, and the scale length to $r_s = 10$ kpc, while the elliptical radius is defined in Eq. (2.3.3). In Fig. 3.1b, for all the profiles, we set the central surface density Σ_0 to 10^6 $M_\odot kpc^{-2}$, and the scale length to $R_d = 10$ kpc.

For a given model, the module applies the following iterative procedure, working on a user-defined grid: first there is a preliminary stage, in which the disc is considered thin and essentially massless, where the fixed potential of DM and stars Φ_{ext} is calculated, and then used to get a first estimate of the disc vertical density profile using Eq. (2.2.5), which is subsequently fit with a functional form to derive an initial guess for the scale-height z_d. The radial trend of z_d is then also fit with a functional form, and used in Eq. (3.1.4) to define a 3D density model, which allows us to get a first estimate of the disc potential Φ, which is then used to set the total galactic potential to $\Phi_{\text{tot}} = \Phi + \Phi_{\text{ext}}$. We then re-calculate the vertical density profile, but this time using Φ_{tot} to take into account the self-gravity of the disc. Once again, the profile is then fit with a functional form to derive the scale-height z_d, which is used in Eq. (3.1.4) to re-define the 3D density model in order to re-evaluate Φ and update Φ_{tot}, which is then used to find a new vertical density profile and consequently a different scale-height. This procedure is then repeated until the maximum difference

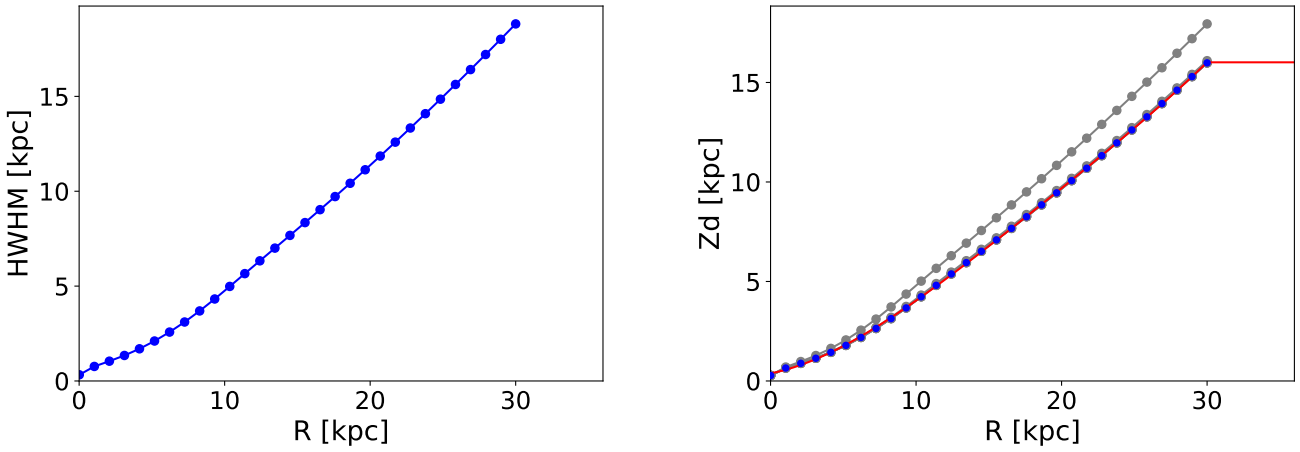

(a) (b)

Figure 3.2: The HWHM (on the left) and the disc scale height (on the right) as a function of the radius given as final output of the iterative procedure used by `galpynamics`. The model used for this example contains a NFW halo, a Hernquist bulge, and an exponential stellar disc, while the surface density of the gas disc is described by a Fraternali profile, with a constant velocity dispersion $\sigma = 10$ km s^{-1}.

between two successive estimates of z_d is less than a user defined threshold, which default value is 10^{-4}. As a final step, the code gives in output the final HWHM (Half-Width-Half-Maximum), and the estimate of the disc scale height z_d, showing both the final one (in blue) and the results obtained in the previous iterations (in gray). We show an example of the HWHM and z_d profiles in Fig. 3.2.

3.2 A method to account for $\sigma = \sigma(R, z)$

For the purpose of this work, we need a more flexible method than the one provided by `galpynamics`, so we derived a new method which allows us to compute models with vertical non-isothermal distributions. This of course means that we need to modify some of the basic assumptions:

1. The velocity dispersion is isotropic, but it can depend on both the radial and vertical coordinate, thus $\sigma = \sigma(R, z)$.

2. The gas disc is stationary and rotates with rotational velocity $V_{rot} = v_\phi = v_\phi(R, z)$, as the distribution is in general baroclinic.

3. The density is defined as
$$\rho(R, z) = \Sigma_{\rm int}(R)\frac{\tilde{\rho}(R, z)}{k(R)}, \tag{3.2.1}$$
where $\Sigma_{\rm int}$ is the intrinsic surface density, $\tilde{\rho} = \rho(R, z)/\rho(R, 0)$ is the normalized vertical density profile and $k(R)$ is a function such that the integral of ρ along z is $\Sigma_{\rm int}$.

The first two points are of course needed to model a gas disc with a velocity dispersion that depends on z, which is the first obvious difference between our method and the original implementation of `galpynamics`. The third point illustrates the second difference: while we still use an analytical profile to define $\Sigma_{\rm int}$, our vertical density profile is not fit with a functional form, and it is instead a purely numerical profile. Naturally, the first consequence of this approach is that k in Eq. (3.2.1) cannot be a constant and has to become a function of the radius (so $k = k(R)$), which needs to be found numerically as well, and we find it by multiplying by 2 the integral of $\tilde{\rho}$ along the positive half of the vertical axis. The second is that now, to estimate the potential, we first need to construct a function for the density by interpolating the points of $\tilde{\rho}(R, z)/k(R)$, as our method does not allow us to solve Eq. (2.3.12) unless the density is given in input as a function. Unfortunately, having to construct a function for every point of integration instead of simply using an analytical profile has an immediate drawback: that is, it requires longer computational times. However, we have tried to obviate this problem by adding the possibility of using more than one processor at a time when estimating the potential. Another consequence of not fitting the vertical density profile to an analytical one is that now finding the scale height at each iteration is redundant, which means we now only find it after the iterative part is complete. We define the disc scale height $h_{34\%}$ as the height which contains 34% of the total mass along the positive half of the vertical axis, which is equivalent to the total area at $1\sigma_{\rm std,dev}$ for a Gaussian distribution. Finally, we want to point out that to find the normalized vertical density profile $\tilde{\rho}$ we use the same approach as `galpynamics`, but since this time we need Eq. (2.2.4) instead of Eq. (2.2.5) we have an additional integral that has to be solved numerically. There are different ways to do it, and in Appendix A we explain in detail the tests we run, and we illustrate the adopted method. We also calculate the vertical profile of the pressure P using the relation $P = \sigma^2\rho$, and the vertical Brunt-Väisäla frequency squared N_z^2. As in Section 3.1.1, we describe here the iterative procedure we use, where all the calculations are executed on a user-defined grid:

0. At the beginning, the disc is assumed to be infinitesimally thin, and essentially massless, so we ignore its contribution to the total gravitational potential. First, the fixed external

potential Φ_{ext} is found, and used to get a first estimate of the normalized vertical density profile $\tilde{\rho}$ using Eq. (2.2.4). The obtained result is used in Eq. (3.2.1) to construct $\rho(R, z)$, which is then inserted in Eq. (2.3.12) to get a first estimate of the disc potential Φ, which is used to set the total galactic potential to $\Phi_{\text{tot}} = \Phi + \Phi_{\text{ext}}$. The normalized vertical density profile is then calculated again using Eq. (2.2.4) with Φ_{tot}, this time taking into account the self-gravity of the disc.

1. From now on, the disc is considered thick and massive, and we use $\tilde{\rho}$ to determine again first $k(R)$ and then $\rho(R, z)$ in the form of Eq. (3.2.1), which is used to re-evaluate the potential Φ (and, consequently, Φ_{tot}). The estimate of the vertical density profile is thus repeated same as before. This step is repeated until the maximum relative difference between two successive estimates of the vertical density profile is less than a user defined threshold, which default value is 10^{-4}.

2. As a final step, we calculate the disc scale-height $h_{34\%}$, the normalized vertical pressure profile $\tilde{P} = \tilde{\rho}\sigma^2(R, z)$, and the vertical Brunt-Väisäla frequency N_z squared. In particular, the disc scale-height is defined as the height where

$$\int_0^{h_{34\%}} \frac{\tilde{\rho}(R, z)}{k(R)} = 0.34 \tag{3.2.2}$$

Chapter 4

Illustrative models

In this chapter, we present some models obtained using the code we developed. We show illustrative multicomponent models, including, aside from the gaseous disc, the DM halo, the stellar disc, and the stellar bulge. Although the tested models may not necessarily represent realistic Galactic conditions, they effectively highlight and amplify the systematic effect of assuming a vertical non-isothermal distribution.

4.1 The profiles of the mass components

4.1.1 The DM halo

For simplicity, the DM halo is assumed spherical in all of our models. We use either a Navarro-Frenk-White (NFW) halo or a pseudo-isothermal halo. The NFW profile (Navarro et al., 1996) is

$$\rho_{DM} = 4\rho_{DM,s}\left(\frac{r}{r_s}\right)^{-1}\left(1+\frac{r}{r_s}\right)^{-2}, \tag{4.1.1}$$

where $r=\sqrt{R^2+z^2}$, r_s is the scale radius, and $\rho_{DM,s}$ is such that $\rho_{DM}(r_s)=\rho_{DM,s}$. The pseudo-isothermal halo (van Albada et al., 1985) is

$$\rho_{DM}(r) = \rho_{DM,0}\left(1+\frac{r^2}{r_c^2}\right)^{-1}, \tag{4.1.2}$$

where $\rho_{DM,0}$ is the central volume density, and r_c is the core radius.

4.1.2 The stellar disc

We assume that the stellar discs have mass distributions in the form of an exponential profile along the radial coordinate, and a sech^2 profile along z:

$$\rho_\star(R,z) = \rho_{\star,0} \exp\left(-\frac{R}{R_\star}\right) \mathrm{sech}^2(z/z_\star), \tag{4.1.3}$$

where $\rho_{\star,0} = \Sigma_{\star,0}/(2z_\star)$ is the central density, $R_\star$ is the radial scale length, and $z_\star$ is the vertical scale height.

4.1.3 The bulge

We use for the bulge an Hernquist profile (Hernquist, 1990)

$$\rho(R) = \frac{\rho_0 r_s}{r} \frac{1}{\left(1+\frac{r}{r_s}\right)^3}, \tag{4.1.4}$$

where ρ_0 is the central density and r_s is a scale length.

4.1.4 The gas density

We define the gas density using Eq. (3.2.1). As we have explained in Section 3.2, the normalized vertical density profile is calculated numerically, so we only need to choose how to model the gas surface density distribution. We describe the surface density $\Sigma(R)$ using the following profile

$$\Sigma(R) = \Sigma_0 \exp\left(-\frac{R}{R_d}\right)\left(1+\frac{R}{R_{d2}}\right)^\alpha, \tag{4.1.5}$$

with Σ_0 being the central surface density, R_d and R_{d2} being two characteristic scale lengths, and α the index of the power-law.

4.1.5 The gas velocity dispersion

For the gas velocity dispersion σ, we generally assume, for the radial profile, either a constant or an exponential profile

$$\sigma(R) = \sigma_{\mathrm{gas},0} \exp\left(-\frac{R}{R_\sigma}\right), \tag{4.1.6}$$

where $\sigma_{\mathrm{gas},0}$ is the gas velocity dispersion at the galaxy centre and R_σ is a scale radius. In the case of a constant velocity dispersion along R, when adding the dependence on z we use

$$\sigma(z) = \sigma_{\mathrm{gas},0} \exp\left(s\frac{|z|}{z_\sigma}\right), \tag{4.1.7}$$

where $s = \pm 1$ and z_σ is a generic scale height. If we use for the radial part the profile described in Eq. (4.1.6) and add the z-dependent part, we can have either of these two profiles:

$$\sigma(R, z) = \sigma_{\rm gas,0} \exp\left(-\frac{R}{R_\sigma}\right) \exp\left(s\frac{|z|}{z_\sigma}\right), \tag{4.1.8}$$

where $s = \pm 1$ and z_σ is a generic scale height.

4.2 Illustrative model I

In this section, we are going to present a model of a mock spiral galaxy. We set the mass components as follows:

- For the DM halo, we choose a NFW profile, where we use for the central density $\rho_{DM,s} = 2.5 \times 10^5$ $\mathrm{M_\odot kpc^{-3}}$, and the scale radius $r_s = 5$ kpc, with $M_{\rm DM}(R = 30 \text{ kpc}) = 1.71 \times 10^9$ and $M_{\rm DM}(R = 100 \text{ kpc}) = 3.29 \times 10^9$.
- For the Hernquist bulge, we have for the central density $\rho_0 = 3 \times 10^8$ $\mathrm{M_\odot kpc^{-3}}$, and for the radial scale length $r_{s,\rm Bulge} = 1$ kpc, $M_{\rm Bulge}(R = 5 \text{ kpc}) = 1.31 \times 10^9$.
- For the exponential stellar disc, the parameters are the central surface density $\Sigma_{\star,0} = 5 \times 10^6$ $\mathrm{M_\odot kpc^{-2}}$, the radial scale length $R_\star = 3$, and the vertical scale height $z_\star = 0.4$ kpc.
- For the gaseous disc: central surface density $\Sigma_0 = 10^6$ $\mathrm{M_\odot kpc^{-2}}$, the first radial scale length $R_d = 5$ kpc, the second radial scale length $R_{d2} = 5$ kpc, and the power-law index $\alpha = 1$.

In Fig. 4.1 we report the different contributions to the circular velocity V_c at $z = 0$ for each component described above. The bulge is the one giving the biggest contribution, up to $R \approx 20$ kpc, where the NFW halo starts to dominate. We want to point out that the contribution from the bulge here is bigger than what it is usually found in real galaxies: this is because we wanted to show two extreme effects, aka the bulge dominance and the bulge absence, which is shown in Section 4.3. Moreover, while we show the contribution of the gas disc, it is considered merely for an illustrative purpose as in this stage we do not consider the vertical structure yet, which is however necessary to find the actual contribution. We will show our results when using either a σ constant along R (case IC) or with a radial profile described by Eq. (4.1.6) (case IR). We show the parameters for both cases in Table 4.1. For the vertical profile of the velocity dispersion, we choose 5 different models, described in Table 4.2. One is equivalent to having a vertical isothermal

Parameters of the models		
Case	$\sigma_{gas,0}$ [km s^{-1}]	$R_\sigma[kpc]$
IC	10	
IR	10	30

Table 4.1: Parameters of the two cases we show for our first illustrative model, each one associated to a different radial profile for the velocity dispersion. In particular: case IC refers to a velocity dispersion constant along R, while case IR refers to Eq. (4.1.6).

Parameters and names of vertical profiles of σ		
Name	s	z_σ [kpc]
XIso	0	–
X+20	+1	20
X+30	+1	30
X-20	−1	20
X-30	−1	30

Table 4.2: Names for the various models associated to a specific vertical profile of the velocity dispersion. The X is a placeholder, and will be substituted by either IC, or IR, depending on the case being studied.

distribution, with $s = 0$, called XIso, two have $s = +1$, with $z_\sigma = 20$ and 30 kpc respectively, called X+20 and X+30, and finally the last two have $s = -1$, with $z_\sigma = 20$ and 30 kpc respectively, called X-20 and X-30. The X is a placeholder, and will be substituted with the name of the case under study: for example, when we work on case IC, the models will be called ICIso, IC+20, IC+30 and so on. In Fig. 4.2, we show the radial profiles of the velocity dispersion at $z = 10$ kpc, using shaded areas that have as upper limit a vertical profile described by models X+20, and as lower limit the one represented by models X-20, while the solid lines represent the radial profiles of models XIso. For every model in each case we use a linear grid of 30 points on the radial axis that goes from 0.01 to 30 kpc, and one of 60 points that goes from 0 to 20 kpc for the vertical axis. We calculate the scale height $h_{34\%}$ as the height at each value of R where 34% of the mass along the vertical axis is contained. We choose this value for convenience, since, when fitting the normalized vertical density profile with a Gaussian distribution, its standard deviation $\sigma_{\rm std,dev}$ is taken as the scale height, and for a Gaussian profile the mass contained within $1\sigma_{\rm std,dev}$ above the

midplane is 34% of the total.

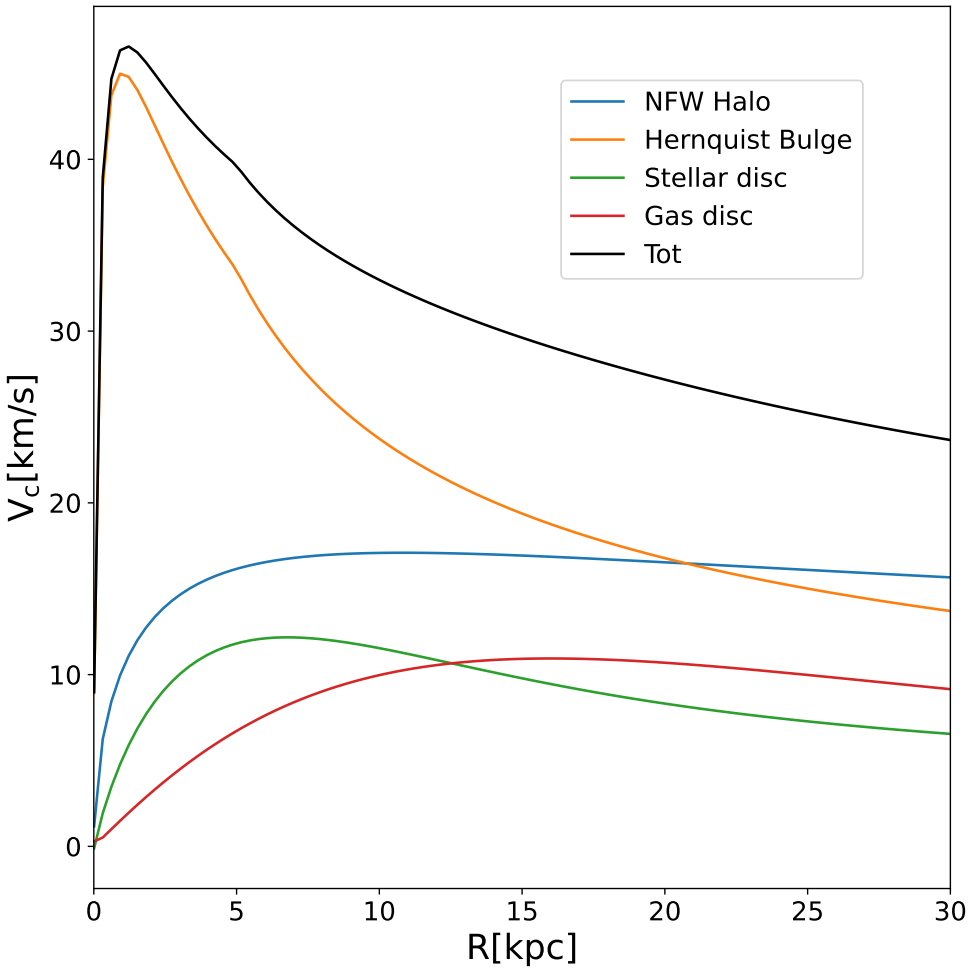

Figure 4.1: Circular velocity V_c for each fixed component of our model. The black line is the total contribution, the NFW halo is the blue line, the Hernquist bulge is the yellow line, the stellar disc is the green line, and the gas disc is the red line. The contribution from the gas disc is merely illustrative, as here the disc is considered thin, so it is not the final contribution, which also depends on the scale-height.

4.2.1 Results for case IC

We first show the result obtained for case IC with our 5 different models. In Fig. 4.3 we present the normalized vertical density profiles $\tilde{\rho}$ for our model. The black dashed line represents the ICIso model, and we can see immediately some noticeable differences between it and the IC-20 and IC-30

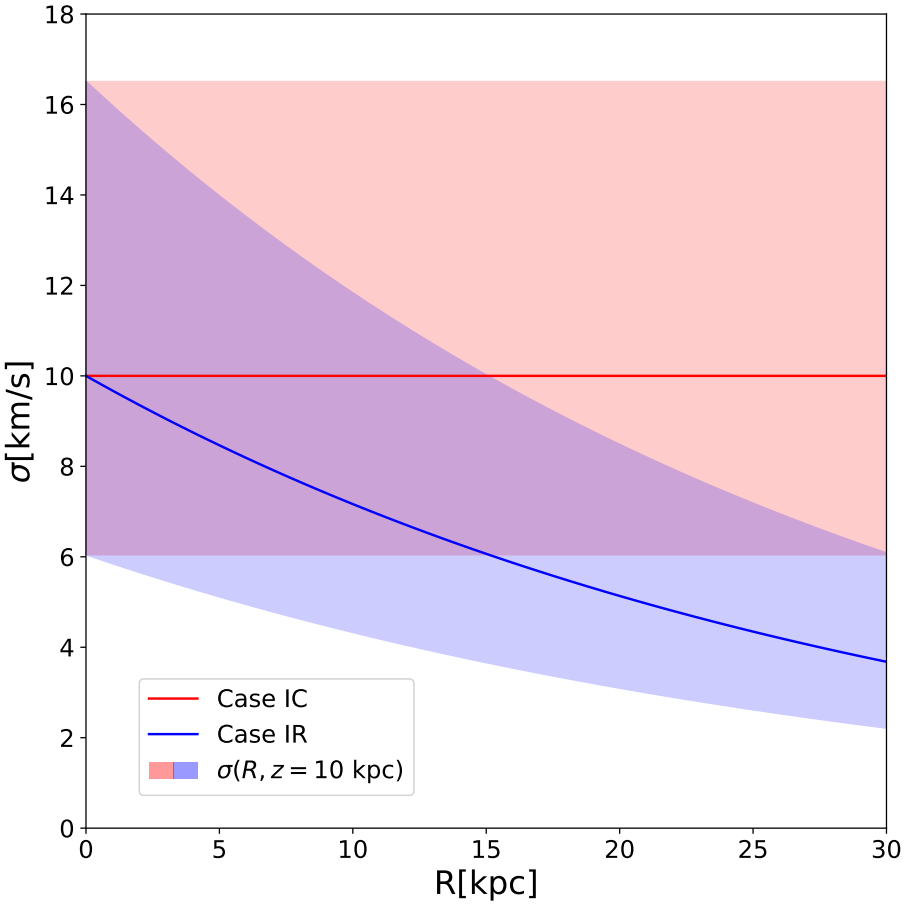

Figure 4.2: Plot showing the two different radial profiles of the velocity dispersion we use. In particular: case IC refers to a σ constant along R, while case IR refers to Eq. (4.1.6). For each case, the shaded area represents the dependence on z, with the upper limit being defined by models X+20, and the lower one by models X-20, all calculated at $z = 10$ kpc.

models: the latters have the peak shifted from $z = 0$ at high values of R. In Fig. 4.4 we show the comparison of the disc scale height for the various models. Compared to the ICIso model, the IC+20 and IC+30 models have a higher disc scale-height up to $R \approx 15 - 17$ kpc, but then their growth slows down, reaching lower values at bigger radii than the ones for the ICIso model. The IC-20 model has a disc scale-height that is always smaller than the ICIso one, however the IC-30 model surpasses the ICIso one at around $R \approx 17$ kpc. In Fig. 4.5 we show the pressure profiles of our models, which, as we expected, always have a negative gradient, as this is required to maintain the vertical hydrostatic equilibrium. Figure 4.6 shows the vertical Brunt-Väisäla frequency squared N_z^2: the reason we show this is that, with the assumptions we explained in Section 2.5, N_z^2 has

to be positive in order to have stability according to the Solberg-Høiland criterion, but as we can see, this is not always the case. When assuming a velocity dispersion that decreases along z, like we do for models IC-20 and IC-30, we may violate the criterion, as the frequency squared can be negative.

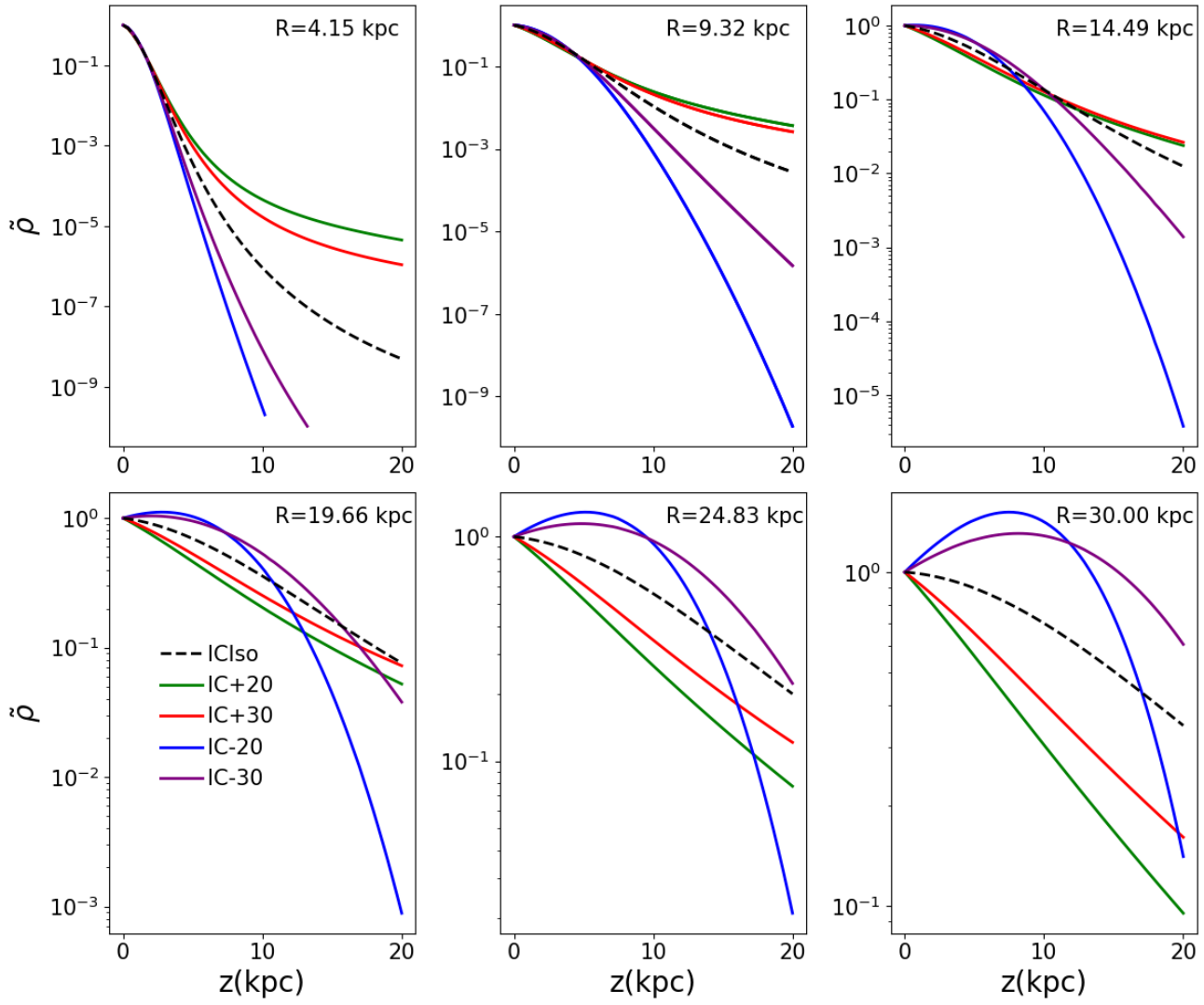

Figure 4.3: Normalized vertical density profile $\tilde{\rho} = \rho(R, z)/\rho(R, 0)$ for our illustrative models. The profiles were obtained with 30 points in a linear interval along R, from 0.01 to 30 kpc, and with 60 points in a linear interval along z, from 0 to 20 kpc. The ICIso model is the one represented with the black dashed line. The blue and the purple profiles correspond to models IC-20 and IC-30 respectively, while the green and red ones to IC+20 and IC+30.

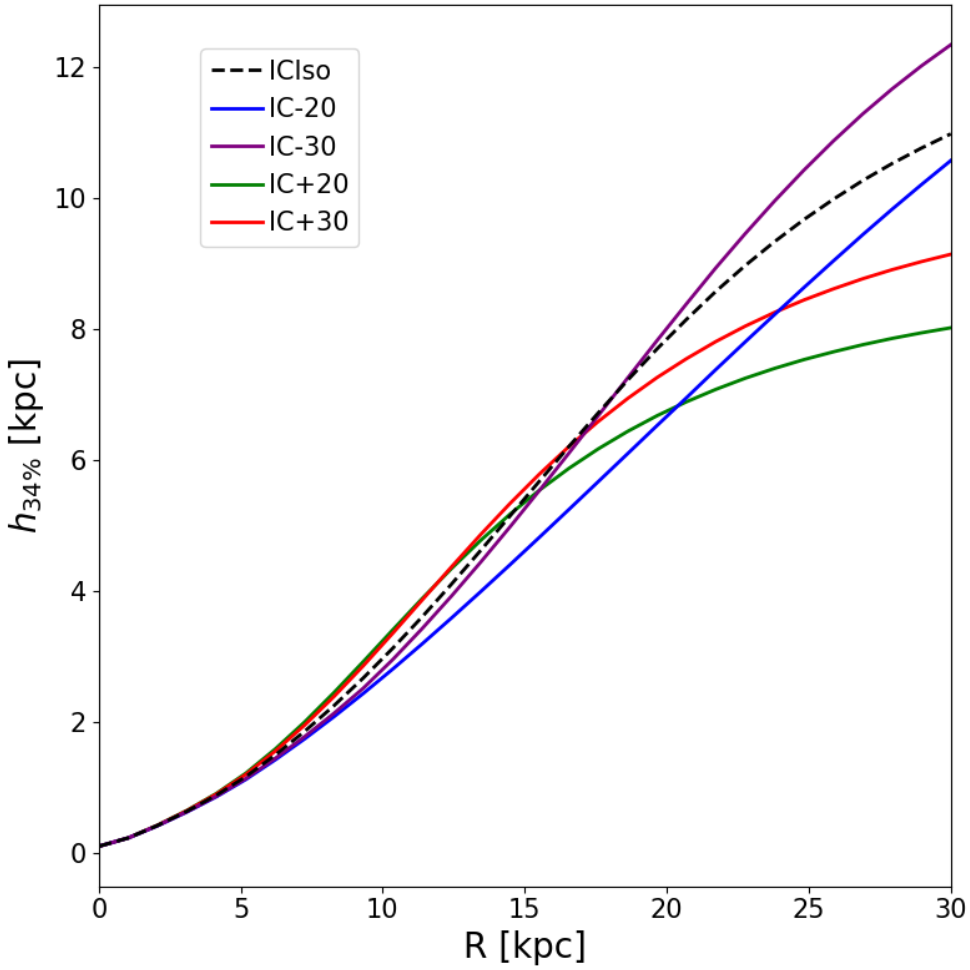

Figure 4.4: Scale height $h_{34\%}$ for our illustrative models. The profiles were obtained with 30 points in a linear interval along R, from 0.01 to 30 kpc, and with 60 points in a linear interval along z, from 0 to 20 kpc. The ICIso model is the one represented with the black dashed line. The blue and the purple profiles correspond to models IC-20 and IC-30 respectively, while the green and red ones to IC+20 and IC+30.

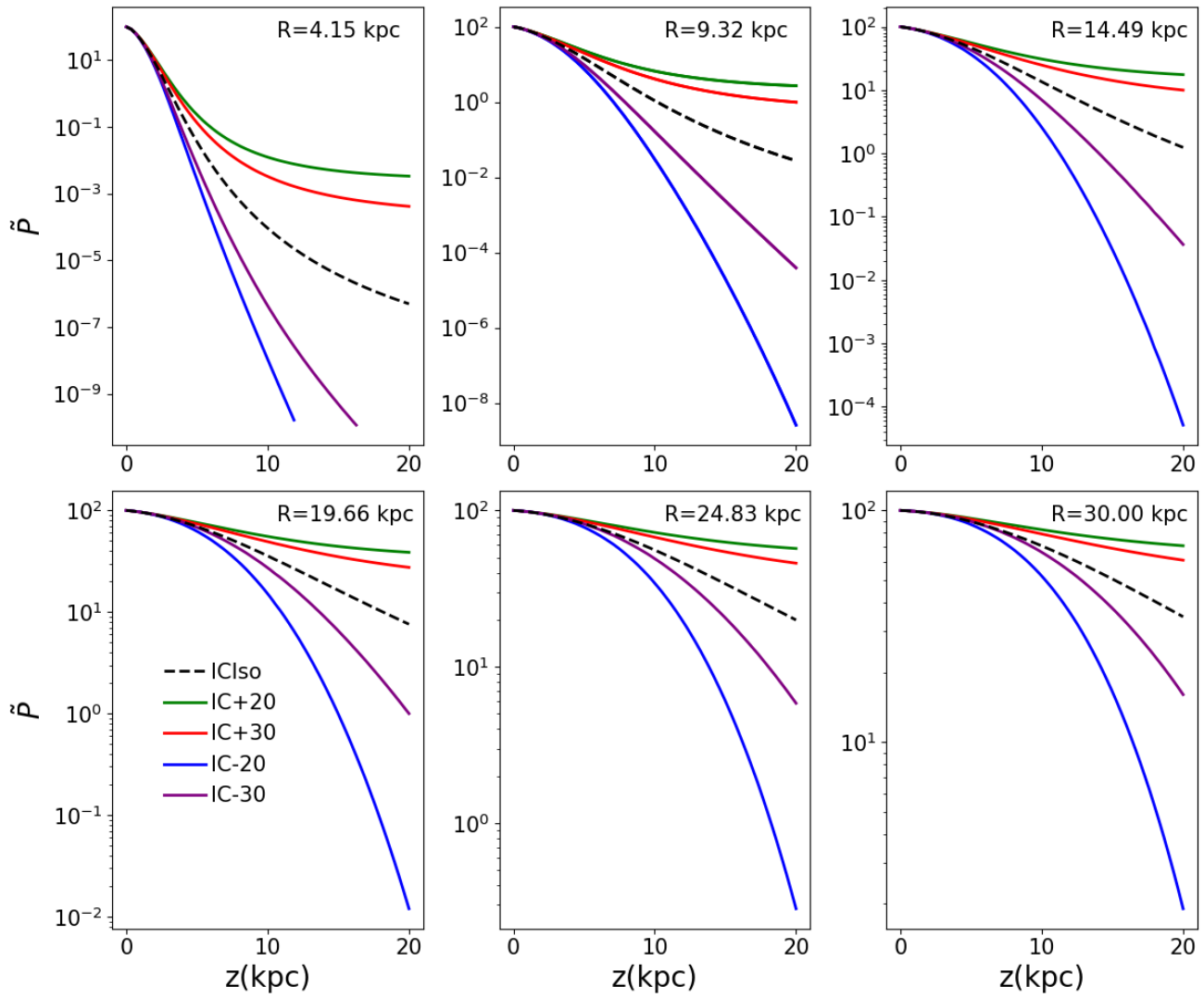

Figure 4.5: Normalized vertical pressure profile $\tilde{P}$ for our illustrative models. The profiles were obtained with 30 points in a linear interval along R, from 0.01 to 30 kpc, and with 60 points in a linear interval along z, from 0 to 20 kpc. The ICIso model is the one represented with the black dashed line. The blue and the purple profiles correspond to models IC-20 and IC-30 respectively, while the green and red ones to IC+20 and IC+30.

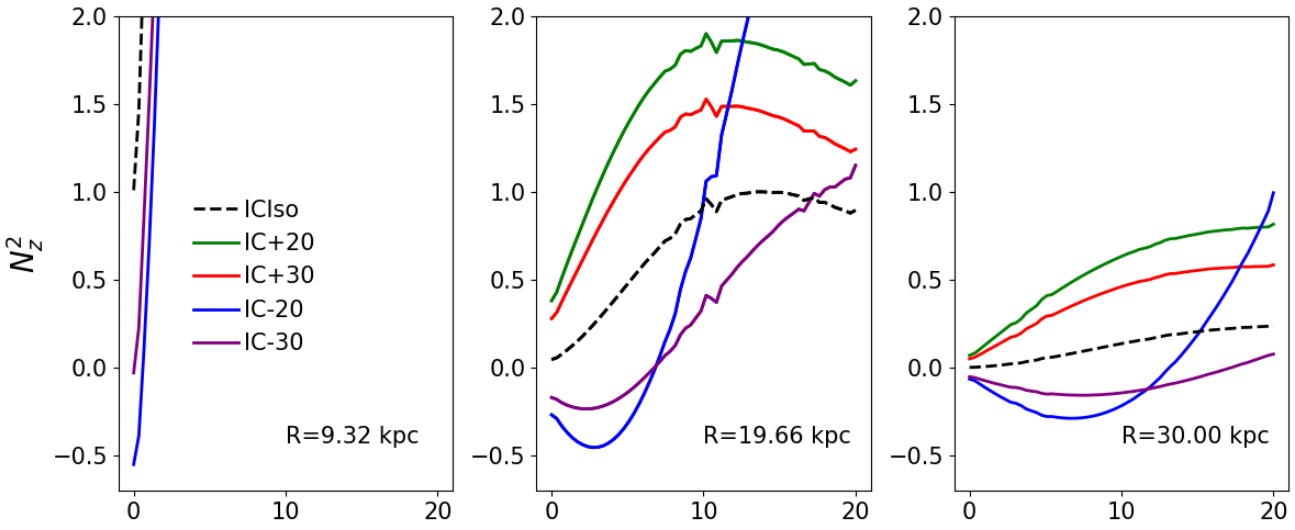

Figure 4.6: Vertical Brunt-Väisäla frequency squared N_z^2 for our illustrative models. The profiles were obtained with 30 points in a linear interval along R, from 0.01 to 30 kpc, and with 60 points in a linear interval along z, from 0 to 20 kpc. The ICIso model is the one represented with the black dashed line. The blue and the purple profiles correspond to models IC-20 and IC-30 respectively, while the green and red ones to IC+20 and IC+30.

4.2.2 Results for case IR

In this subsection, we present our case IR, and the results for every model. The normalized vertical density profile $\tilde{\rho}$ is shown in Fig. 4.7: similar to what we find in case IC (Section 4.2.1), the IR-20 and IR-30 models have the peak shifted from $z = 0$, although this time the shift is not as evident. There is also another trend that we can clearly see: the IR+20 and IR+30 models have a slower decrease compared to the IRIso model, while the opposite is true for the IR-20 and IR-30 models. This means that the mass is more concentrated for models that have a velocity dispersion that decreases with z. While this effect is already visible in Fig. 4.3 for the IC-20 model, in this case is more evident and present at all radii. This of course has an effect on the scale height: as shown in Fig. 4.8, both IR-20 and IR-30 have a lower scale height compared to IRIso, while the opposite is true for IR+20 and IR+30. We then show the pressure profiles in Fig. 4.9, and we see that the vertical hydrostatic equilibrium is kept. Finally, in Fig. 4.10 we show the vertical Brunt-Väisäla frequency squared N_z^2, which, just as we saw for case IC (Section 4.2.1), can be negative for certain values of R and z for our IR-20 and IR-30 models, both of which have a $\sigma(R, z)$ that decreases along z, hence we may violate the Solberg-Høiland criterion.

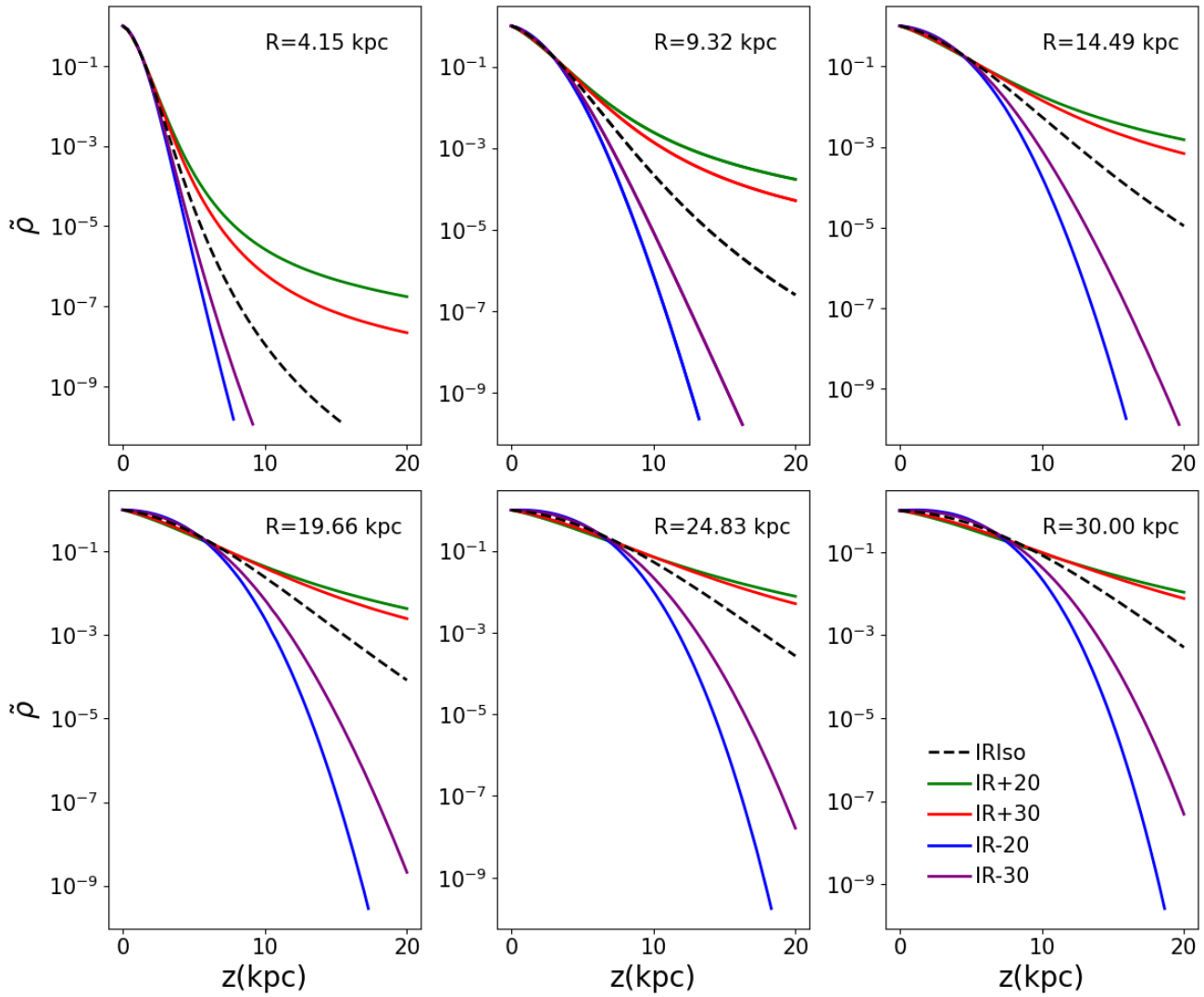

Figure 4.7: The same as Fig. 4.3, but for case IR.

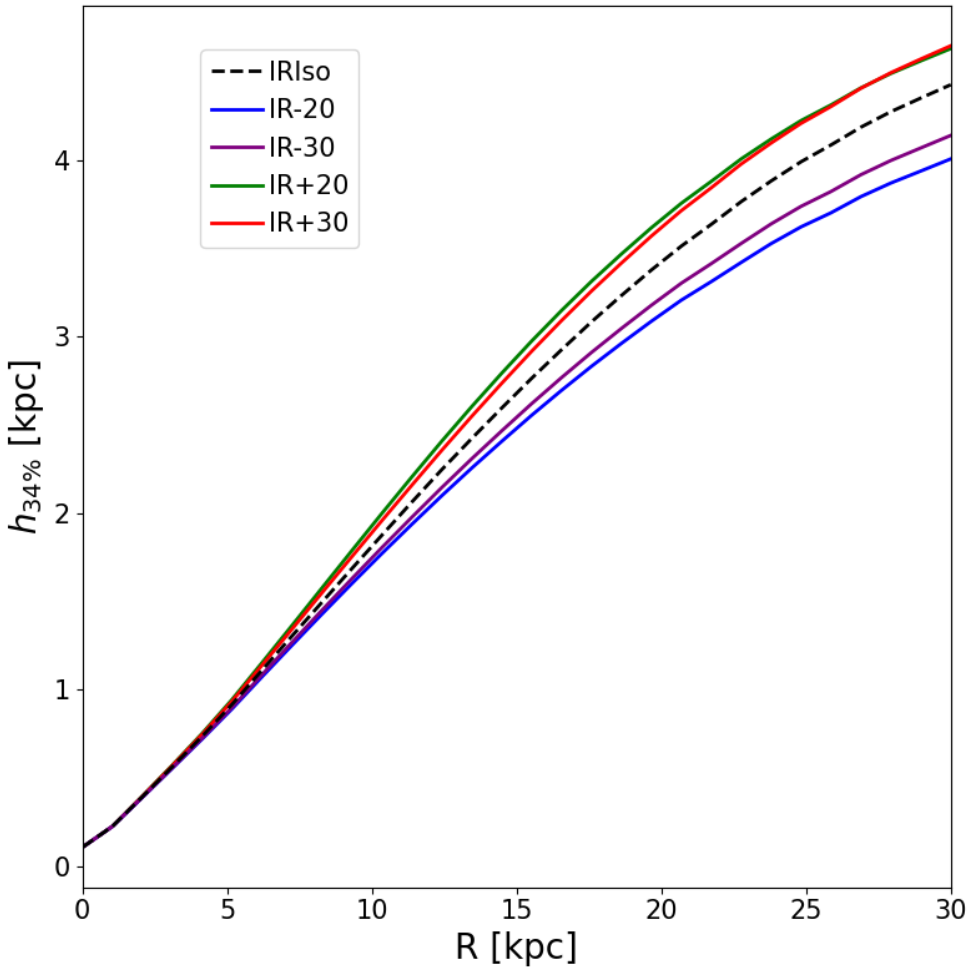

Figure 4.8: The same as Fig. 4.4, but for case IR.

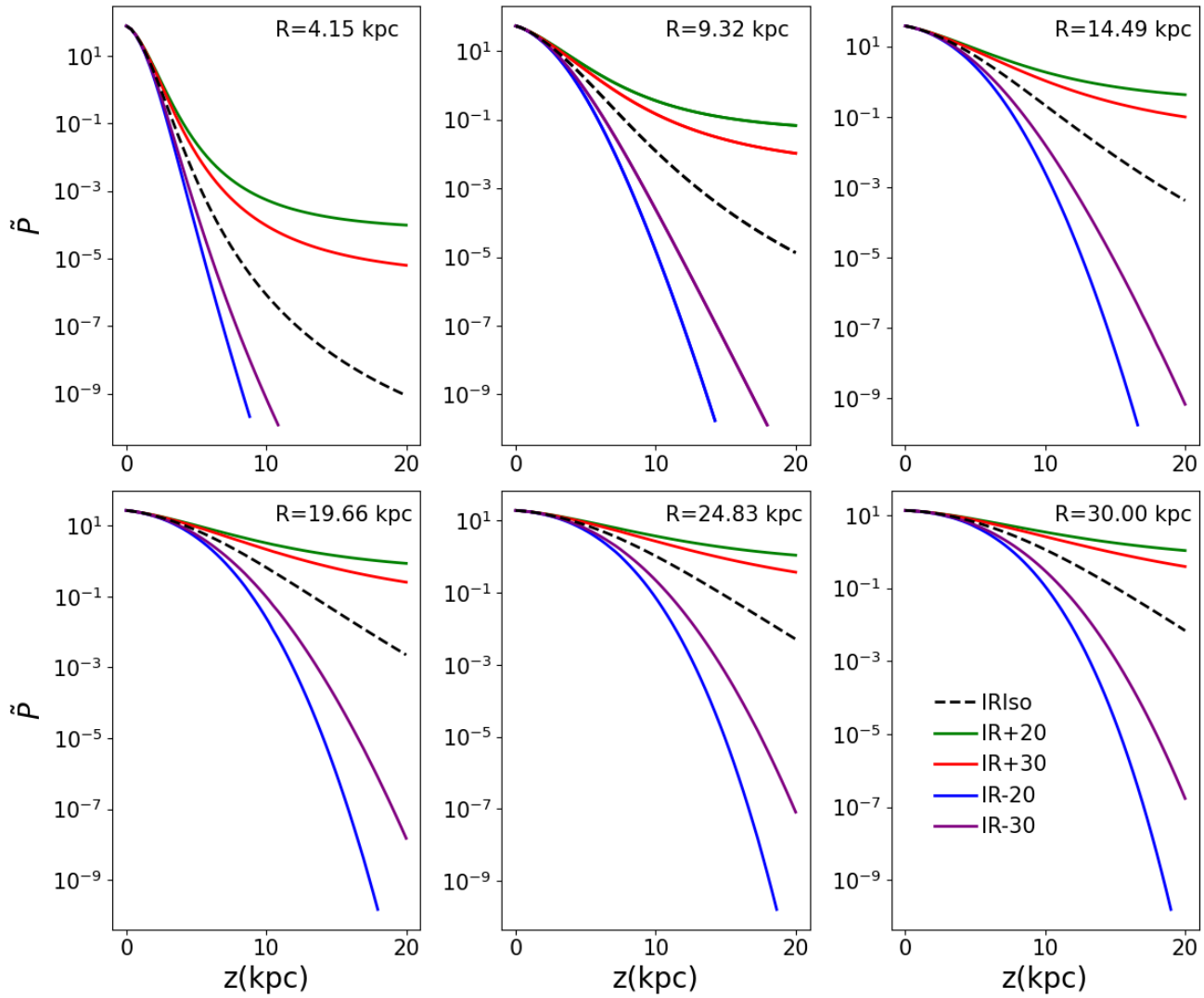

Figure 4.9: The same as Fig. 4.5, but for case IR.

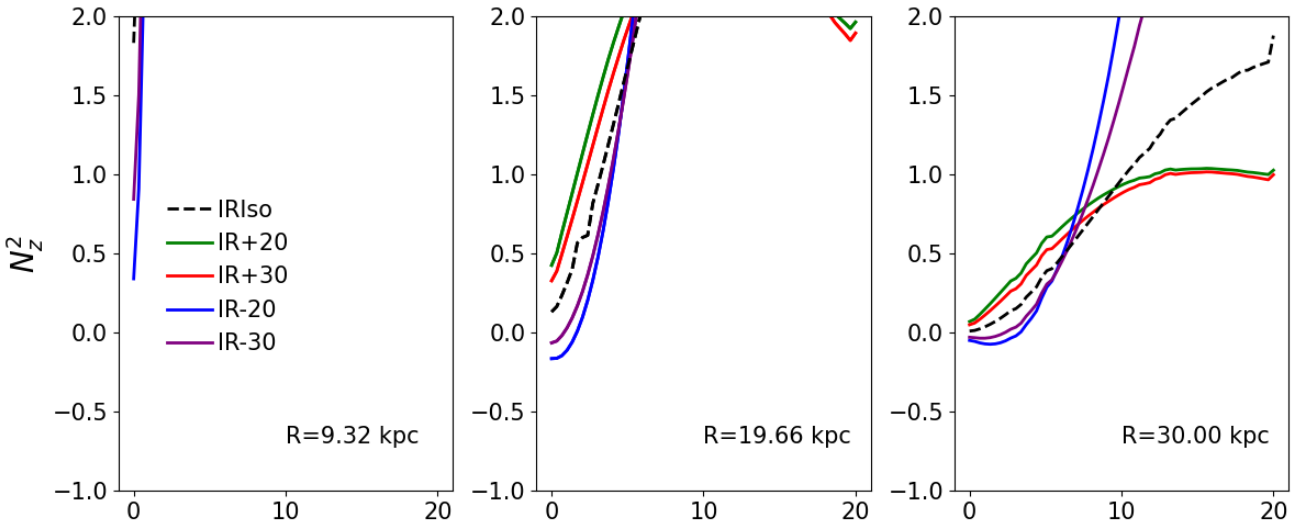

Figure 4.10: The same as Fig. 4.6, but for case IR.

4.3 Illustrative model II

We now present a second illustrative model of a disc galaxy. For this model, we use a different halo, and we remove the bulge. This is to show the impact of the choice of the density distribution of the components, and to highlight the effects caused by the absence of a bulge. We now set the various mass components as follows:

- For the DM halo, we choose the pseudo-isothermal profile, where we use for the central density $\rho_{DM,0} = 10^6$ M$_\odot$kpc^{-3}, and the scale radius $r_s = 5$ kpc, with $M_{\rm DM}(R = 30$ kpc$) = 7.22 \times 10^9$ and $M_{\rm DM}(R = 100$ kpc$) = 2.90 \times 10^{10}$.

- For the exponential stellar disc, the parameters are the central surface density $\Sigma_{\star,0} = 5 \times 10^6$ M$_\odot$kpc^{-2}, the radial scale length $R_\star = 3$, and the vertical scale height $z_\star = 0.4$ kpc.

- For the gaseous disc: central surface density $\Sigma_0 = 10^6$ M$_\odot$kpc^{-2}, the first radial scale length $R_d = 5$ kpc, the second radial scale length $R_{d2} = 5$ kpc, and the power $\alpha = 1$.

Here the dominant component is by far the pseudo-isothermal DM halo, as shown in Fig. 4.11, and, as we stated in Section 4.2, the contribution from the gas disc is to be considered merely illustrative. We use the same profiles for the velocity dispersion as we did in Section 4.2, so we will show our results when using either a σ constant along R (case IIC) or with a radial profile described by Eq. (4.1.6) (case IIR). We show the parameters for both cases in Table 4.3. For the

Parameters of the models		
Case	$\sigma_{gas,0}$ [km s^{-1}]	$R_\sigma[kpc]$
IIC	10	
IIR	10	30

Table 4.3: Parameters of the two cases we show for our first illustrative model, each one associated to a different radial profile for the velocity dispersion. In particular: case IIC refers to a velocity dispersion constant along R, while case IIR refers to Eq. (4.1.6).

vertical profile of the velocity dispersion, we choose 5 different models, described in Table 4.4. One is equivalent to having a vertical isothermal distribution, with $s = 0$, called XIso, two have $s = +1$, with $z_\sigma = 20$ and 30 kpc respectively, called X+20 and X+30, and finally the last two have $s = -1$, with $z_\sigma = 20$ and 30 kpc respectively, called X-20 and X-30. The X is a placeholder, and will be substituted with the name of the case under study: for example, when we work on case IIC, the models will be called IICIso, IIC+20, IIC+30 and so on. Just like we did in Section 4.2, for every model in each case we use a linear grid of 30 points on the radial axis that goes from 0.01 to 30 kpc, and one of 60 points that goes from 0 to 20 kpc for the vertical axis, and we calculate the scale height $h_{34\%}$ as the height at each value of R where 34% of the mass along the vertical axis is contained.

Parameters and names of vertical profiles of σ		
Name	s	z_σ [kpc]
XIso	0	–
X+20	+1	20
X+30	+1	30
X-20	−1	20
X-30	−1	30

Table 4.4: Names for the various models associated to a specific vertical profile of the velocity dispersion. The X is a placeholder, and will be substituted by either IIC, or IIR, depending on the case being studied.

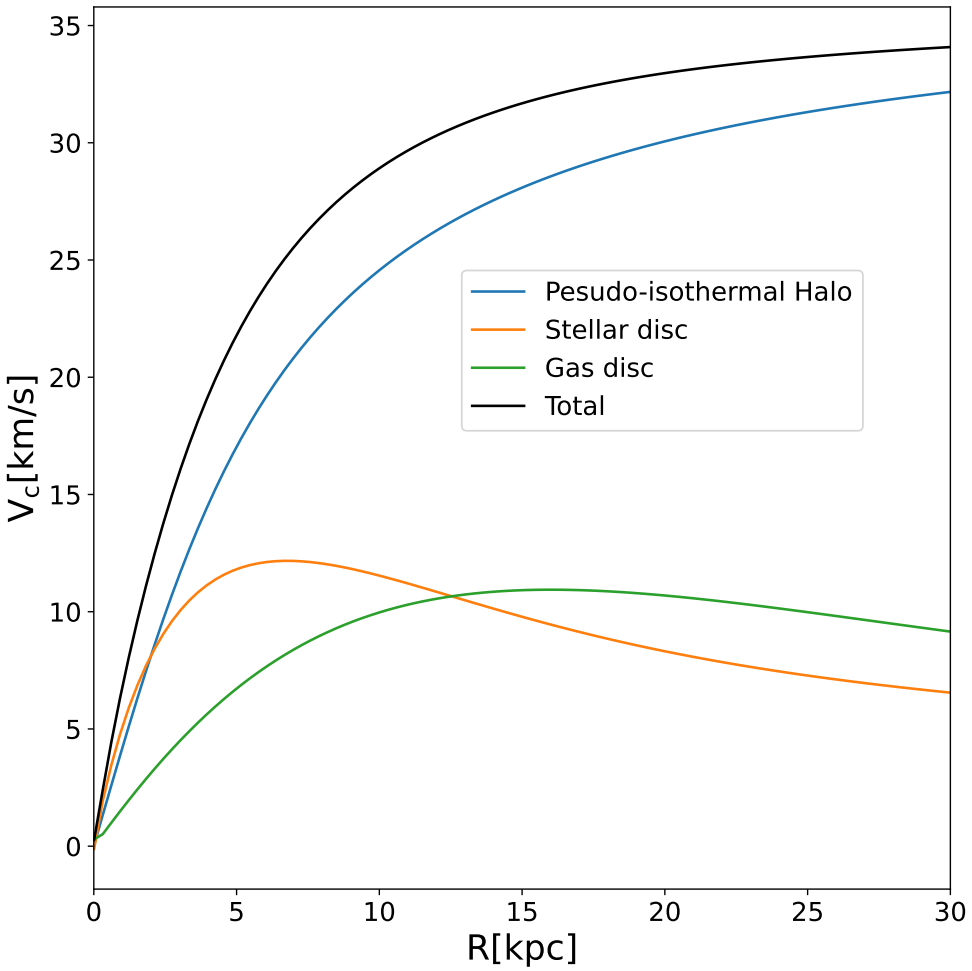

Figure 4.11: Circular velocity V_c for each fixed component of our model. The black line is the total contribution, the pseudo-isothermal halo is the blue line, the stellar disc is the yellow line, and the gas disc is the green line. The contribution from the gas disc is merely illustrative, as here the disc is considered thin, so it is not the final contribution, which also depends on the scale-height.

4.3.1 Results for case IIC

We now show the result obtained for case IIC with our 5 different models. The normalized vertical density profile is shown in Fig. 4.12, and similar to what we have in case IC (Section 4.2.1), the peak can shift from $z = 0$ for both models IIC-20 and IIC-30. However, we observe a fundamental difference: the mass is much less concentrated at small radii compared to what we see in Fig. 4.3, while the opposite is true for larger radii. The reason for this is the absence of the bulge: the gravitational potential well due to the pseudo-isothermal halo is deeper than the one due to the NFW halo, however, at small radii, the bulge contribution to the potential is enough to result into a deeper total potential well than the one we find in our second mock galaxy. In Fig. 4.13 we show the disc scale-height for our models, and we see something similar to what we observe for the density: compared to Fig. 4.4, the values at small radii are larger, but for larger radii the opposite holds true. Unlike case IC, this time both models IIC-20 and IIC-30 have a lower disc scale-height compared to the IICIso one, and models IIC+20 and IIC+30 slow down their growth slightly later compared to models IC+20 and IC+30. The normalized vertical pressure profile is shown in Fig. 4.14, where we see that the gradient is always negative, as it is required to keep the hydrostatic equilibrium. We once again also show the profile for the vertical Brunt-Väisäla frequency N_z squared in Fig. 4.15, finding once more that for models IIC-20 and IIC-30 it can have negative values, which may violate the Solberg-Høiland criterion.

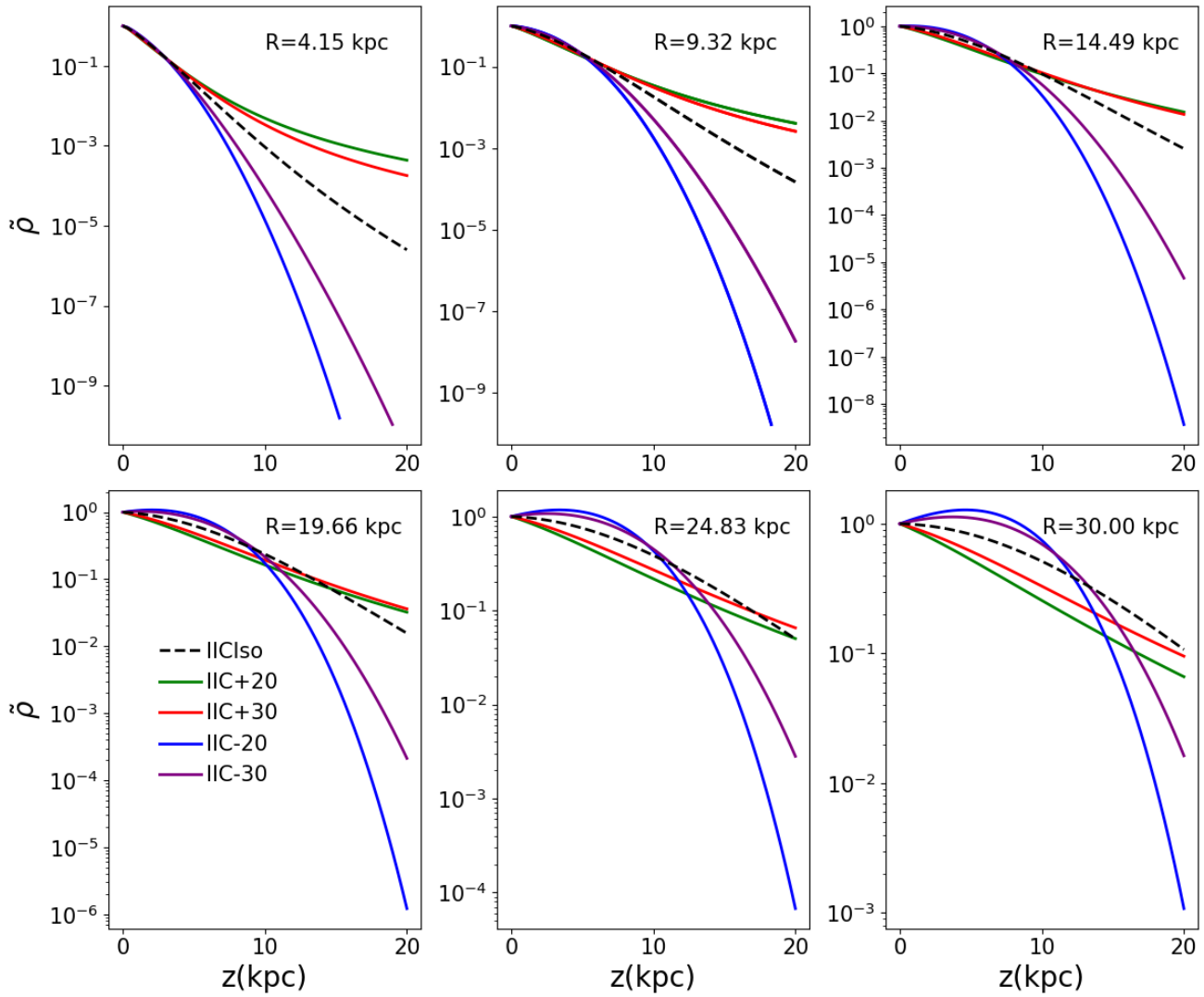

Figure 4.12: The same as Fig. 4.3, but for case IIC.

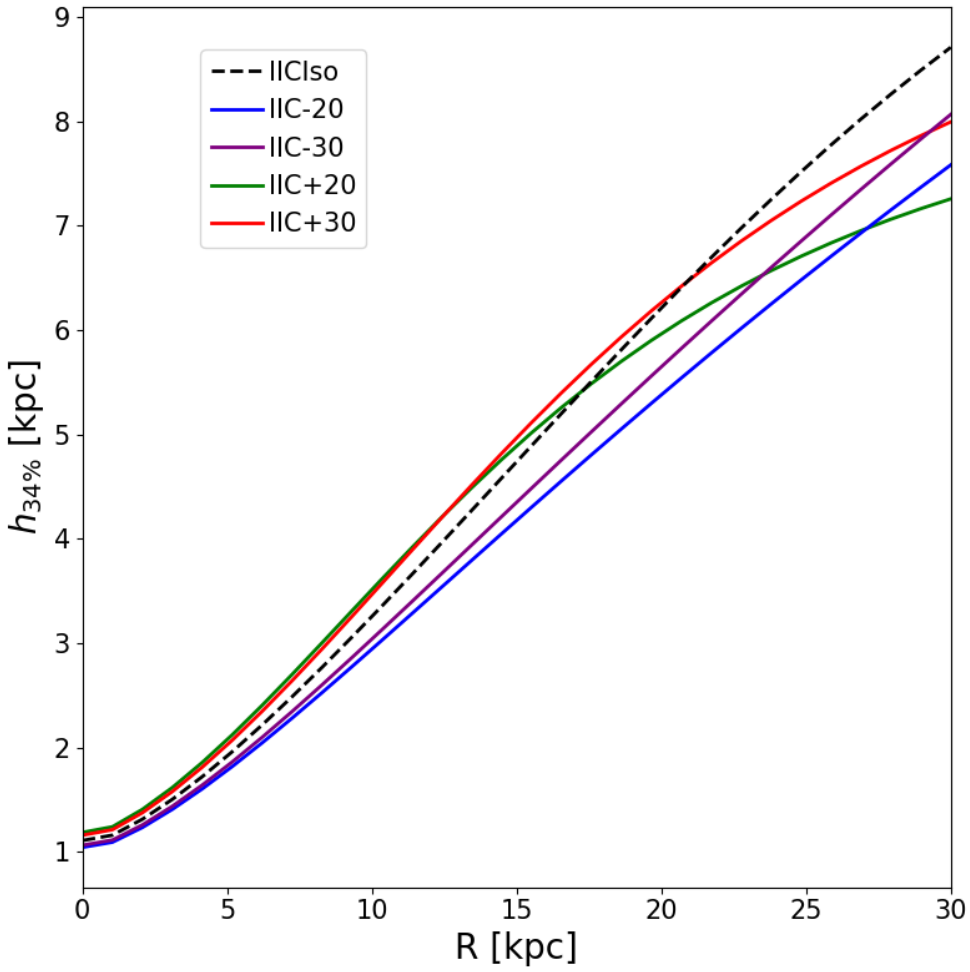

Figure 4.13: The same as Fig. 4.4, but for case IIC.

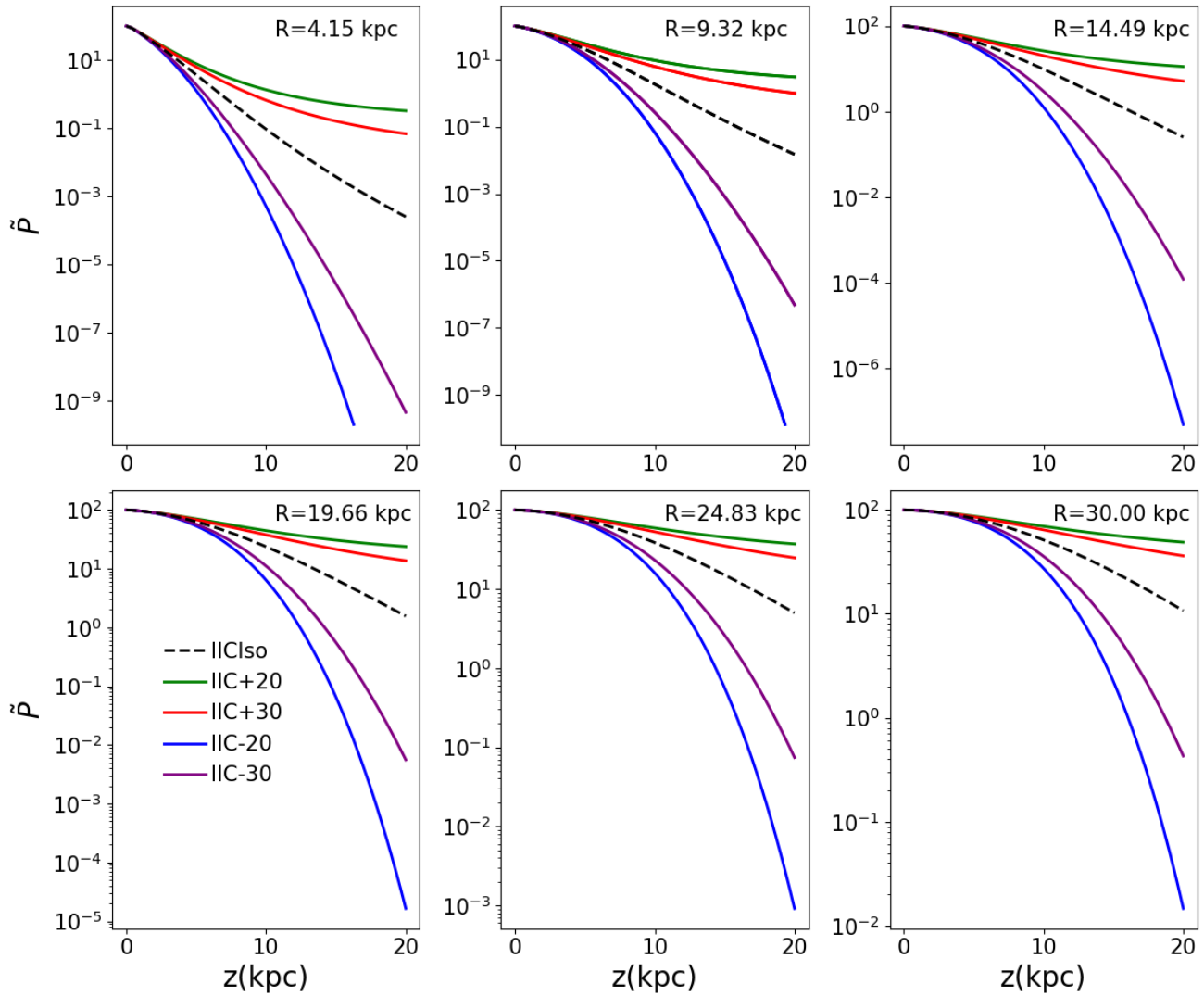

Figure 4.14: The same as Fig. 4.5, but for case IIC.

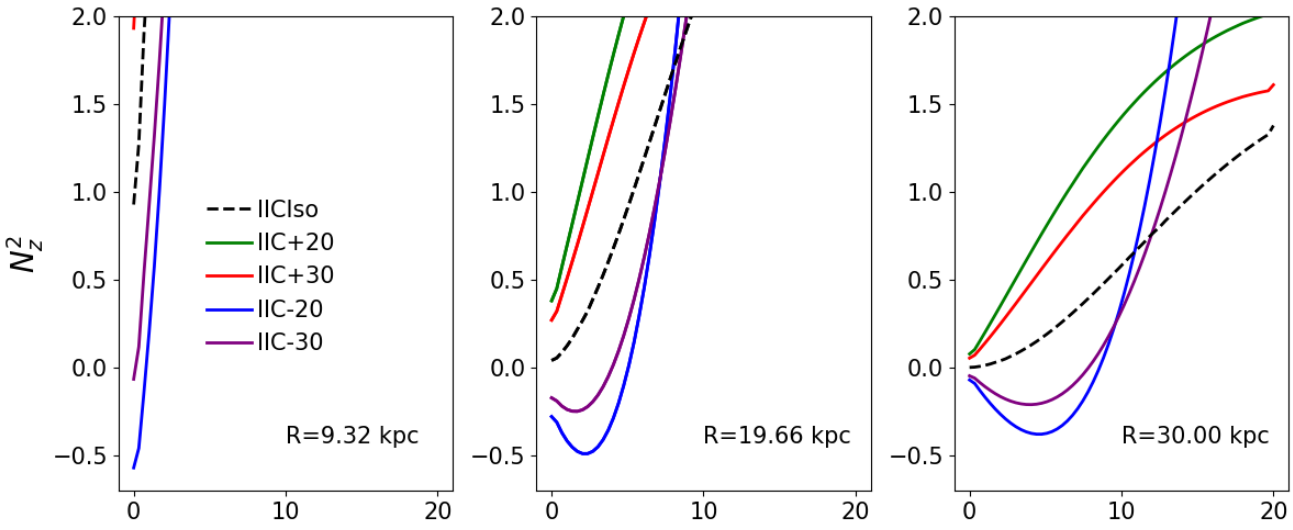

Figure 4.15: The same as Fig. 4.6, but for case IIC.

4.3.2 Results for case IIR

In this subsection, we present our case IIR, and the results for every model. We show the normalized vertical density profile $\tilde{\rho}$ in Fig. 4.16: similar to what we find for case IR (Section 4.2.2), the IIR-20 and IIR-30 models have the peak shifted from $z = 0$, and the IIR+20 and IIR+30 models have a slower decrease compared to the IIRIso model, while the opposite is true for the IIR-20 and IIR-30 models. This means that the mass is more concentrated for models that have a velocity dispersion that decreases with z. Similar to what we observe for the density in case IIC (Section 4.3.1), at smaller radii the mass is less concentrated when compared to what we see in Fig. 4.7, while the opposite happens at larger radii, witnessing once again the effect lacking the bulge can cause. Of course, we see this affects the scale-height as well: as we can see in Fig. 4.17, compared to Fig. 4.8, we have higher values for $h_{34\%}$ at smaller radii, but smaller for larger radii. Just as we commented in Section 4.2.2, we can see how the models IIR+20 and IIR+30 have a scale-height that lies above the one we find for IIRIso, while the opposite holds true for models IIR-20 and IIR-30. We show the pressure in Fig. 4.18, and just like what we have seen for the other 3 cases we see that the vertical hydrostatic equilibrium is kept. Finally, in Fig. 4.19 we show the vertical Brunt-Väisäla frequency squared N_z^2, which, just as we have seen in the previous sections, can be negative for certain values of R and z for our IIR-20 and IIR-30 models, both of which have a $\sigma(R, z)$ that decreases along z, hence we may violate the Solberg-Høiland criterion.

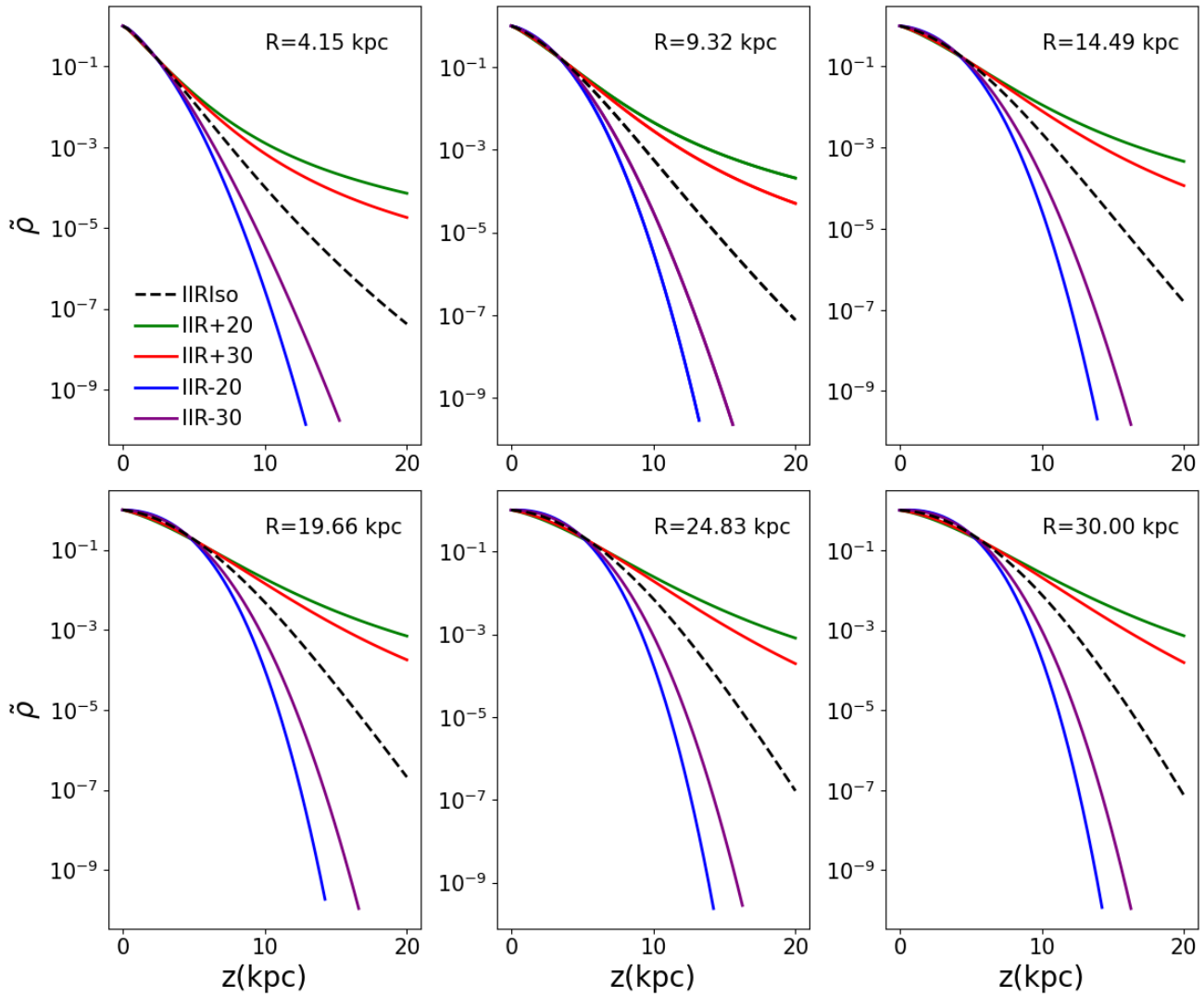

Figure 4.16: The same as Fig. 4.3, but for case IIR.

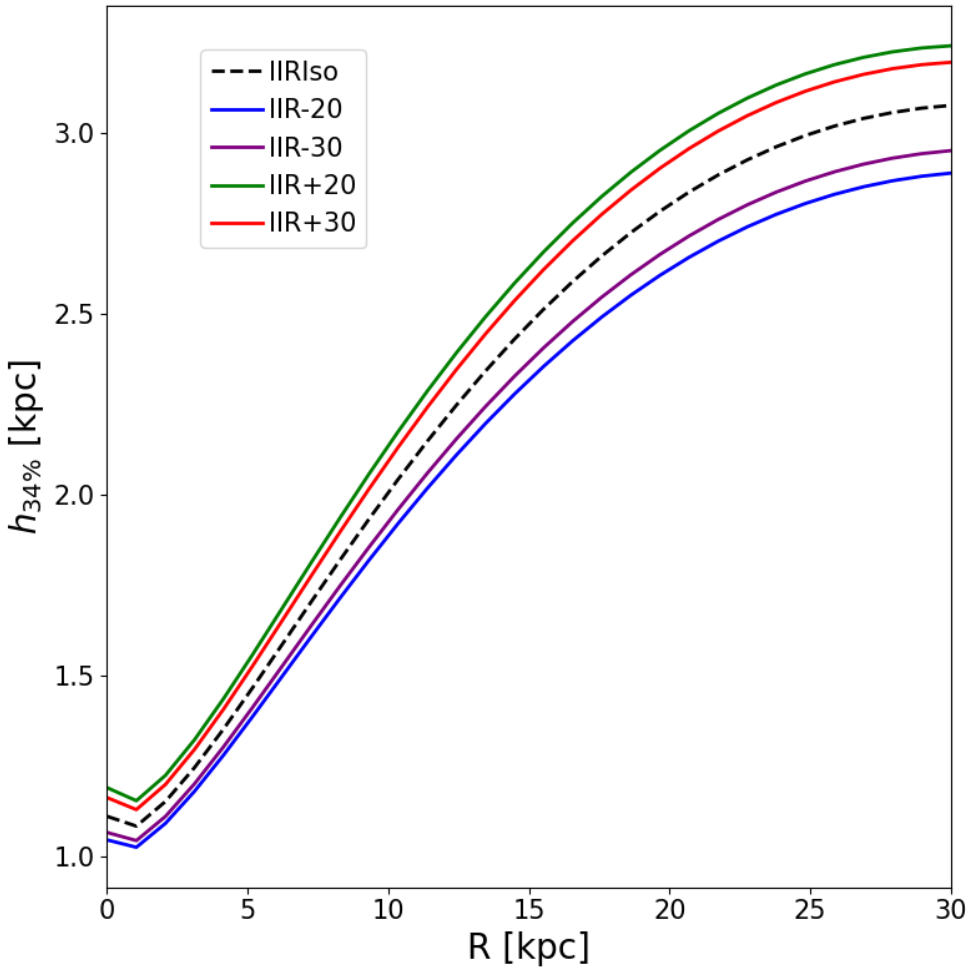

Figure 4.17: The same as Fig. 4.4, but for case IIR.

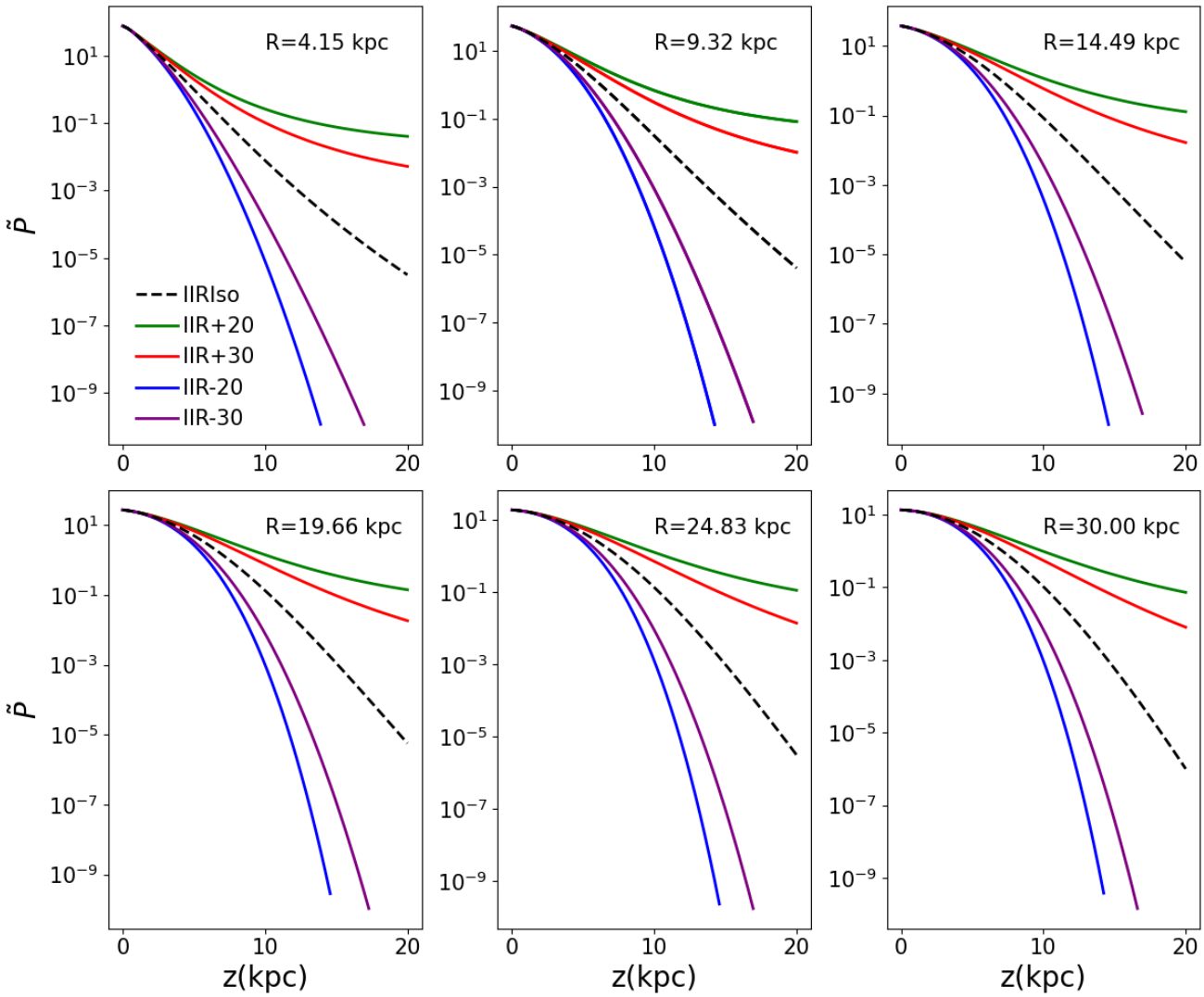

Figure 4.18: The same as Fig. 4.5, but for case IIR.

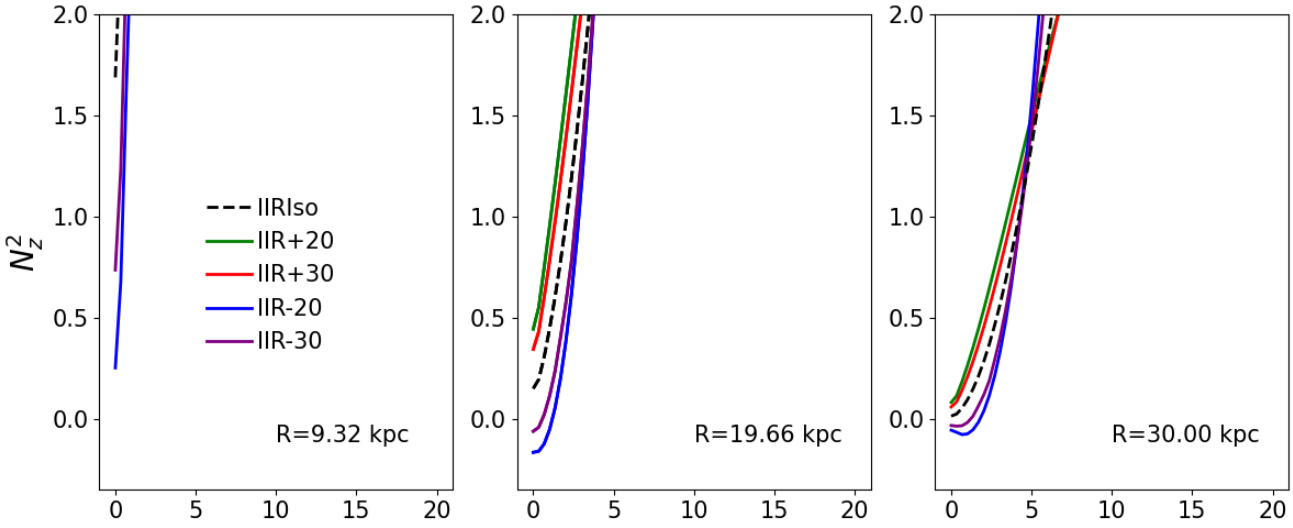

Figure 4.19: The same as Fig. 4.6, but for case IIR.

Chapter 5

The Milky Way

This chapter is dedicated to the modelling of the vertical distribution of the HI disc of our galaxy, the Milky Way. In Section 5.1 we present the method used by Marasco et al. (2017) to determine the gas distribution and kinematics, which were obtained by modelling the HI emission-line datacubes from the Leiden-Argentine-Bonn (LAB) survey (Kalberla et al., 2005), and then we describe the method used by Kalberla et al. (2007) to find the observed disc $h(R)$ profile. In Section 5.2 we describe our dynamical model for the Milky Way, mostly following the approach used in Bacchini et al. (2024), and we present the different profiles we use for the velocity dispersion. Section 5.3 is where we describe our method to calculate the $h(R)$ profile, and present the parameters and nomenclature for each case we study, while we present the obtained results in Section 5.4, comparing them to literature values (e.g. Kalberla et al. (2007)). Finally, in Section 5.5, we discuss our findings and their implications.

5.1 The method and the model

5.1.1 The gas distribution and kinematics by Marasco et al. (2017)

We use the gas surface density and the radial velocity dispersion derived by Marasco et al. (2017), using a hanning-smoothed[1] version of the LAB all-sky 21-cm survey (Kalberla et al., 2005). The hanning smoothing is a technique used in radio observations to increase the signal-to-noise ratio at the expense of the spectral resolution. It consists on mixing the signal from adjacent channels with proper weights that assure an increase of the SNR by a factor of ≈ 1.6. At the same time,

[1] Named after the Austrian meteorologist Julius von Hann

this causes adjacent channels to not be independent anymore, reducing the spectral resolution of about a factor 2. Marasco et al. (2017) assumed the Galactic disc can be decomposed into a series of concentric and co-planar rings, that the vertical distribution of the gas can be approximated with a Gaussian profile, and that the kinematics do not change with z. This means the gas is described by four parameters per ring: the rotational velocity v_ϕ, the velocity dispersion σ, the midplane volume density n_0, and the scale height h_s, which is defined as the Half Width Half Maximum of the Gaussian distribution. These parameters are then fit to the data. First, the gas in the midplane is modelled, following an iterative method similar to the one adopted by Kregel and Der Kruit (2004); in particular, they determine a synthetic brightness temperature profile $T_B(\nu)$ (Marasco et al., 2017, Sec. 2.3), with ν being the line-of-sight velocity in the local standard of rest, at a given Galactic longitude l at a fixed latitude $b = 0°$, then they fit it to the observed data. This method is thus applied to all rings, moving towards the Galactic centre, to determine the values of the parameters recursively. To model the gas above the midplane the process is similar, the only difference is that this time instead of a single line the latitude-velocity $(b - v)$ slice $T_B(b, \nu)$ is modelled.

5.1.2 Data analysis and method of Kalberla et al. (2007)

Same as Marasco et al. (2017), this is data analysis based on the LAB HI line survey (Kalberla et al., 2005). However, this time the original telescope data is used, instead of the hanning-smoothed version, which allows them to keep the original spectral resolution at the expense of losing the fainter emission from the less dense zones. Basically, first they determine which of the observed brightness temperature $T_B(l, b, \nu)$ profiles show contribution to a volume element centered on R_0, z_0, ϕ_0, then for each profile the column densities are calculated and turned into volume densities $n(R, z, \phi)$ by dividing by the path length. The survey grid is in (l,b,ν)-coordinates, but to analyze Galactic properties it is easier to use cylindrical coordinates, so they use the following mapping functions:

$$l = \sin^{-1}\left[\frac{R}{d}\sin\phi\right], \tag{5.1.1}$$

$$b = \tan^{-1}\left(\frac{z}{d}\right), \tag{5.1.2}$$

$$\nu = \sin l \cos b \left[\frac{R_0}{R} v_{\rm rot}(R, z) - v_{\rm rot,0}\right] + v_{\rm ell}(R)\cos\phi\left(1 - \frac{R_0^2}{R^2}\sin^2 l\right)^{1/2}\cos b, \tag{5.1.3}$$

where $v_{\rm rot,0}$ and R_0 are 220 km s^{-1} and 8.5 kpc respectively, while d is the projection onto the plane of the disc of the distance between the Sun and the point being investigated; $v_{\rm ell}$ is a parametrization of the ellipticity of the orbit and can vary with the Galactocentric radius. Using Eqs. (5.1.1)–(5.1.3), they construct $T_B(R,z,\phi)$ from to $T_B(l,b,\nu)$, and from the former they can recover $n(R,z,\phi)$. The procedure used is the same as the one described in Levine et al. (2006), but here $v_{\rm rot}(R)$ is replaced by a generalized rotation law $v_{\rm rot}(R,z)$, as they do not always assume cylindrical rotation, unlike Marasco et al. (2017). For the conversion of $T_B(l,b,\nu)$ to $n(R,z,\phi)$ it is necessary to assume a rotation curve; in Kalberla et al. (2007), they study how different rotation curves, corresponding to different mass models, may affect the results. The $n(R,z,\phi)$ distribution was calculated and interpreted for $0 < R < 40$ kpc, $-15 < z < 20$ kpc at a resolution of $\Delta R = 100$ pc, $\Delta z = 100$ pc, and $\Delta\phi = 1°$, but then data originating from $R < 3.5$ kpc was discarded because this region is affected by ambiguities due to large velocity dispersions. In addition, they flagged data at latitudes $|b| > 30°$ and with velocity in Local Standard Rest $|v_{\rm LSR}| < 10$ km s^{-1}. Once $n(R,z,\phi)$ is obtained, one can find the first three moments: the surface density Σ, the first moment, z_0, which represents the midplane, and the second moment $\sigma_{\rm II}$, which represents the disc scale-height.

When observing the HI disc, we usually detect some extraplanar gas that is not part of the actual HI disc (see Fraternali et al., 2002). In Kalberla et al. (2007) they want to focus solely on the HI disc, so they need a way to remove this excess component, which they expect to be mainly present in the tails of the gas distribution. Their idea is the following: they assume the gas in the HI disc to be in a distribution similar to a Gaussian one; if one filters the mass outside the range $z_0 - 2.35\sigma_{\rm II} < z < z_0 + 2.35\sigma_{\rm II}$, for a Gaussian distribution the excluded mass would be around 2%, however, if the discarded amount is bigger, this might mean something that is not part of the HI disc is also being eliminated. For this reason, they do a first estimate of the three moments, then discard the data outside the range $z_0 - 2.35\sigma_{\rm II} < z < z_0 + 2.35\sigma_{\rm II}$, then from the remaining parts of the data $\Sigma(R,\phi)$, $z_0(R,\phi)$, and $\sigma_{\rm II}(R,\phi)$ are determined again. With this method, on average, they discard more than twice the amount of gas that one would exclude using a Gaussian distribution, so they conclude that they are indeed eliminating extraplanar gas. We are interested in particular in the second moment, $\sigma_{\rm II}(R,\phi)$, which they use to calculate from the data the average $h(R)$ profile $h(R) = f\langle\sigma_{\rm II}(R,\phi)\rangle$, with $f = \sqrt{2\ln 2}$, in order to mimic the HWHM of the HI layer, allowing for an easy comparison with the literature values. The $h(R)$ profile they find from $\sigma_{\rm II}$ is essentially an observed profile, as it is calculated from the volume densities derived from the observational data; it is important, however, to understand that in order to obtain $n(R,z,\phi)$, they first need to

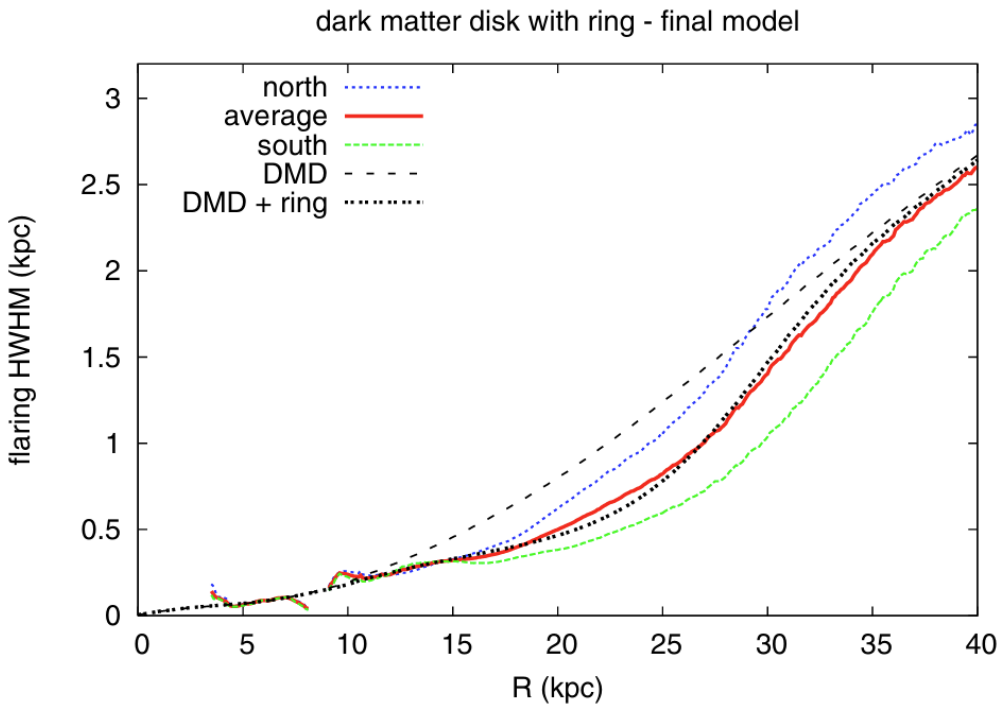

Figure 5.1: Observed mean HWHM flaring (thick red line), applying the rotation curve of Kalberla et al. (2007) best-fit model. The dotted blue and green lines give the flaring in the northern and southern hemispheres, respectively. The best-fit flaring model, containing dark matter disk and ring, is plotted with a black dotted line. The flaring curve from the initial dark matter disk model (without ring) is shown for comparison (black dashed).

define a rotation curve. Depending on the chosen $v_{\rm rot}(R, z)$ the resulting observed $h(R)$ changes, so while it is not a purely theoretical quantity, it is still model-based. In Kalberla et al. (2007), they present different dynamical models; for each one of them, they determine the rotation curve and then show a comparison between the observed $h(R)$ profile obtained from the data and the expected $h(R)$ profile found theoretically assuming vertical hydrostatic equilibrium, checking if the latter can reproduce the former. They find that the best possible result (shown in Fig. 5.1) is obtained using a model that contains a DM disc (instead of the more classic spheroidal halo) combined with a DM ring. As our model contains a spherical halo, we are going to compare our results to the observed $h(R)$ profile they obtain when assuming a flat rotation curve with $v_{\rm rot} = 220$ km s^{-1} (see Kalberla et al., 2007, Fig. 3), hereafter referred to as Kalberla_reference, and when using a rotation curve derived from a model with an isothermal DM spheroidal halo (see Kalberla

et al., 2007, Fig. 4), which will be called Kalberla_sphere from now on, and is described by

$$\rho(R,z) = \rho_0 \left[\frac{R_c^2}{R_c^2 + R^2 + (z/q)^2} \right], \tag{5.1.4}$$

where ρ_0 is the density at the center, and R_c is the core radius, and $q = 1$ is the flattening parameter. In Kalberla et al. (2007), the $h(R)$ profile expected for the model described by Eq. (5.1.4) does not match the one derived from the data. They test different values of q, but the mismatch is still present, and they conclude that a halo described by a single constant q parameter does not match the observations if one considers a broad range of galactocentric distances.

5.2 The galaxy model

In order to confront our results with the models present in Kalberla et al. (2007) we first need to define a dynamical model of the Milky Way, as well as define the profiles of the velocity dispersion.

5.2.1 The dynamical model

The mass models for both the DM halo and the stellar discs were taken from McMillan (2017). We use a spherical halo described by a Navarro-Frenk-White density profile (Navarro et al., 1996), which is

$$\rho_{DM} = 4\rho_{DM,s} \left(\frac{r}{r_s} \right)^{-1} \left(1 + \frac{r}{r_s} \right)^{-2}, \tag{5.2.1}$$

where we set the scale radius $r_s = 19.6$ kpc, while we have $\rho_{DM,s} = 2.125 \times 10^6$ $\mathrm{M_\odot kpc^{-3}}$, with $M_{DM}(R = 30\mathrm{kpc}) = 2.61 \times 10^{11}$ $\mathrm{M_\odot}$, and $M_{DM}(R = 500\mathrm{kpc}) = 1.86 \times 10^{12}$ $\mathrm{M_\odot}$. We consider two stellar discs with finite thickness, one thin and one thick. Both are described using an exponential profile along the radial coordinate, and a sech^2 profile along z, following van der Kruit et al. (1981):

$$\rho_\star(R,z) = \rho_{\star,0} \exp\left(-\frac{R}{R_\star} \right) \mathrm{sech}^2(z/z_\star), \tag{5.2.2}$$

where $\rho_{\star,0} = \Sigma_{\star,0}/(2z_\star)$ is the central density, $R_\star$ is the radial scale length, and $z_\star$ is the vertical scale height. The parameters for each disc are reported in Table 5.1.
The bulge is modelled as a Plummer sphere (Plummer, 1911) (Di Matteo et al., 2015)

$$\rho(R) = \rho_0 \left(1 + \left(\frac{R}{R_s} \right)^2 \right)^{-5/2}, \tag{5.2.3}$$

	Stellar discs parameters		
	$\Sigma_{\star,0}[\mathrm{M}_\odot\mathrm{kpc}^{-2}]$	$R_\star$[kpc]	$z_\star$[kpc]
Thin disc	8.9×10^8	2.50	0.30
Thick disc	1.8×10^8	3.02	0.90

Table 5.1: Parameters for the thin and thick stellar discs of the Milky Way

with $\rho_0 = \frac{3M_{\mathrm{Bulge},0}}{4\pi R_s^3}$. We use $M_{\mathrm{Bulge},0} = 9 \times 10^9$ $\mathrm{M}_\odot$ and $R_s = 1.3$ kpc, and we have $M_{\mathrm{Bulge}}(R = 30\mathrm{kpc}) = 9.03 \times 10^9$ $\mathrm{M}_\odot$, and $M_{\mathrm{Bulge}}(R = 50\mathrm{kpc}) = 9.04 \times 10^9$ $\mathrm{M}_\odot$. Finally, for the surface density of the gaseous disc, we adopt a combination of a polynomial and an exponential function:

$$\Sigma(R) = \Sigma_{0,gas} \left(1 + \sum_{i=1}^{N=3} C_i R^i\right) \exp\left(-\frac{R}{R_\Sigma}\right), \tag{5.2.4}$$

where $\Sigma_{0,gas}$ is the central surface density, C_i are the polynomial coefficients, and R_Σ is the scale radius. To obtain the parameters (which are reported in Table 5.2), we fit Eq. (5.2.4) to the radial profile of the measured gas surface density obtained by Marasco et al. (2017).

$\Sigma_{0,gas}[\mathrm{M}_\odot\mathrm{kpc}^{-2}]$	R_Σ [kpc]	C_1	C_2	C_3
9.18×10^6	2.041	1.0	-1.4	0.50

Table 5.2: Parameters obtain from fitting Eq. (5.2.4) to the data by Marasco et al. (2017).

In Fig. 5.2 we report the different contributions to the circular velocity V_c for each component described above. It can be clearly seen that for $R \gtrsim 7$ kpc the biggest contribution comes from the DM halo, followed by the stellar thin disc, while the bulge is the one with the smallest contribution, aside from the gas disc. The contribution from the latter is merely illustrative, as here we do not know the vertical structure yet, however it is small enough that we can expect the final V_c to be essentially the same. Moreover, it can be seen that the gas disc circular velocity has negatives values. The reason is that the circular velocity shown for each component is just a measure of the centripetal acceleration caused by the mass distribution of each component, and by convention we use a negative sign when the force is going outwards; in the case of the gas disc, the profile used for the surface density has a density peak in $R \neq 0$, which results in some negative values for the circular velocity.

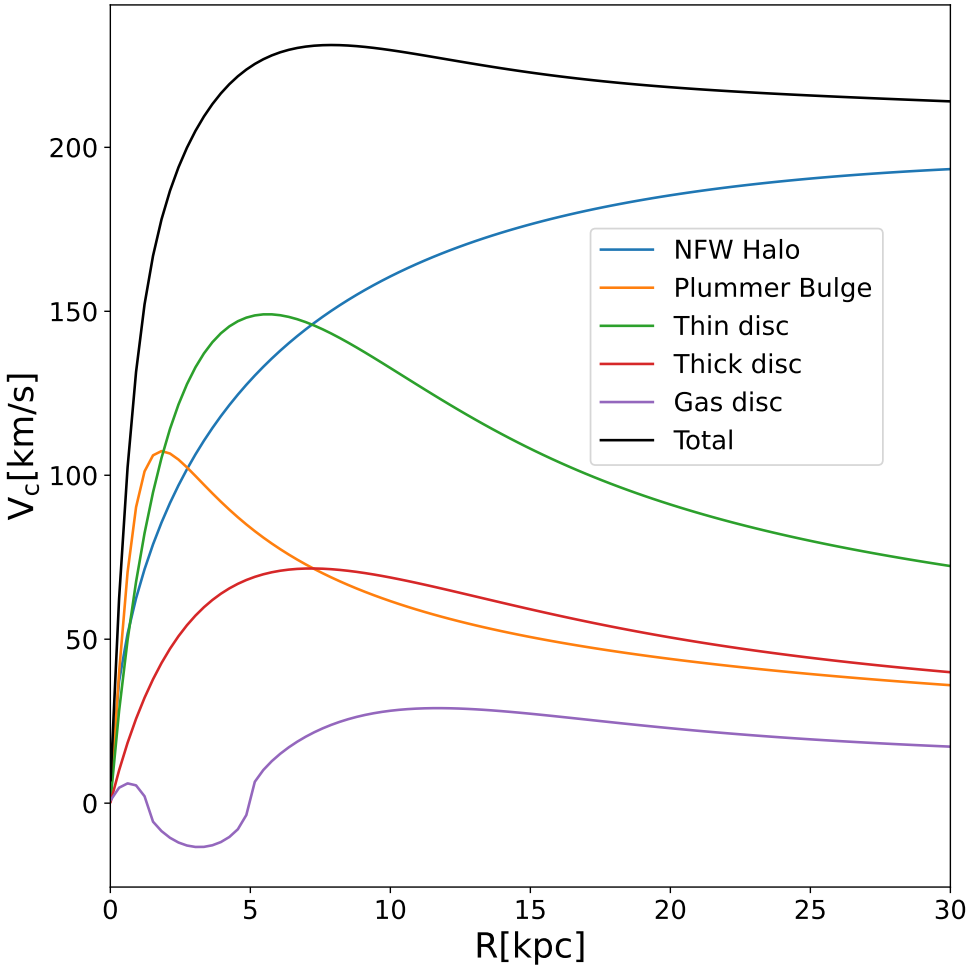

Figure 5.2: Circular velocity V_c for each fixed component of our model. The black line is the total contribution, the NFW halo is the blue line, the Plummer bulge is the yellow line, the thin stellar disc is the green line, the thick stellar disc is the red line, and the gas disc is the purple line. The contribution from the gas disc is merely illustrative, as here the disc is considered thin, so it is not the final contribution, which also depends on the scale-height.

5.2.2 The gas velocity dispersion

For the purpose of this work, we are going to use both a constant velocity dispersion along the cylindrical radius and one that changes with R. The former is set to a value $\sigma_{\rm const}$, and when we add the dependence on z it becomes

$$\sigma(z) = \sigma_{\rm const}\ \exp\left(s\frac{|z|}{z_\sigma}\right), \tag{5.2.5}$$

where $s = \pm 1$, and z_σ is a generic scale height.

For the latter, we obtain the radial profile of the gas velocity dispersion by fitting our data with the following profile

$$\sigma(R) = \sigma_a \exp\left(-\frac{R}{R_a}\right) + \sigma_b \exp\left(-\frac{R}{R_b}\right). \tag{5.2.6}$$

We obtain from the fit of the data from Marasco et al. (2017) the following parameters: $\sigma_a = 17.3$ km s^{-1}, $R_a = 0.55$ kpc, $\sigma_b = 11.3$ km s^{-1}, and $R_b = 22$ kpc; with these choices the velocity dispersion has an initial sharp decrease, going from around $25 - 30$ km s^{-1} in the Galactic centre to ~ 10 km s^{-1} at around $R = 1.5$ kpc. This is the profile we use when modelling an isothermal vertical distribution. When we consider a generic vertical distribution, we define the velocity dispersion using the following

$$\sigma(R,z) = \sigma_a \exp\left(-\frac{R}{R_a}\right) \exp\left(s\frac{|z|}{z_\sigma}\right) + \sigma_b \exp\left(-\frac{R}{R_b}\right) \exp\left(s\frac{|z|}{z_\sigma}\right), \tag{5.2.7}$$

where $s = \pm 1$, and z_σ is a generic scale height.

While Eq. (5.2.6) fits pretty well our data (see Fig. 5.3), it is important to note that the data by Marasco et al. (2017) does not cover radii larger than $R \sim 8$ kpc. Since we want to study the behaviour of the gas disc at larger values of R, we also want a velocity dispersion that does not necessarily follow Eq. (5.2.6) at all radii. The reason for this is that the conventional value of the velocity dispersion for the HI gas in the Milky Way is ~ 9.2 km s^{-1} (Olling et al., 2000), but using Eq. (5.2.6) at $R = 20$ kpc we obtain $\sigma \approx 4.6$ km s^{-1}, half of the literature values. It stands to reason that we can expect to see, after a certain value of the radius, an underestimate of the disc scale height. Hence why we also study a model with a velocity dispersion in the form of

$$\sigma(R) = \begin{cases} \sigma_a \exp\left(-\dfrac{R}{R_a}\right) + \sigma_b \exp\left(-\dfrac{R}{R_b}\right) & \text{for } R < R_{\rm crit}, \quad (5.2.8a) \\ \sigma_{\rm const} & \text{for } R \geq R_{\rm crit}, \quad (5.2.8b) \end{cases}$$

with $R_{\rm crit}$ the value of the radius where we expect Eq. (5.2.6) to underestimate the disc scale height, and with $\sigma_{\rm const}$ a constant value of the velocity dispersion.

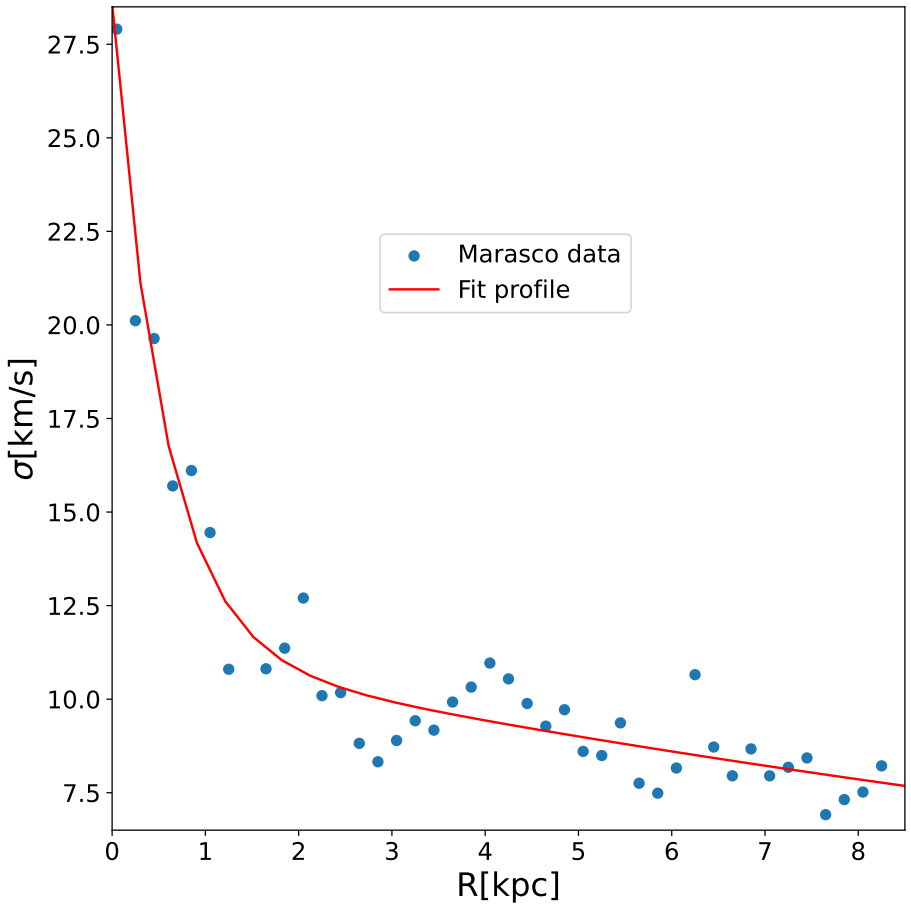

Figure 5.3: The radial profile of the velocity dispersion σ for the Milky Way. The blue dots are the data obtained by Marasco et al. (2017), while the red line shows the profile we use to fit the data, which is described in Eq. (5.2.6).

For a gaseous disc with a generic non-isothermal vertical distribution, Eq. (5.2.8) becomes

$$\sigma(R,z) = \begin{cases} \sigma_a \exp\left(-\dfrac{R}{R_a}\right) \exp\left(s\dfrac{|z|}{z_\sigma}\right) + \sigma_b \exp\left(-\dfrac{R}{R_b}\right) \exp\left(s\dfrac{|z|}{z_\sigma}\right) & \text{for } R < R_{\text{crit}}, \quad (5.2.9a) \\ \sigma_{\text{const}} \exp\left(s\dfrac{|z|}{z_\sigma}\right) & \text{for } R \geq R_{\text{crit}}, \quad (5.2.9b) \end{cases}$$

where $s = \pm 1$, and z_σ is a scale height.

Equation (5.2.8) may still however not sufficient to properly describe the $h(R)$ profile of our galaxy: from Kalberla et al. (2007), we know that the $h(R)$ profile starts to rapidly grow at $R \sim 22$ kpc, and to match this increase it might be necessary to also have a velocity dispersion that increases

with R. We thus present another radial profile for the velocity dispersion:

$$\sigma(R) = \begin{cases} \sigma_a \exp\left(-\frac{R}{R_a}\right) + \sigma_b \exp\left(-\frac{R}{R_b}\right) & \text{for } R < R_{\rm crit}, \quad (5.2.10a) \\ \sigma_{\rm const} & \text{for } R_{\rm crit} \leq R \leq R_{\rm crit,2}, \quad (5.2.10b) \\ \sigma_{\rm const} \exp\left(\frac{R - R_{\rm crit}}{R_\sigma}\right) & \text{for } R \geq R_{\rm crit,2}, \quad (5.2.10c) \end{cases}$$

with $R_{\rm crit,2}$ the value of the radius where the trend of the $h(R)$ profile changes and R_σ is a generic scale length. When we also have the dependence on z, Eq. (5.2.11) becomes

$$\sigma(R,z) = \begin{cases} \sigma_a \exp\left(-\frac{R}{R_a}\right) \exp\left(s\frac{|z|}{z_\sigma}\right) + \sigma_b \exp\left(-\frac{R}{R_b}\right) \exp\left(s\frac{|z|}{z_\sigma}\right) & \text{for } R < R_{\rm crit}, \quad (5.2.11a) \\ \sigma_{\rm const} \exp\left(s\frac{|z|}{z_\sigma}\right) & \text{for } R_{\rm crit} \leq R \leq R_{\rm crit,2}, \quad (5.2.11b) \\ \sigma_{\rm const} \exp\left(\frac{R - R_{\rm crit}}{R_\sigma}\right) \exp\left(s\frac{|z|}{z_\sigma}\right) & \text{for } R \geq R_{\rm crit,2}, \quad (5.2.11c) \end{cases}$$

where $s = \pm 1$, and z_σ is a scale height.

5.3 Our method and models

We follow a method for the calculation of the $h(R)$ profile similar to the one described in Section 5.1.2: once we obtain our vertical density profile $\tilde{\rho}(R,z)/k(R)$, with $k(R)$ defined as we explain in Section 3.2, we find the second moment $\sigma_{\rm II}(R)$ with

$$\sigma^2_{\rm II,first}(R) = \frac{\int_0^{z_{max}} z^2 \frac{\tilde{\rho}(R,z)}{k(R)}\,{\rm d}z}{\int_0^{z_{max}} \frac{\tilde{\rho}(R,z)}{k(R)}\,{\rm d}z}. \quad (5.3.1)$$

We then repeat the calculation, but this time we only integrate up to $z_{up} = 2.35\sigma_{\rm II,first}(R)$, so our second moment becomes

$$\sigma^2_{\rm II}(R) = \frac{\int_0^{2.35\sigma_{\rm II,first}} z^2 \frac{\tilde{\rho}(R,z)}{k(R)}\,{\rm d}z}{\int_0^{2.35\sigma_{\rm II,first}} \frac{\tilde{\rho}(R,z)}{k(R)}\,{\rm d}z}. \quad (5.3.2)$$

Unlike Kalberla et al. (2007), we do not need to find z_0, as we assumed symmetry on the $z = 0$ plane, so for us it is always $z_0 = 0$. We also find how much mass we discard with this method, which we define as

$$\text{Percentage of discarded mass} = 100\left(1 - \frac{\int_0^{2.35\sigma_{\rm II,first}} \frac{\tilde{\rho}(R,z)}{k(R)}\,{\rm d}z}{\int_0^{z_{max}} \frac{\tilde{\rho}(R,z)}{k(R)}\,{\rm d}z}\right). \quad (5.3.3)$$

The reason we execute this cut is however different from the one illustrated in Kalberla et al. (2007): as explained in Section 5.1.2, they apply this filter in order to exclude extraplanar gas, which has a different origin and structure than the gaseous disc. However, in our case, the mass discarded cannot be extraplanar gas, but it is simply related to the shape of the vertical distribution of the density, so depending on whether the mass is more concentrated in a neighborhood of $z = 0$ or if the tails are more relevant we can filter a different amount of gas. The farther the quantity is from 2%, the more our gas distribution deviates from a Gaussian profile.
Finally, same as Kalberla et al. (2007), we define $h(R) \equiv f\sigma_{\rm II}(R)$, with $f = \sqrt{2\ln 2}$.
We show four different cases with four different radial velocity dispersion profiles: case A refers to Eq. (5.2.5), case B to Eq. (5.2.6), case C to Eq. (5.2.8), and case D to Eq. (5.2.11). For each case, we summarize the various parameters in Table 5.3. For each of these cases, we define four different profiles for the vertical component of the velocity dispersion: one which corresponds to having an isothermal vertical distribution, with $s = 0$, called XIso, one with $s = -1$ and $z_\sigma = 5$ kpc, called X-5, and two with $s = +1$, with $z_\sigma = 5$ and 3 kpc respectively, with the first called X+5 and the second called X+3. For each model, we substitute X with the letter corresponding to the case under study; for example, in case A, the models will be called AIso, A-5, A+5, and A+3. The names associated with each profile are explained in Table 5.4. In Fig. 5.4, we show for each case the radial profiles of the velocity dispersion at $z = 1.5$ kpc, using shaded areas that have as upper limit a vertical profile described by models X+3, and as lower limit the one represented by models X-5, while the radial profiles of models XIso are represented by the solid and dashed lines. In the following section, for each model and for each case, we present plots of the normalized vertical density profile (as well as a zoom on the peak to show when it is shifted), the scale height radial profiles before and after filtering, the normalized vertical pressure profiles, and the profiles of the vertical Brunt-Väisäla frequency squared, as well as a plot showing how much mass we discard with our filtering process.

Parameters of the cases								
Case	σ_{const} [km s^{-1}]	σ_a [km s^{-1}]	σ_b [km s^{-1}]	R_a [kpc]	R_b [kpc]	$R_{crit}[kpc]$	$R_{crit,2}[kpc]$	$R_\sigma[kpc]$
A	8.3							
B		17.3	11.3	0.55	22			
C	5.22	17.3	11.3	0.55	22	17		
D	5.22	17.3	11.3	0.55	22	17	22	7.37

Table 5.3: Parameters of the four different cases we show for the Milky Way, each one associated to a different radial profile for the velocity dispersion. In particular: case A refers to Eq. (5.2.5), case B to Eq. (5.2.6), case C to Eq. (5.2.8), and case D to Eq. (5.2.11).

Parameters and names of vertical profiles of σ		
Name	s	z_σ [kpc]
XIso	0	–
X-5	-1	5
X+5	$+1$	5
X+3	$+1$	3

Table 5.4: Names and parameters for the various models associated to a specific vertical profile of the velocity dispersion. The X is a placeholder, and will be substituted by either A, B, C, or D depending on the case being studied.

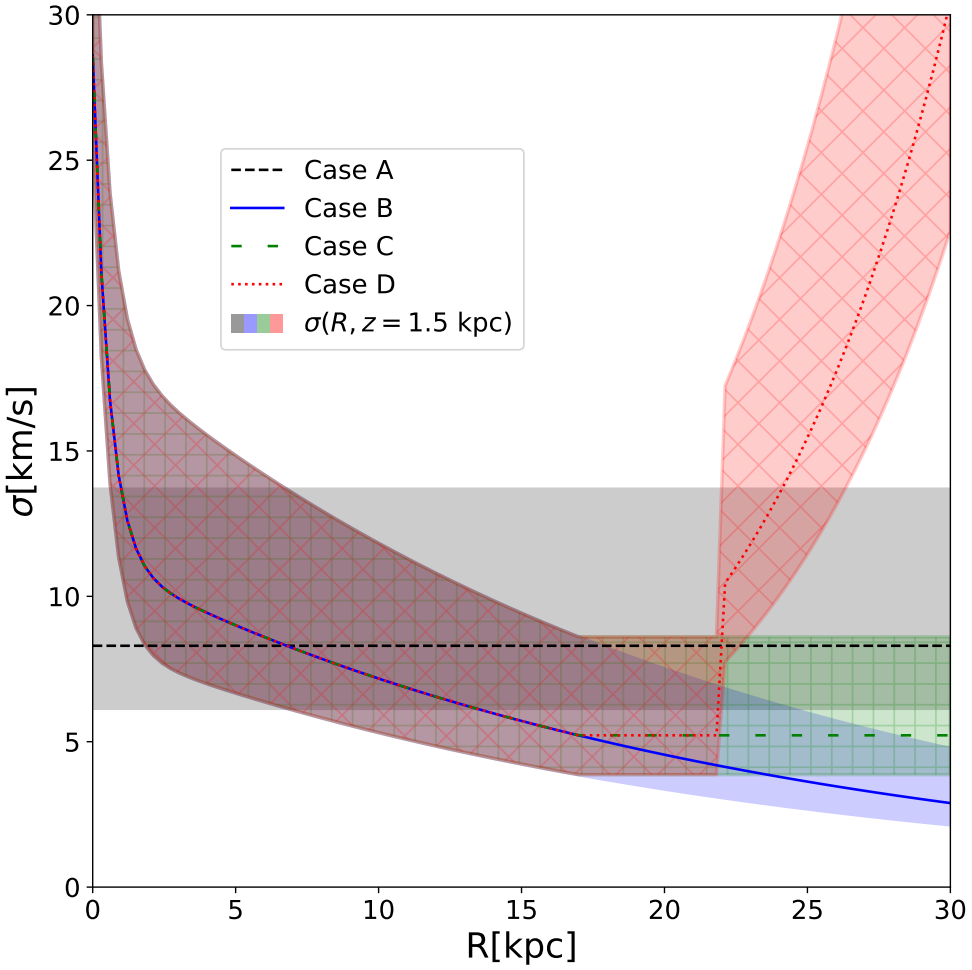

Figure 5.4: Plot showing the four different radial profiles of the velocity dispersion we use. In particular: case A refers to Eq. (5.2.5), case B to Eq. (5.2.6), case C to Eq. (5.2.8), and case D to Eq. (5.2.11). For each case, the shaded area represents the dependence on z, with the upper limit being defined by models X+3, and the lower one by models X-5, all calculated at $z = 1.5$ kpc.

5.4 Results

In the following subsections, we consider separately the four cases (A, B, C, D), and for each case, we present four different models, each one associated to a different vertical profile of the velocity dispersion. For each case and model presented, we use a linear grid of 30 points on the radial axis that goes from 0.05 to 30 kpc, and one of 45 points that goes from 0 to 3 kpc for the vertical axis.

5.4.1 Case A

We first present the case for the constant radial velocity dispersion. Figure 5.5 shows the normalized density profile $\tilde{\rho}$, where we can see, similar to Section 4.2, that with a decreasing velocity dispersion along z (model A-5) the density peak can shift from $z = 0$, but the decrease in the tail is sharper, while for a velocity dispersion that grows along z (models A+5 and A+3) we have the opposite. In Fig. 5.6, to better showcase the difference between the different velocity dispersion profiles, we show a zoom around the peak of the normalized vertical density profile. In Fig. 5.7 and Fig. 5.9 we show the $h(R)$ profile before and after filtering, while in Fig. 5.8 we show the percentage of the mass we excluded when applying our filtering. Looking at model AIso, we can notice how, aside from the smallest radii, we tend to discard between 2% and 4% of the gas mass: the former is equivalent to the case of a Gaussian filter, the latter is what one would exclude using Kalberla et al. (2007) method. On the other hand, models A+3 and A+5 tend to filter more mass, while the opposite holds true for model A-5. This is to be expected, as it reflects the shape of the density, which tends to show that mass is more concentrated when the dispersion velocity grows smaller along the vertical axis. We compare our results to the observed $h(R)$ profile of two cases obtained by Kalberla et al. (2007): the one with a flat rotation curve with $v_{\rm rot} = 220$ km s^{-1} is represented by purple dots, while the model with an isothermal spherical halo of DM is shown with brown stars. We can see that filtering our data causes the difference between our profiles to shrink, but it changes little of the trend. It is clear that, using a constant dispersion velocity along R, we cannot reproduce the data of either model, which is however not surprising: the observed $h(R)$ profile starts with a really shallow growth that then shows an increase at $R \approx 17$ kpc and finally starts to grow really fast after $R \approx 25$ kpc. Using a velocity dispersion that is independent of the radius is expected to produce a gradual radial variation of the scale-height.
In Fig. 5.10 we show the vertical pressure profile, which, as expected, always shows a negative gradient, as it is essential to keep the vertical hydrostatic equilibrium. Figure 5.11 shows a zoom

close to zero of the vertical Brunt-Väisäla frequency squared N_z^2 for three different radii: while for the smallest radii we can see that it is always positive, the same cannot be said for the other two, as a dispersion velocity that decreases along z (model A-5) can result in a range of z where N_z^2 is negative, which could lead to a violation of the Solberg-Høiland stability criterion.

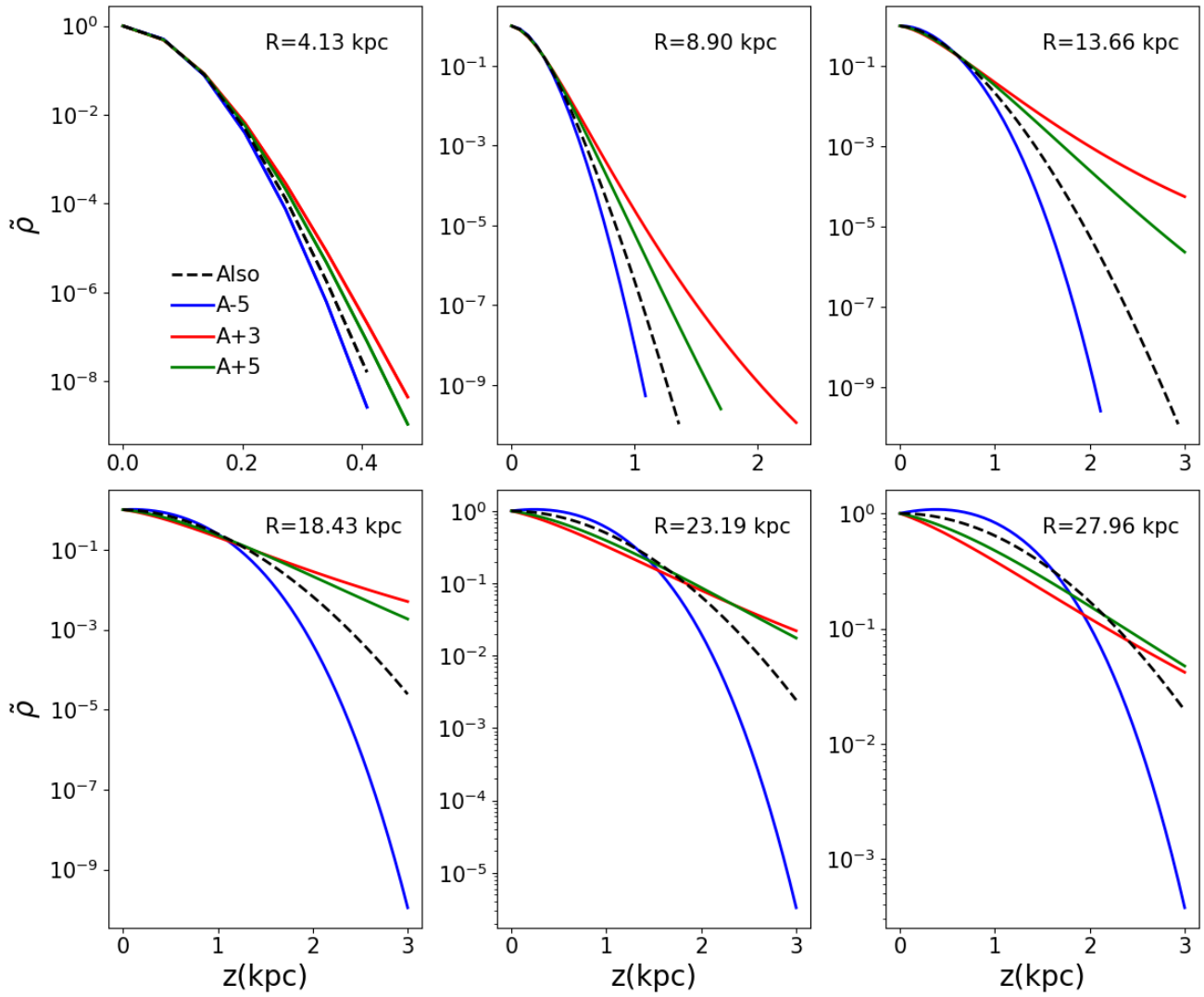

Figure 5.5: Normalized vertical density profile $\tilde{\rho} = \rho(R,z)/\rho(R,0)$ for the Milky Way for the models in case A. The AIso model is the one represented with the black dashed line. The blue one corresponds to model A-5, while the green and red ones to the models A+3 and A+5.

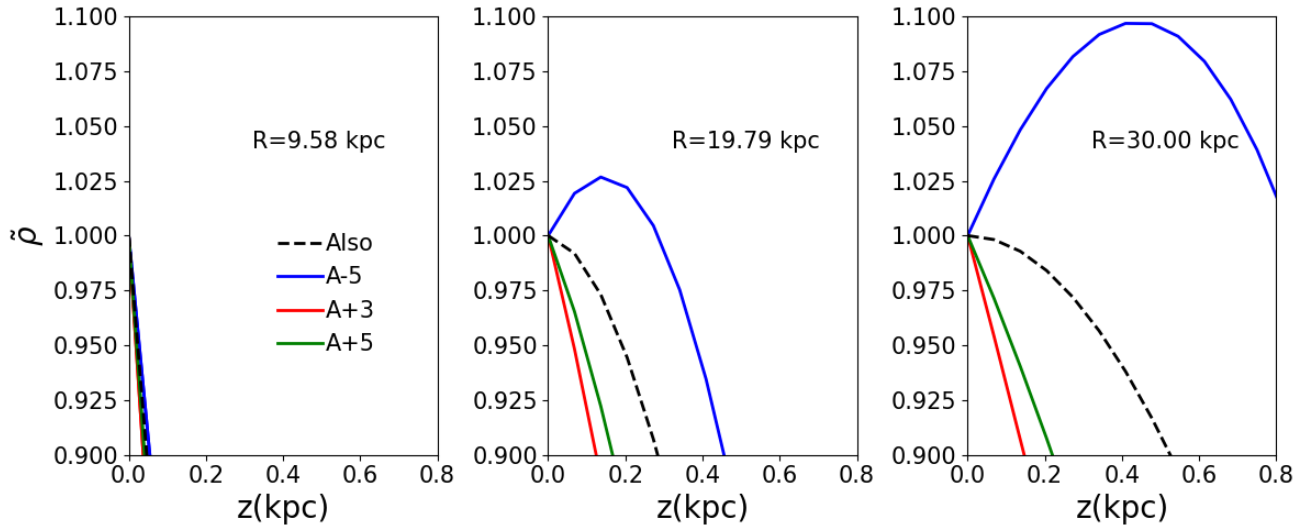

Figure 5.6: Zoom on the peak of the normalized vertical density profile $\tilde{\rho} = \rho(R, z)/\rho(R, 0)$ for the Milky Way for the same models as in Fig. 5.5.

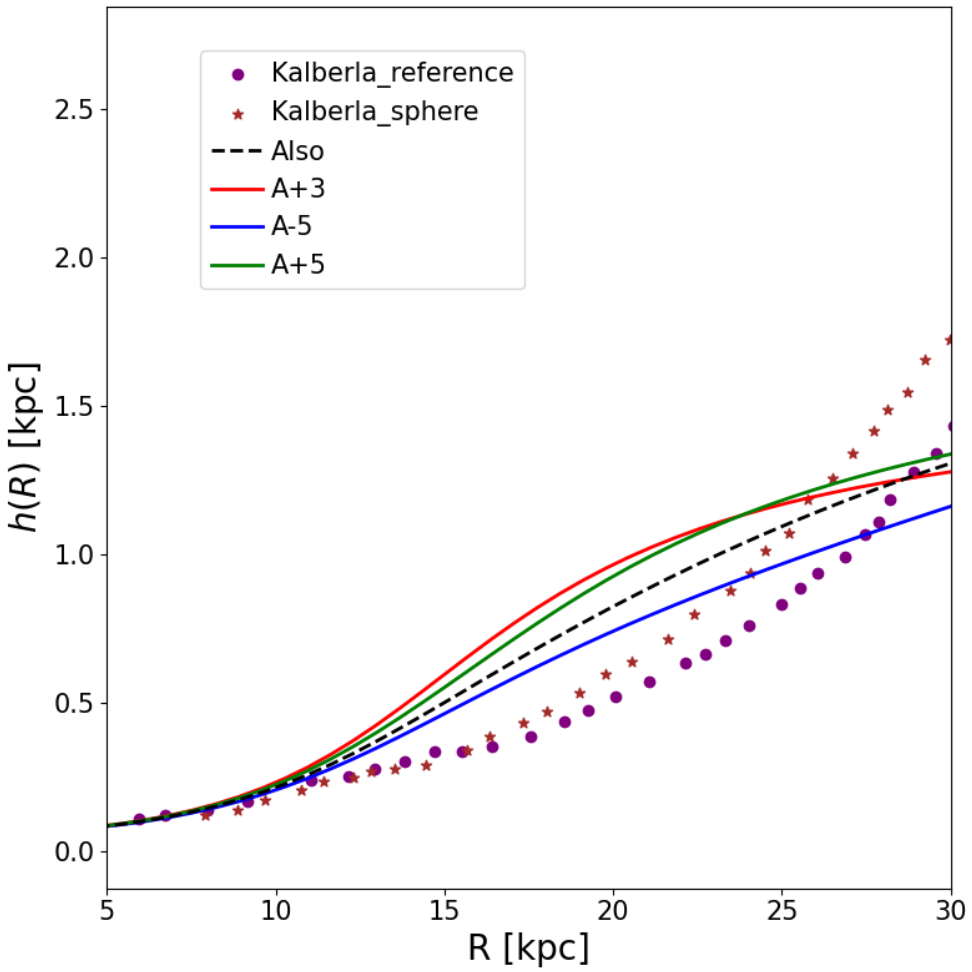

Figure 5.7: Scale height $h(R)$ for the Milky Way as a function of the radius before filtering for the models in case A. The AIso model is the one represented with the black dashed line. The blue one corresponds to model A-5, while the green and red ones to the models A+3 and A+5. The purple points and the brown stars are the observed $h(R)$ profiles obtained by Kalberla et al. (2007); the first is obtained when using a flat rotation curve with $v_{rot} = 220$ km s^{-1}, while the second is obtained when using a rotation curve obtained from a model with the spherical DM halo described by Eq. (5.1.4).

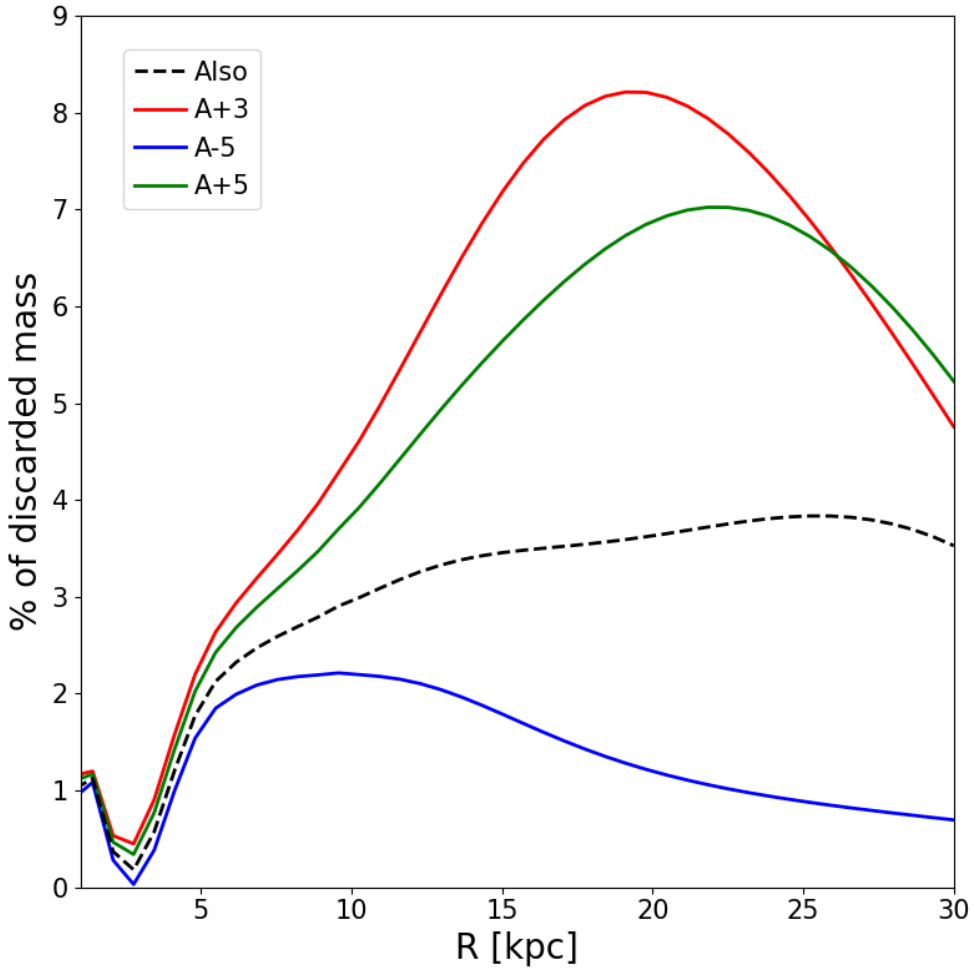

Figure 5.8: Percentage of discarded mass after the process of filtering for the models in case A. The AIso model is the one represented with the black dashed line. The blue one corresponds to model A-5, while the green and red ones to the models A+3 and A+5.

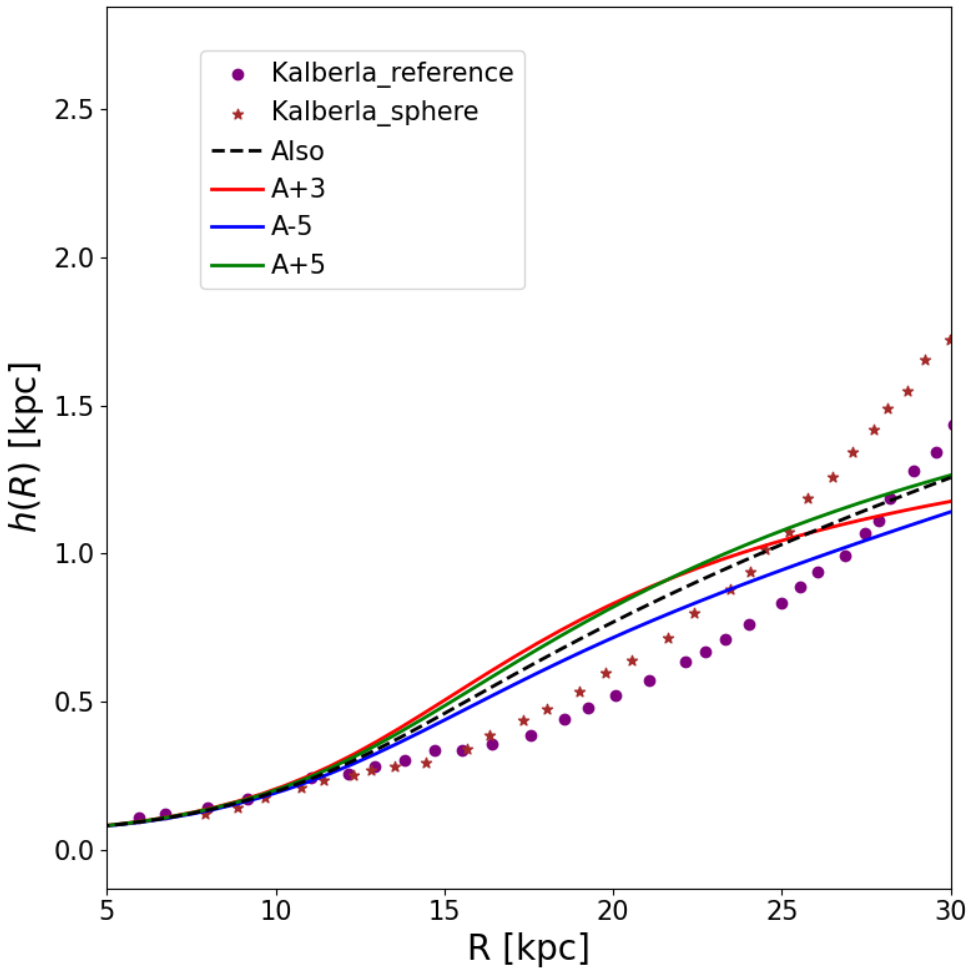

Figure 5.9: Same as Fig. 5.7, but with the profiles of our models obtained after filtering.

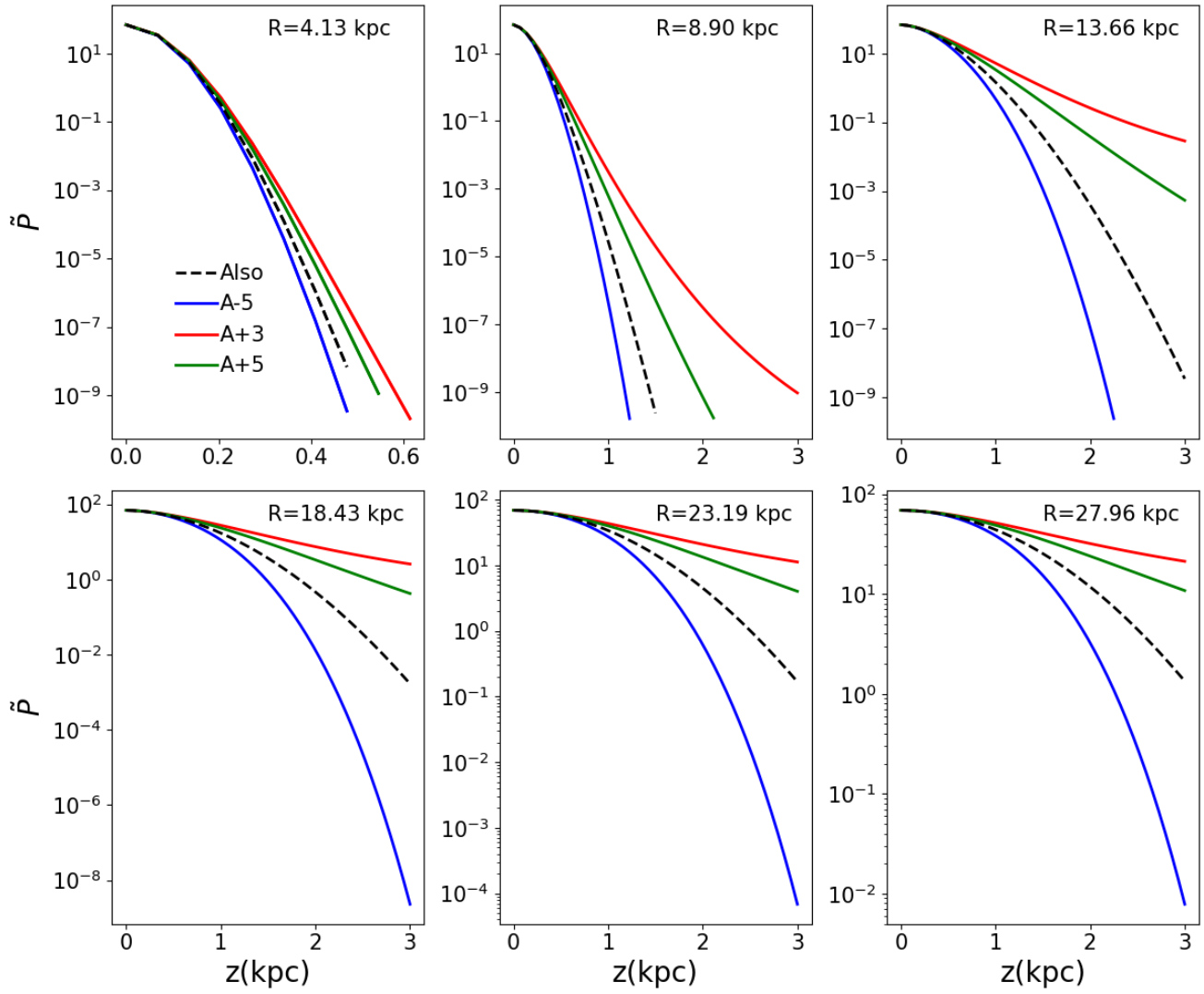

Figure 5.10: Normalized pressure $\tilde{p}$ for the Milky Way for the models in case A. The AIso model is the one represented with the black dashed line. The blue one corresponds to model A-5, while the green and red ones to the models A+3 and A+5.

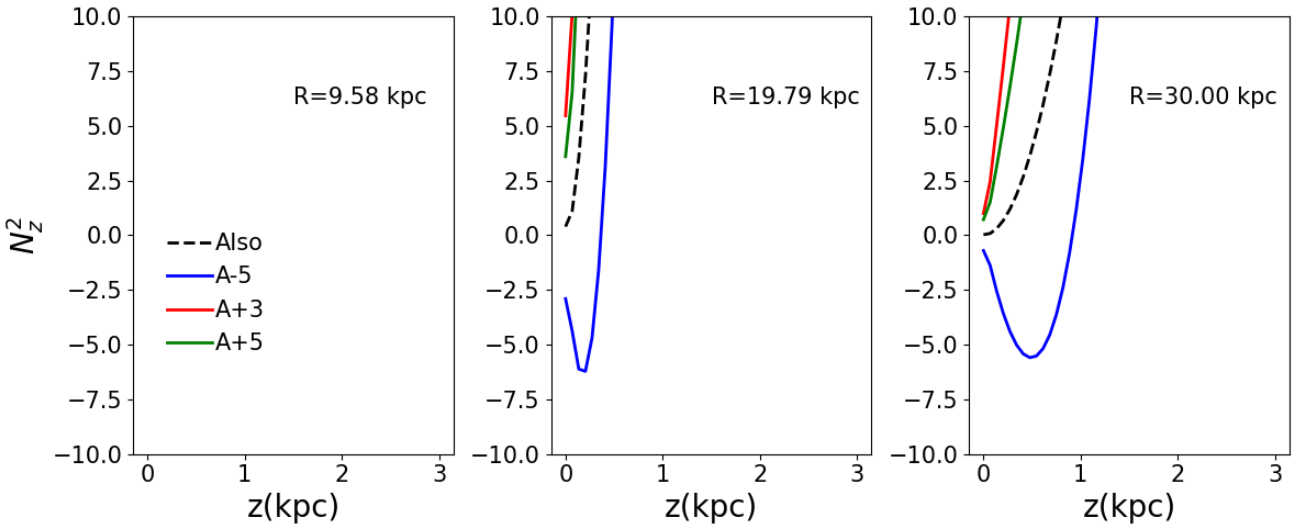

Figure 5.11: Vertical Brunt-Väisäla frequency squared N_z^2 for the Milky Way for the models in case A. The AIso model is the one represented with the black dashed line. The blue one corresponds to model A-5, while the green and red ones to the models A+3 and A+5.

5.4.2 Case B

Below, we show the results obtained for our case B where we use a radial profile for the velocity dispersion in the form of Eq. (5.2.6). In Fig. 5.12, we show the normalized vertical density profile $\tilde{\rho}$ obtained for each vertical profile of the velocity dispersion. Similar to what we saw in Section 4.2 and Section 5.4.1, we find that for models B+3 and B+5 the peak is less pronounced, but we have a shallower decrease compared to the isothermal profile, while the opposite holds true for model B-5, aka when the velocity dispersion decreases along z. While not as evident as the case shown in Fig. 4.8, we have a shifted peak for the B-5 model; we report in Fig. 5.13 a zoom on the peak. As a result, we obtain a higher scale height than the isothermal case for models B+5 and B+3, and a lower one for model B-5, as shown in Fig. 5.14 and Fig. 5.16. In Fig. 5.14 we show a comparison between our models and the observed average $h(R)$ profile obtained by Kalberla et al. (2007) when using a flat rotation curve with $v_{\rm rot} = 220$ km s^{-1} (purple dots), and when using a model with an isothermal DM spheroidal halo (brown stars). The same is shown in Fig. 5.16, but this time our profiles are shown after filtering. Similar to what we found in Section 5.4.1, the filtering causes our profiles to get closer. Moreover, this time the difference between our models is less marked than the one showed in Section 5.4.1, showing the influence of the radial profile of the velocity dispersion. As we did in Section 5.4.1, we present the fraction of discarded mass after

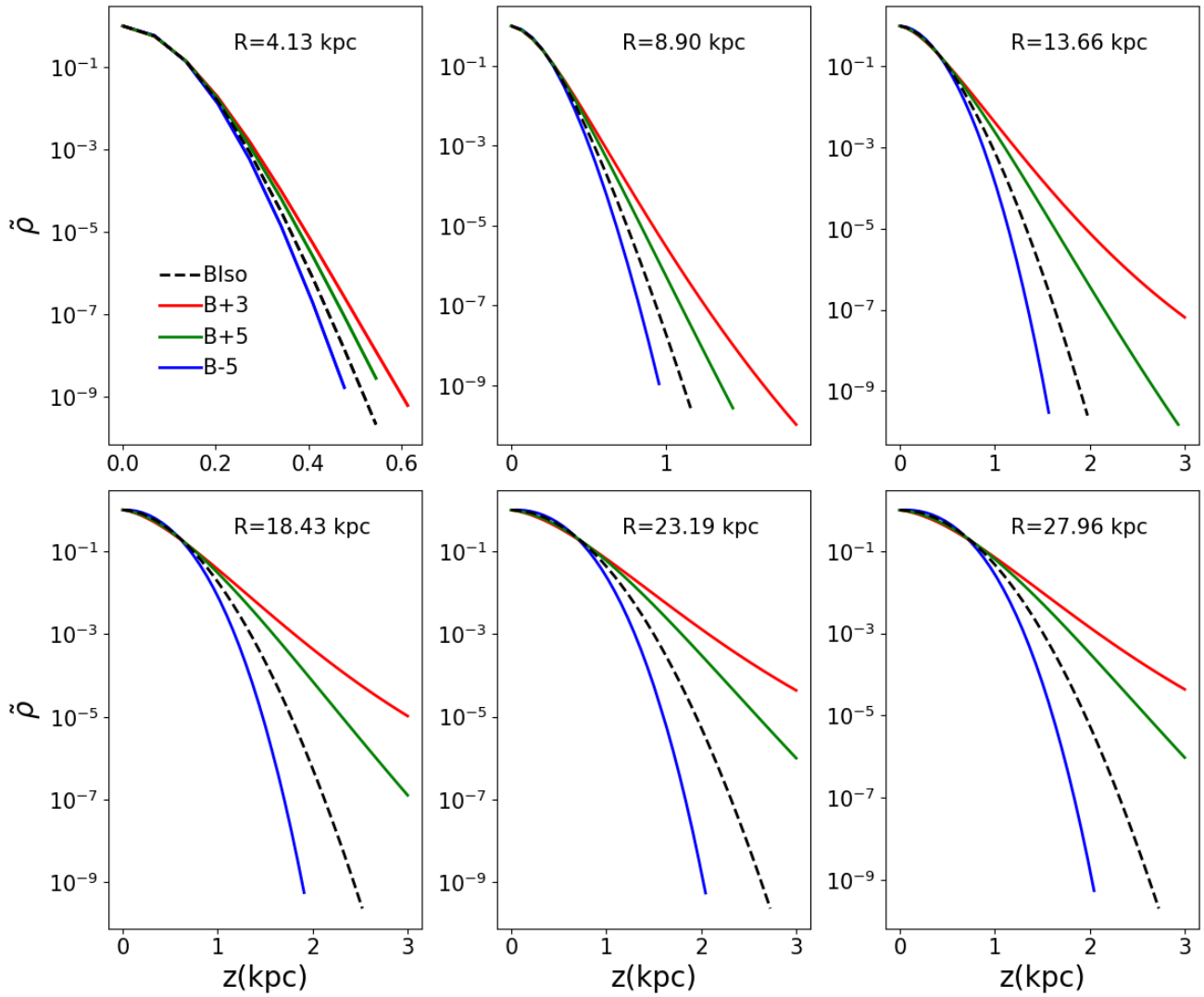

Figure 5.12: Same as Fig. 5.5, but for case B.

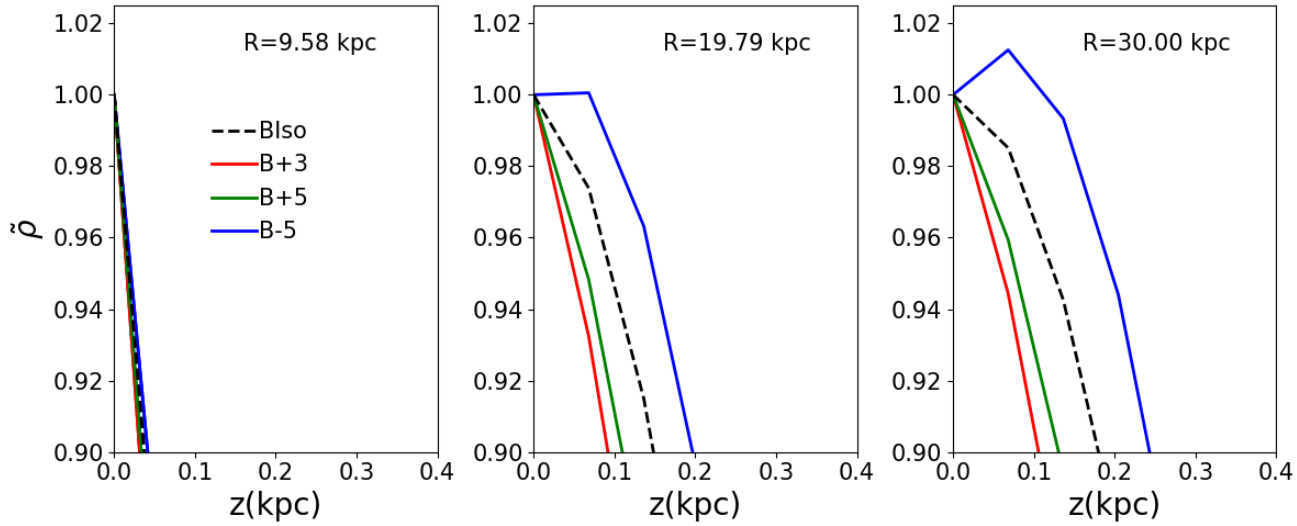

Figure 5.13: Same as Fig. 5.6, but for case B.

filtering in Fig. 5.15, but this time the different profiles for $\sigma(R, z)$ give us more similar results. This is not a surprise: the density profiles are much more similar compared to the ones shown in Section 5.4.1, but we still have the same trends, with models B+3 and B+5 having more discarded mass compared to the isothermal, while the opposite is true for model B-5. It is evident from both Fig. 5.14 and Fig. 5.16 that a velocity dispersion that monotonically decreases with R is not able to reproduce the observed $h(R)$ profile, since the MW $h(R)$ profile shows a sharp increase after $R \approx 17$ kpc. This is, however, not surprising: Marasco et al. (2017) considers the velocity dispersion to be on average $\langle\sigma(R)\rangle = 8.9$ km s^{-1}, while other articles such as Olling et al. (2000) use a constant velocity dispersion $\sigma = 9.2$ km s^{-1}, and Kalberla et al. (2007) solution is close to a single-component model with an effective constant velocity dispersion of 8.3 km s^{-1}. It is immediate that using Eq. (5.2.6) to define $\sigma(R)$ yields value of the velocity dispersion too small when going towards large radii, which results in a $h(R)$ profile that does not keep on growing. However, it is important to note that being able to reproduce the $h(R)$ profile at 5 kpc$< R <$ 17.5 kpc is an interesting result: in Kalberla et al. (2007), when using a spheroidal DM halo like us, they only manage to reproduce the average trend when comparing the model with the data, and cannot reproduce the depression in the curve, deviating from the observed $h(R)$ profile at around $R = 10$ kpc. As we pointed out in Section 5.1.2, their final solution is to renounce the classic spheroidal DM halo and use a more complex dynamical model with a DM disc and a DM ring, however here we want to show that another possibility is to act on the profile of the velocity dispersion, and

from Fig. 5.9 we can clearly that using a constant velocity dispersion is not enough if one wants to use a model that contains a spherical DM halo but a velocity dispersion that changes with the radius can improve the results, as we have just explained. Moreover, the profile that matches the data the best is model B+3, which means the contribution from the vertical profile of σ can also play a role. The pressure is shown in Fig. 5.17, where we find a similar situation as the one shown in case A (Section 5.4.1), with a gradient that is everywhere negative. The vertical Brunt-Väisäla frequency squared is shown in Fig. 5.18, where we once again see that it could lead to a violation of the Solberg-Høiland criterion for stability when $\sigma(R, z)$ decreases along z (model B-5).

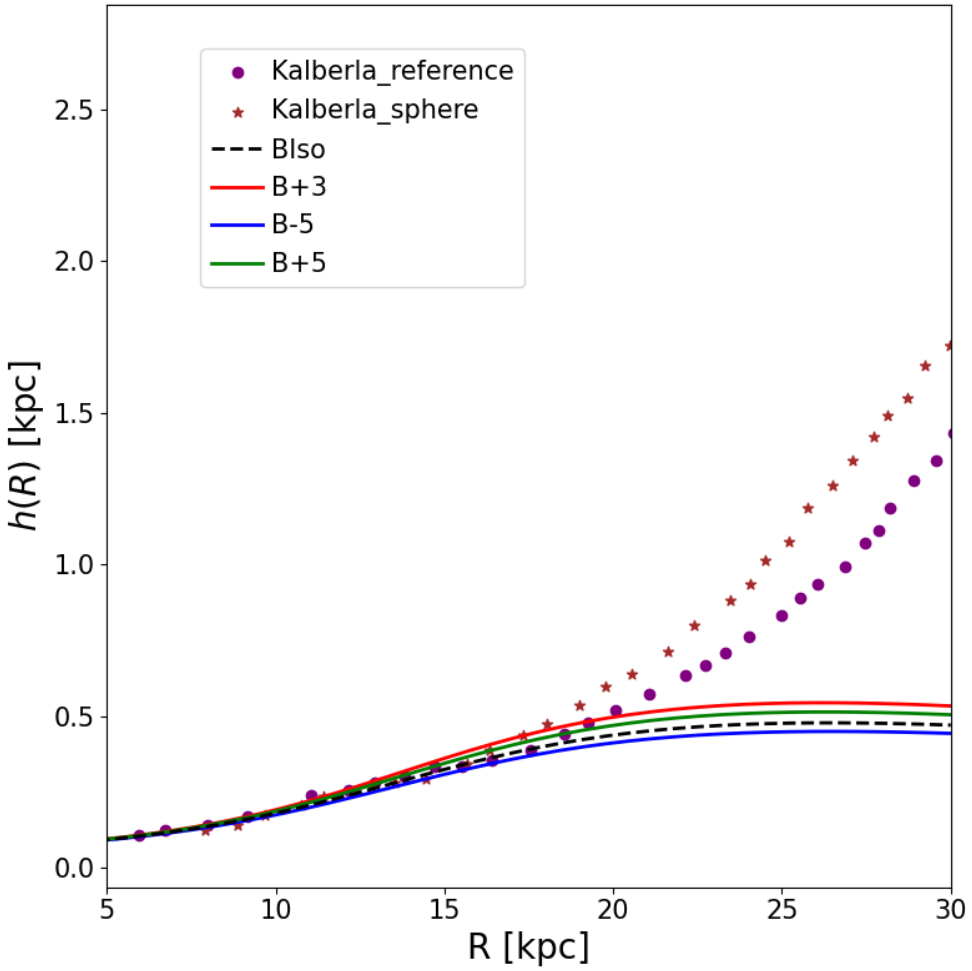

Figure 5.14: Same as Fig. 5.7, but for case B.

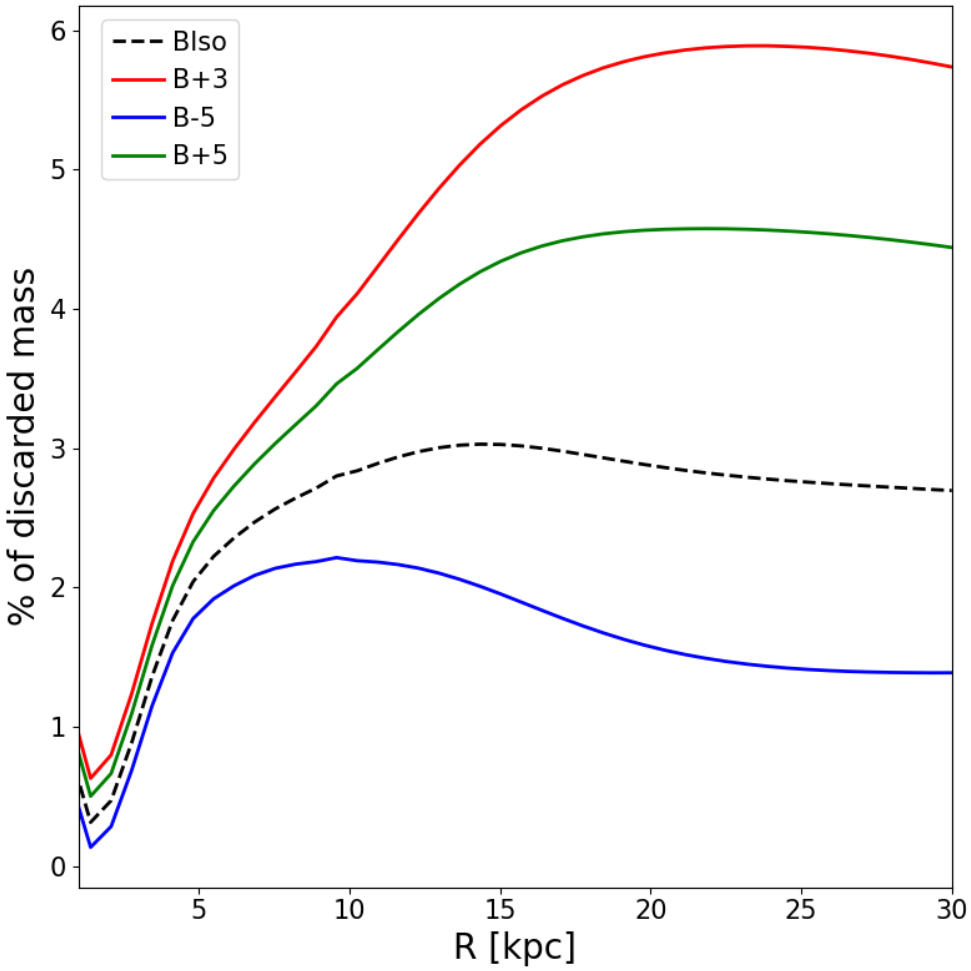

Figure 5.15: Same as Fig. 5.8, but for case B.

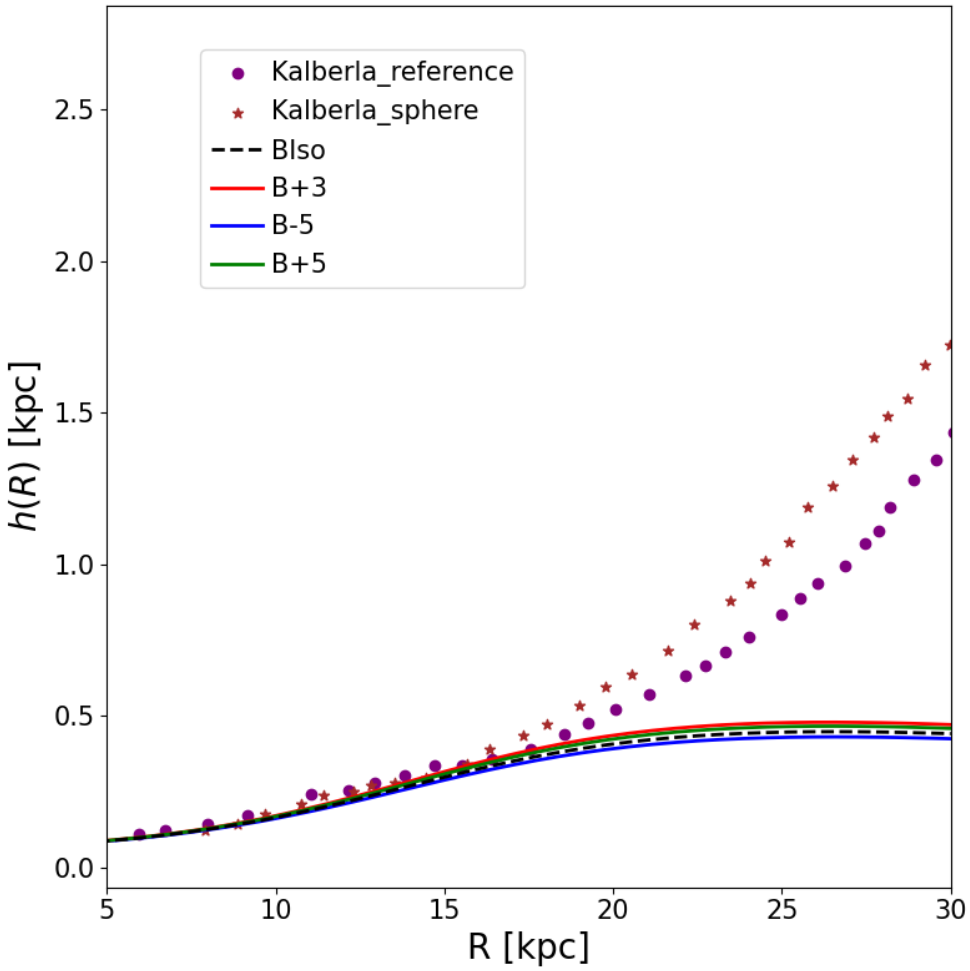

Figure 5.16: Same as Fig. 5.9, but for case B.

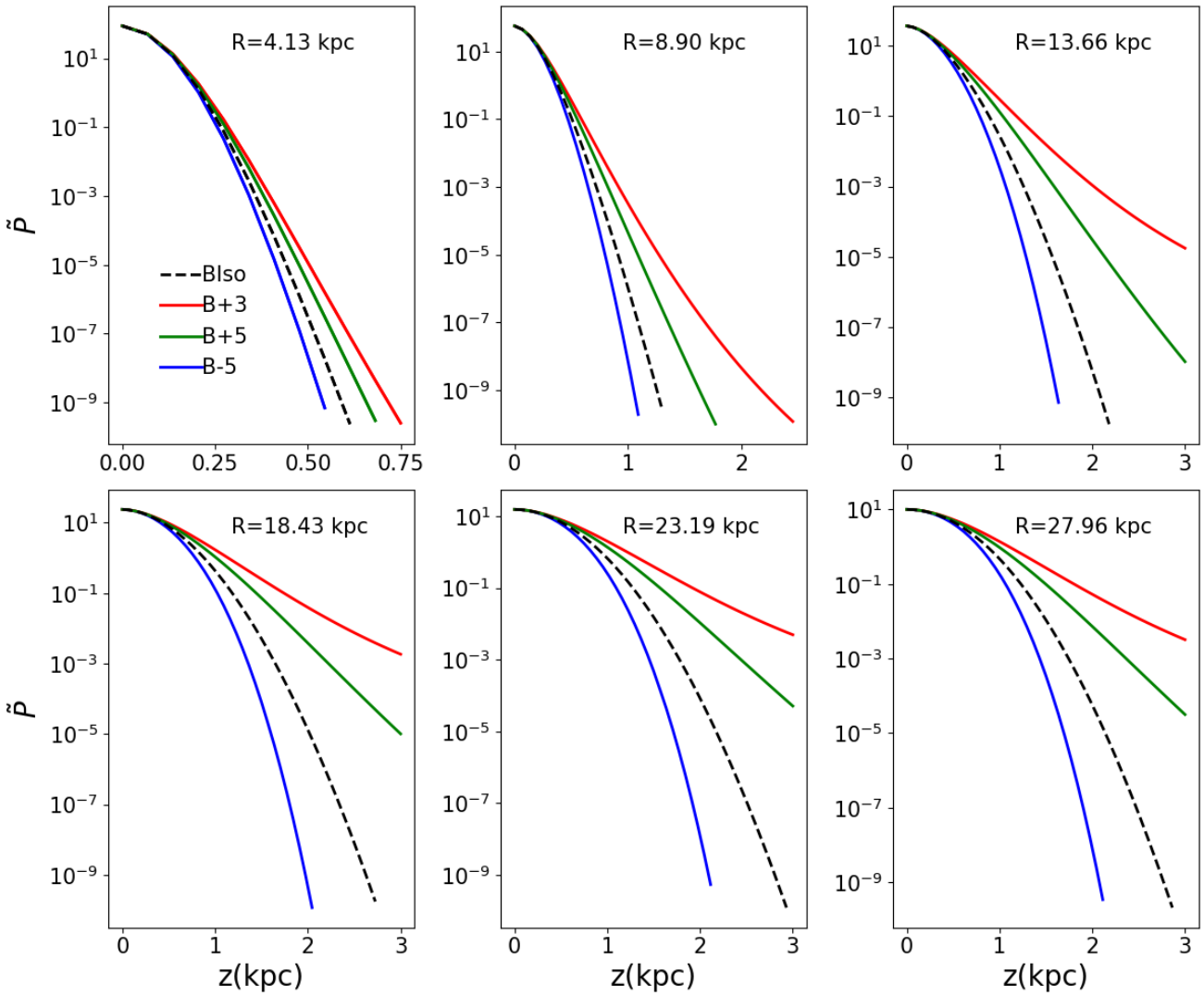

Figure 5.17: Same as Fig. 5.10, but for case B.

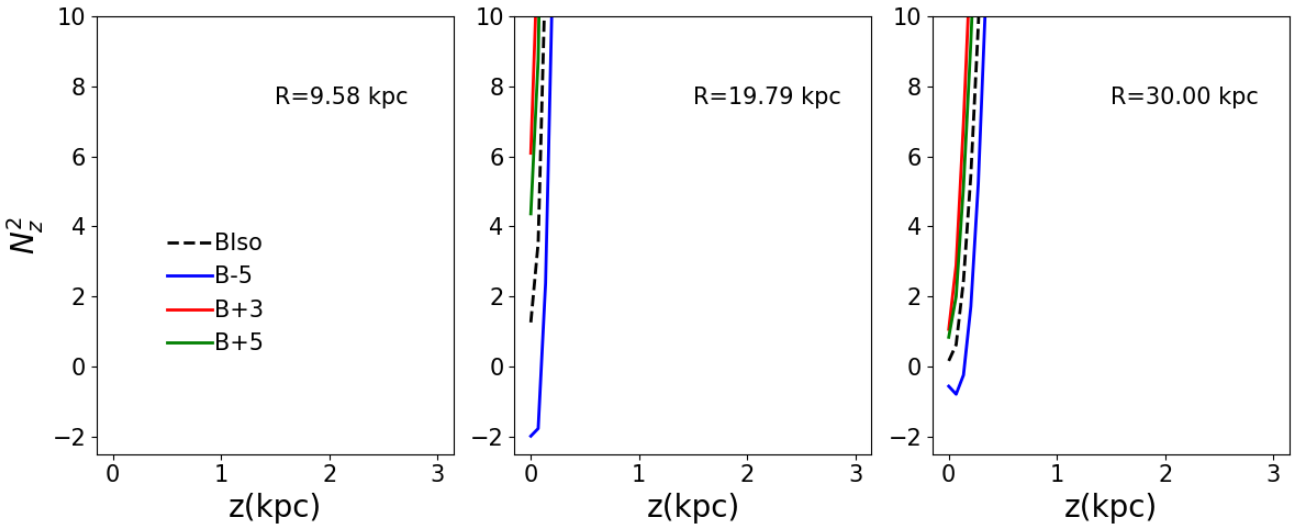

Figure 5.18: Same as Fig. 5.11, but for case B.

5.4.3 Case C

We now show the resulting disc scale-height profile when using a velocity dispersion in the form of Eq. (5.2.9), which is our case C. In Fig. 5.19 we show the normalized vertical density profile, which shows trends similar to the ones showed in case A and case B (Section 5.4.1 and Section 5.4.2), while in Fig. 5.20 we show the zoom on the density peak. Figure 5.22 shows the fraction of discarded mass, which shows bigger values for $\sigma(R, z)$ growing with z than what we found for case B (Section 5.4.2). This time, as shown in Fig. 5.21 and Fig. 5.23, we manage to reproduce the flaring up to 22 kpc, but not much beyond that. However, this is once again not surprising: at $R \gtrsim 25$ kpc we have an extended strongly flared region which deviates significantly from the average disc scale-height up to that radius. A possible explanation would be to assume the velocity dispersion increases thanks to turbulent processes, but this leads to the question of what processes could feed this additional turbulence, as this region is outside the stellar disc. In Bacchini et al. (2020) they show that the dissipation timescale actually increases for an increasing $h(R)$ profile, and they show that low-efficiency SN feedback is sufficiently energetic to be the sole driver of turbulence in local starforming galaxies, while another possible solution could be turbulence driven by gas accretion, as shown in Klessen and Hennebelle (2010). A more detailed analysis might be needed, but it is beyond the scope of this work. We show the pressure in Fig. 5.24, however we do not see anything different in the trends compared to cases A and B (Sections 5.4.1 and 5.4.2). Similarly, the vertical Brunt-Väisäla frequency squared N_z^2 can be negative when $\sigma(R, z)$ decreases with z

(model C-5), just as we saw in cases A and B (Sections 5.4.1 and 5.4.2), which means it could result in a violation of the Solberg-Høiland stability criterion.

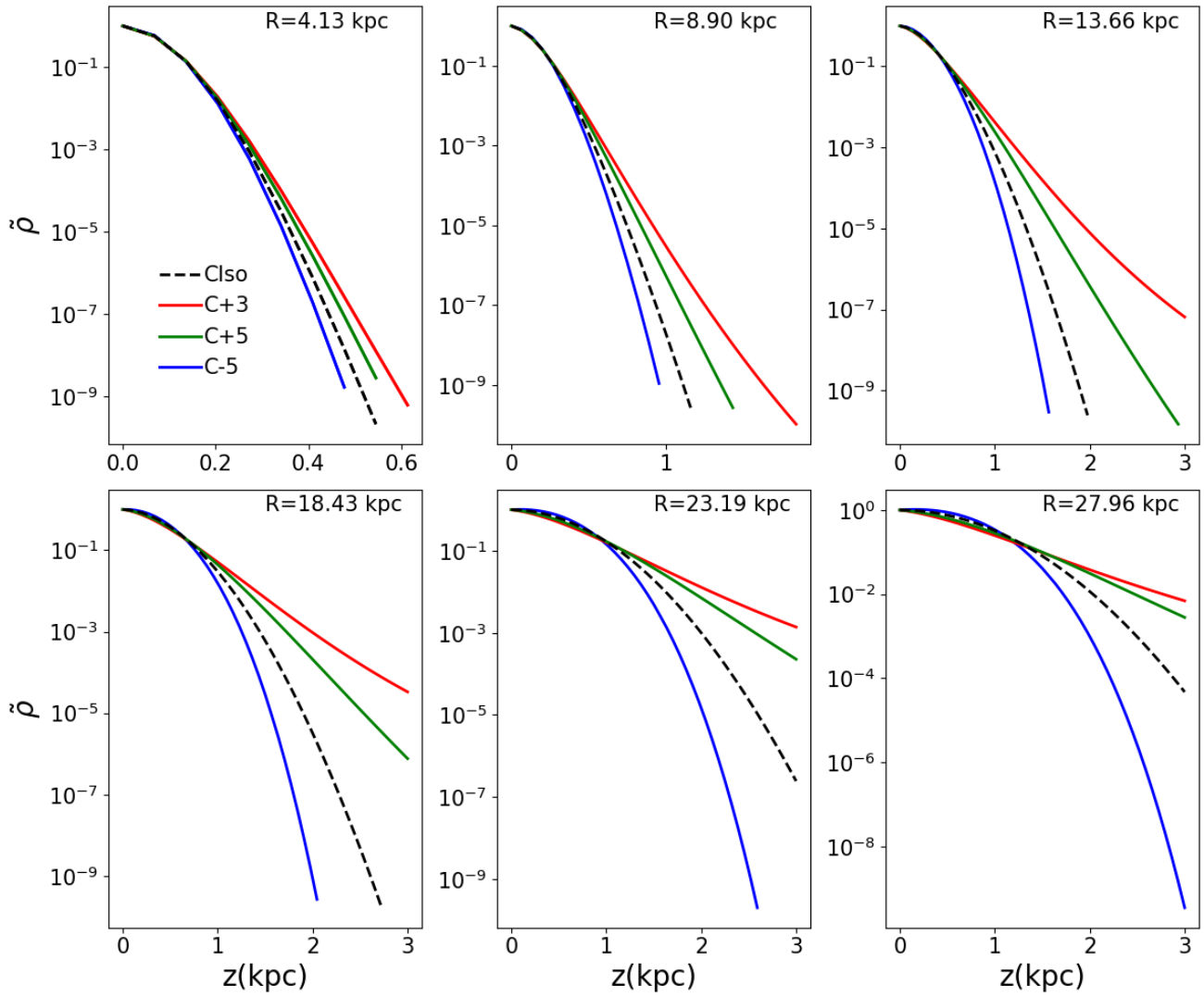

Figure 5.19: Same as Fig. 5.5, but for case C.

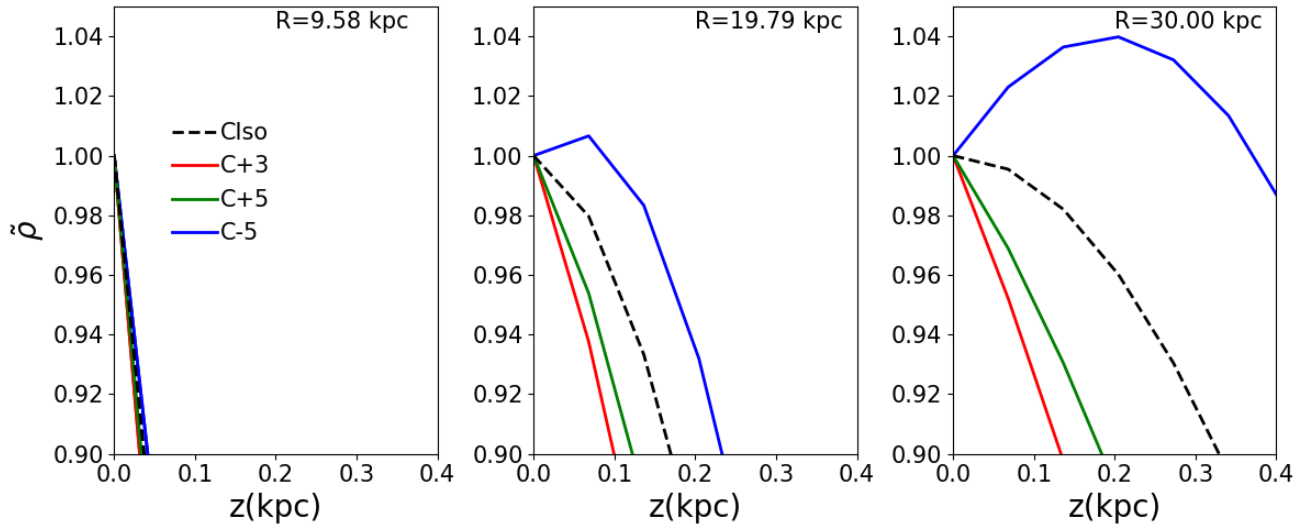

Figure 5.20: Same as Fig. 5.6, but for case C.

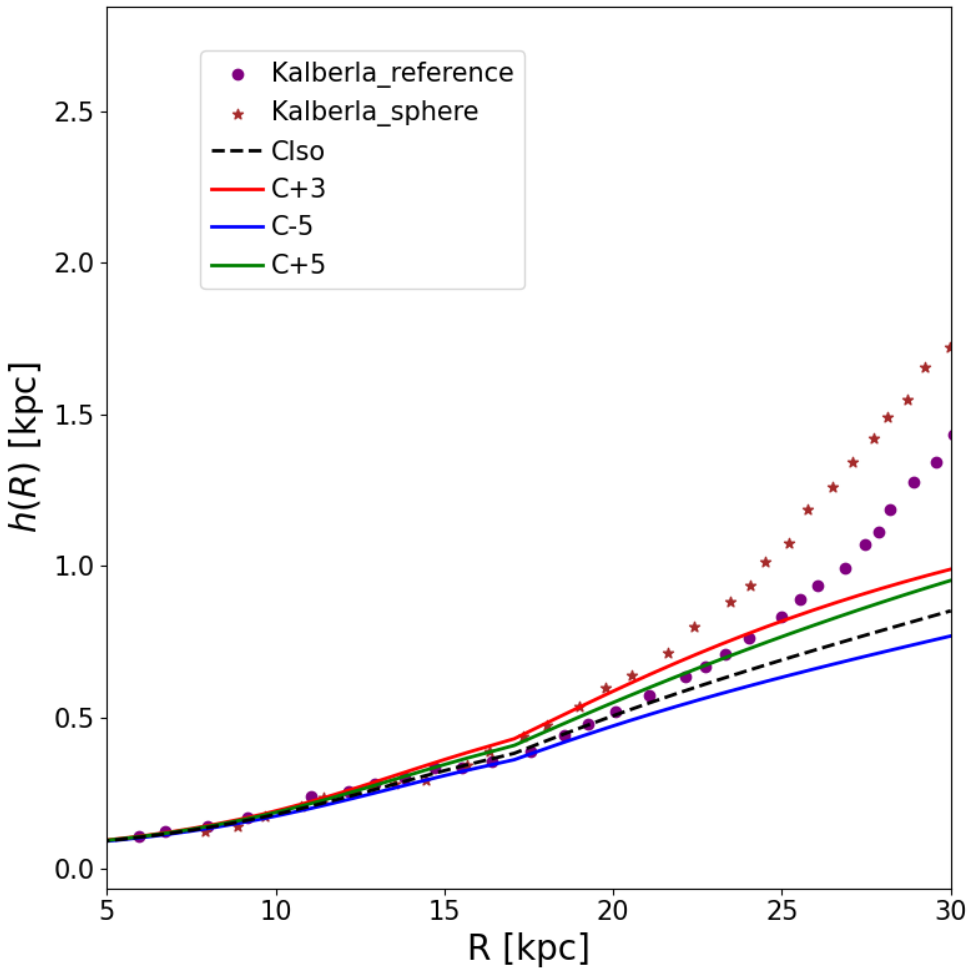

Figure 5.21: Same as Fig. 5.7, but for case C.

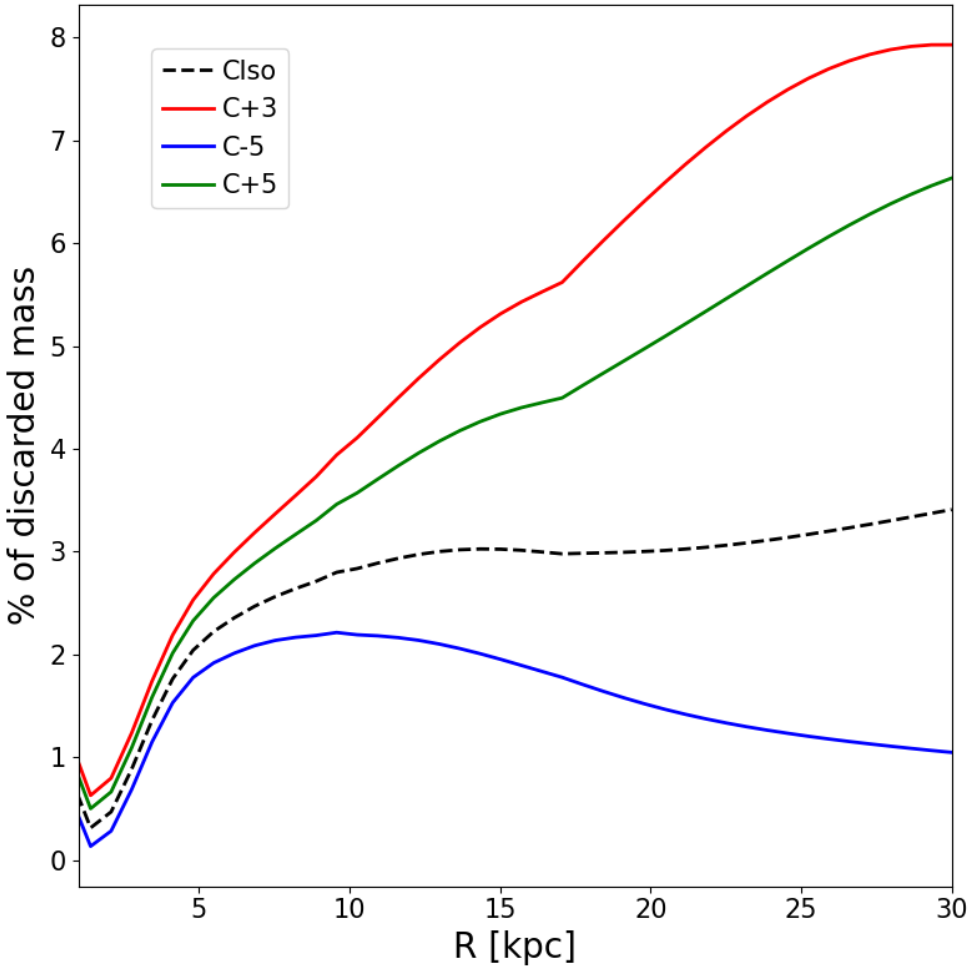

Figure 5.22: Same as Fig. 5.8, but for case C.

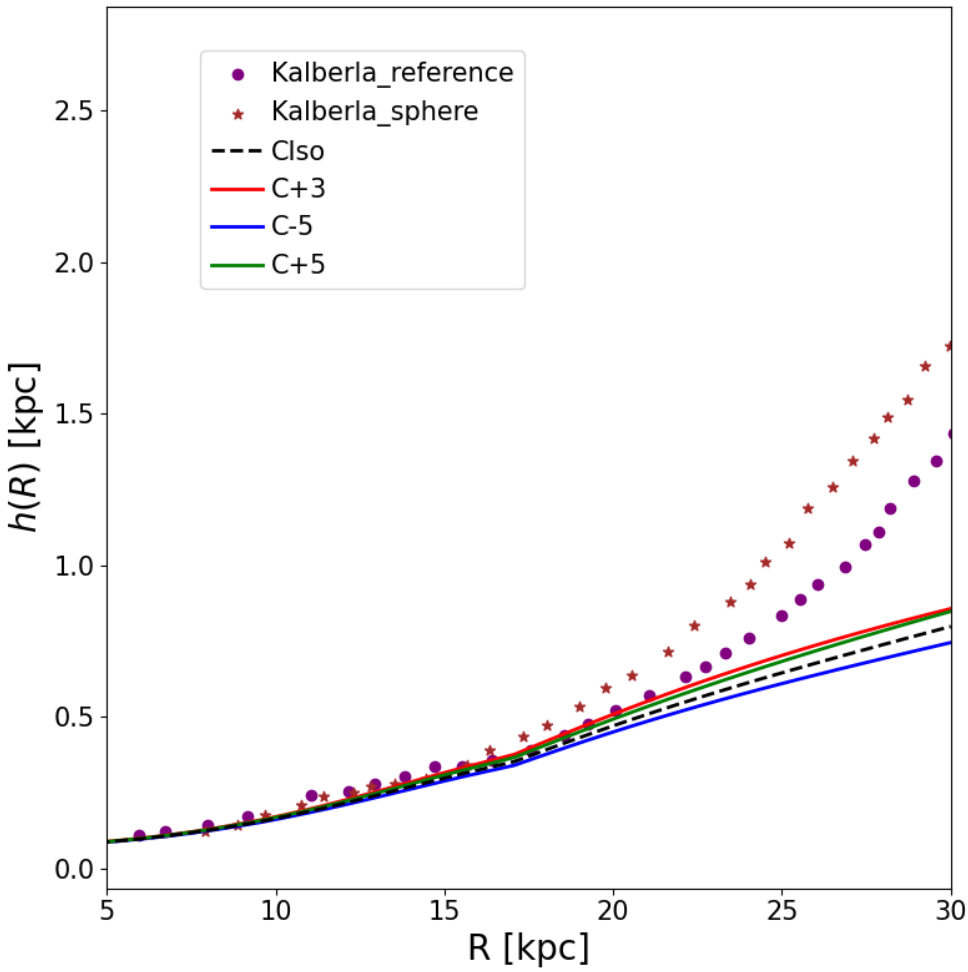

Figure 5.23: Same as Fig. 5.9, but for case C.

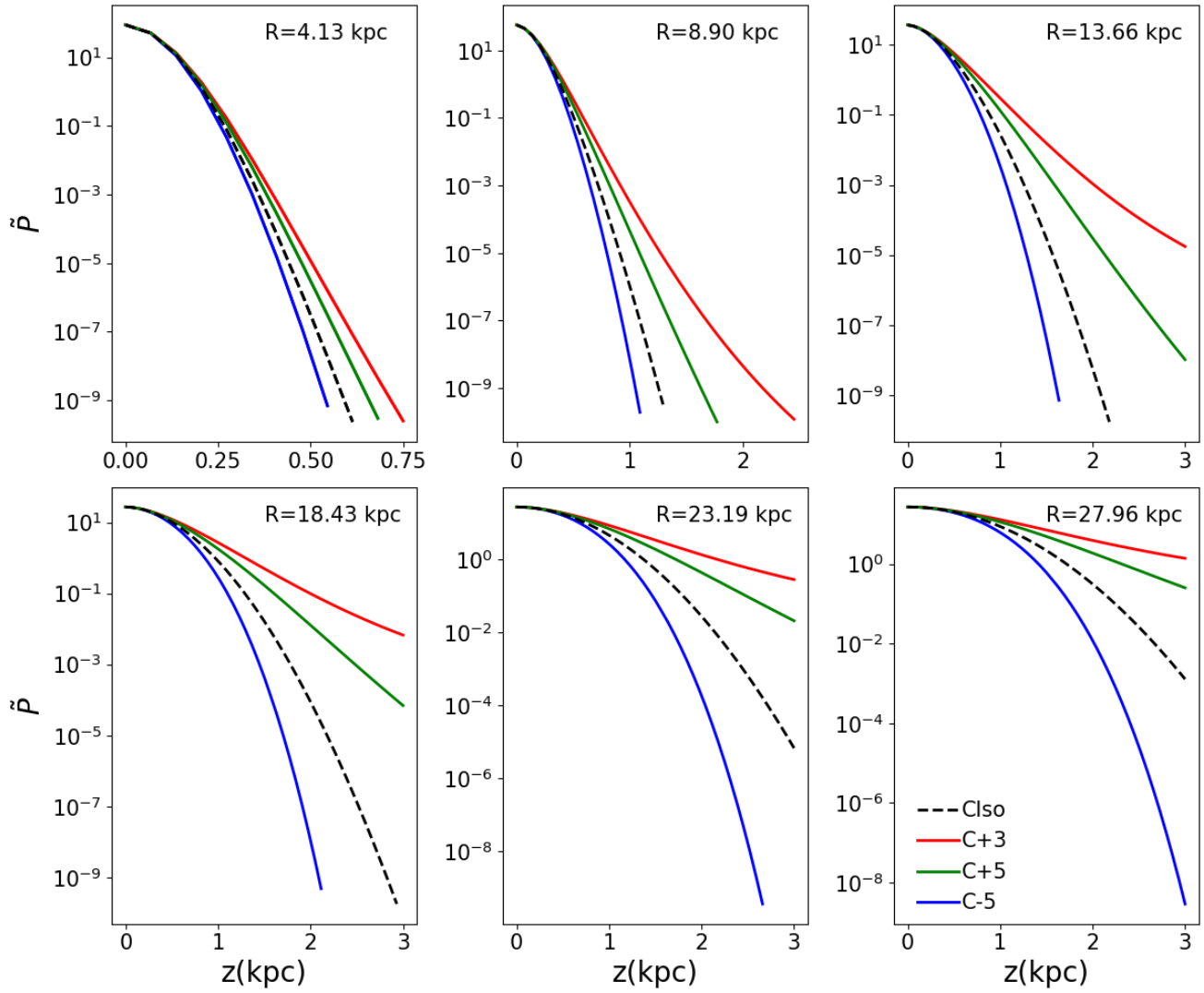

Figure 5.24: Same as Fig. 5.10, but for case C.

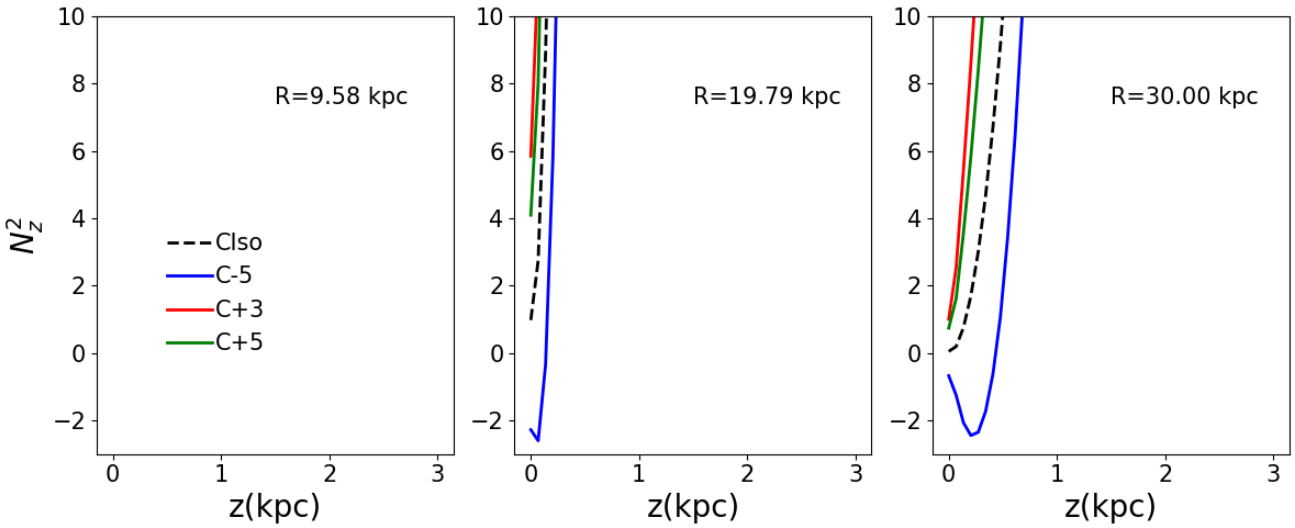

Figure 5.25: Same as Fig. 5.11, but for case C.

5.4.4 Case D

We now show our results for case D, where we have a radial profile for the velocity dispersion in the form of Eq. (5.2.11). The normalized vertical density profile and the zoom on the peak are shown in Figs. 5.26 and 5.27, and, as for models A-5, B-5, and C-5, we have the shifted peak for the model D-5; in this case we actually have a really pronounced peak, comparable to what we see in case A (Section 5.4.1). In Fig. 5.28 we show the scale height before filtering, and this time we manage to reproduce both the depression in the curve and the sharp flaring for $R \gtrsim 25$ kpc, improving the results obtained in the previous cases. Up to $R \sim 25$ kpc, model D+3 and model D+5 are the ones that manage to reproduce Kalberla et al. (2007) model with a spherical DM halo, but then they stop growing, similar to what we see in Section 5.4.1; on the other hand, the DIso and D-5 models follow the trend of Kalberla et al. (2007) model with a flat rotation curve in the beginning, but then show a sharp increase, with profiles becoming similar to the one described by brown stars. The filtering does not significantly change the results, but it is worth noting that the percentage of discarded mass, shown in Fig. 5.29, tends to grow up to $R \sim 25$ kpc, then has a sharp decrease. It is also interesting that in Sections 5.4.2 and 5.4.3 the discarded mass always grows with the radius, and while in Section 5.4.1 we see it decreases for models A+3 and A+5, it is not as sharp as the one we see in Fig. 5.29. The pressure is shown in Fig. 5.31, but we have no relevant differences to what we see in Sections 5.4.1–5.4.3, and the same can be said for the vertical Brunt-Väisäla frequency squared shown in Fig. 5.32, which once again can be negative for model

D-5, as it has a velocity dispersion that decreases along z, so this model may lead to a violation of the Solberg-Høiland stability criterion.

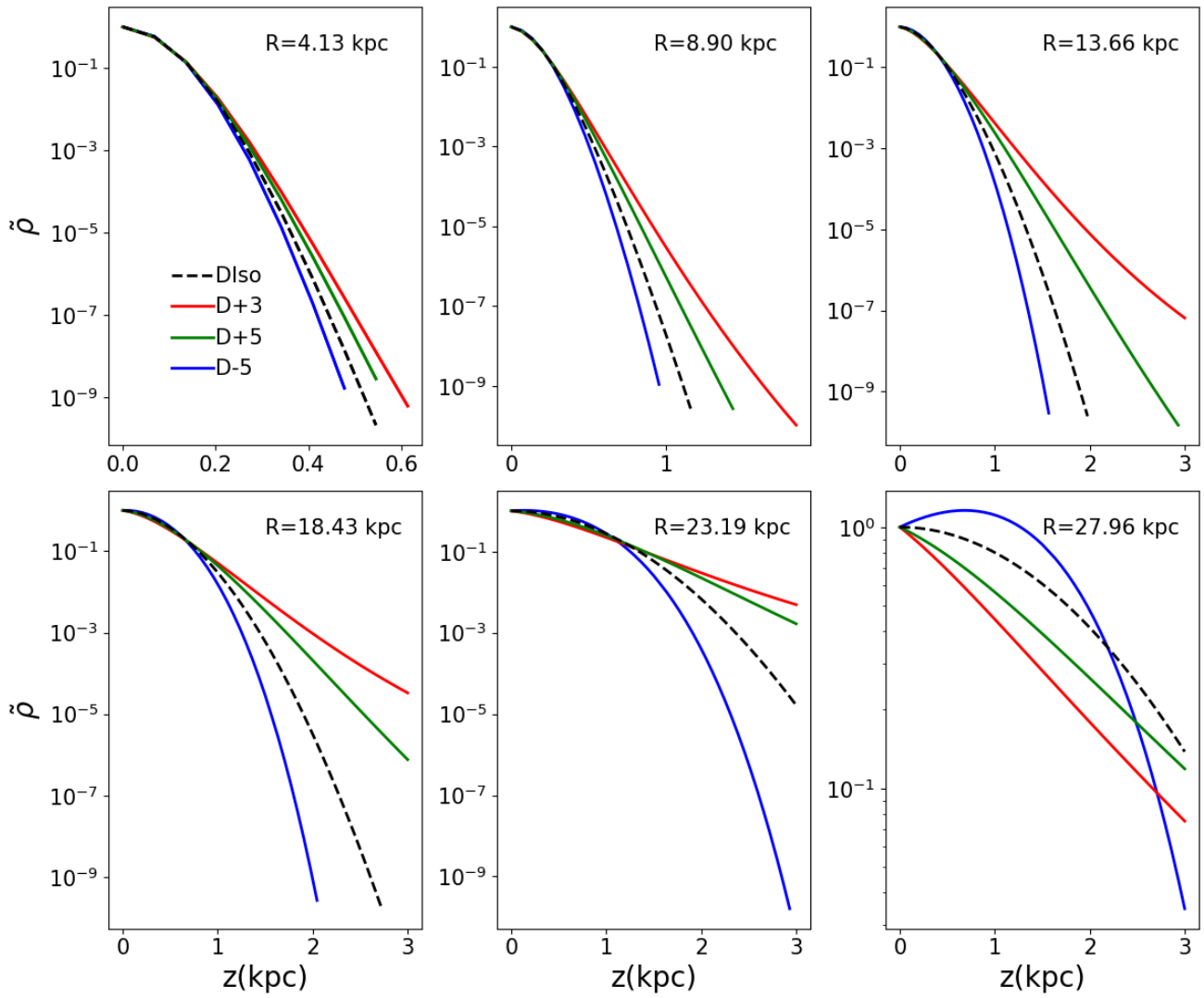

Figure 5.26: Same as Fig. 5.5, but for case D.

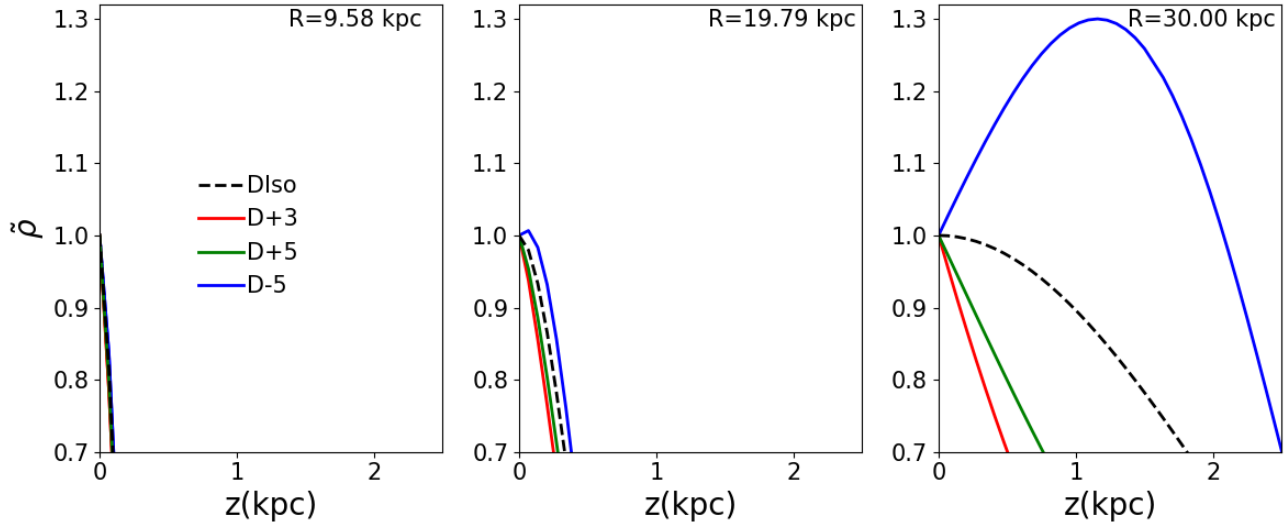

Figure 5.27: Same as Fig. 5.6, but for case D.

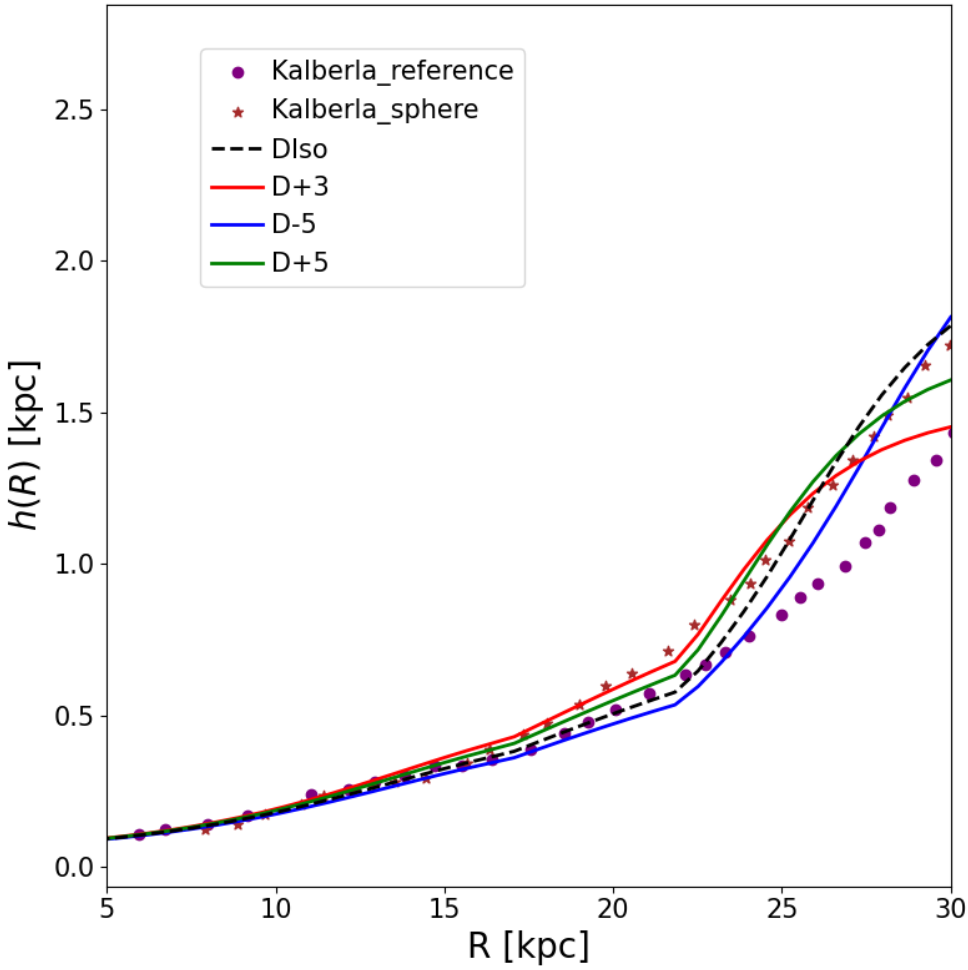

Figure 5.28: Same as Fig. 5.7, but for case D.

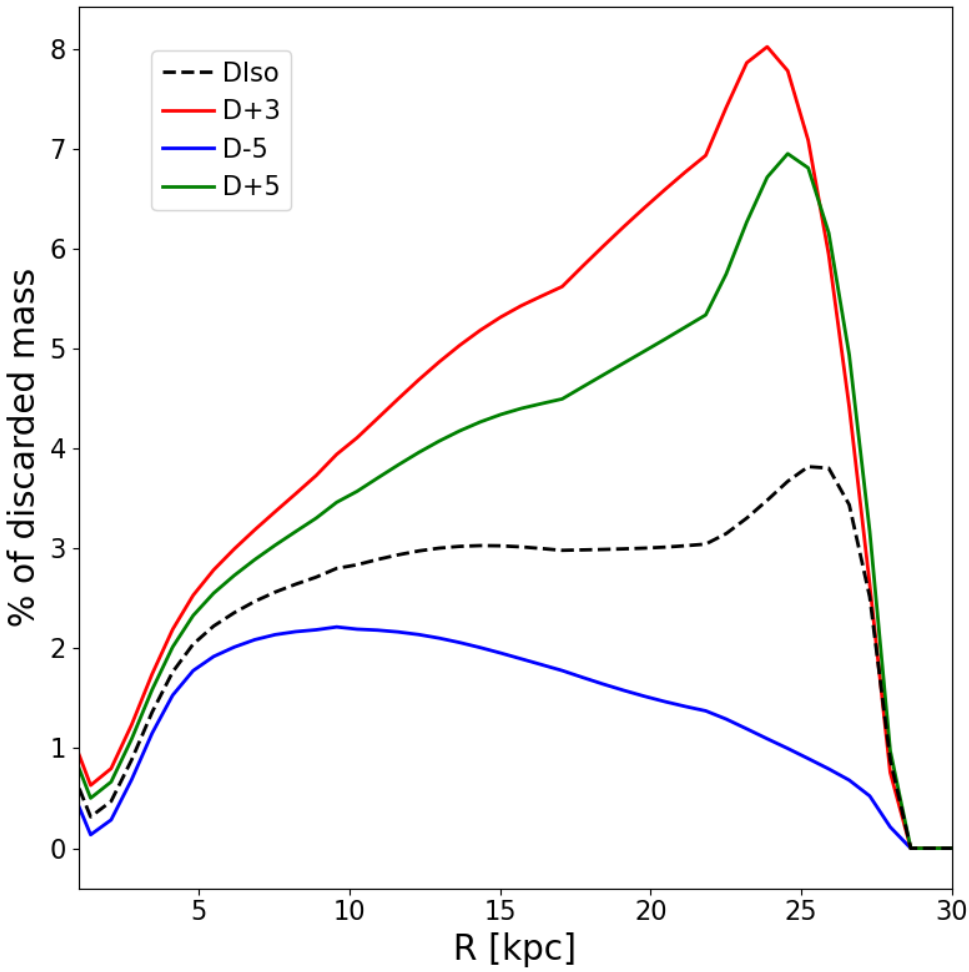

Figure 5.29: Same as Fig. 5.8, but for case D.

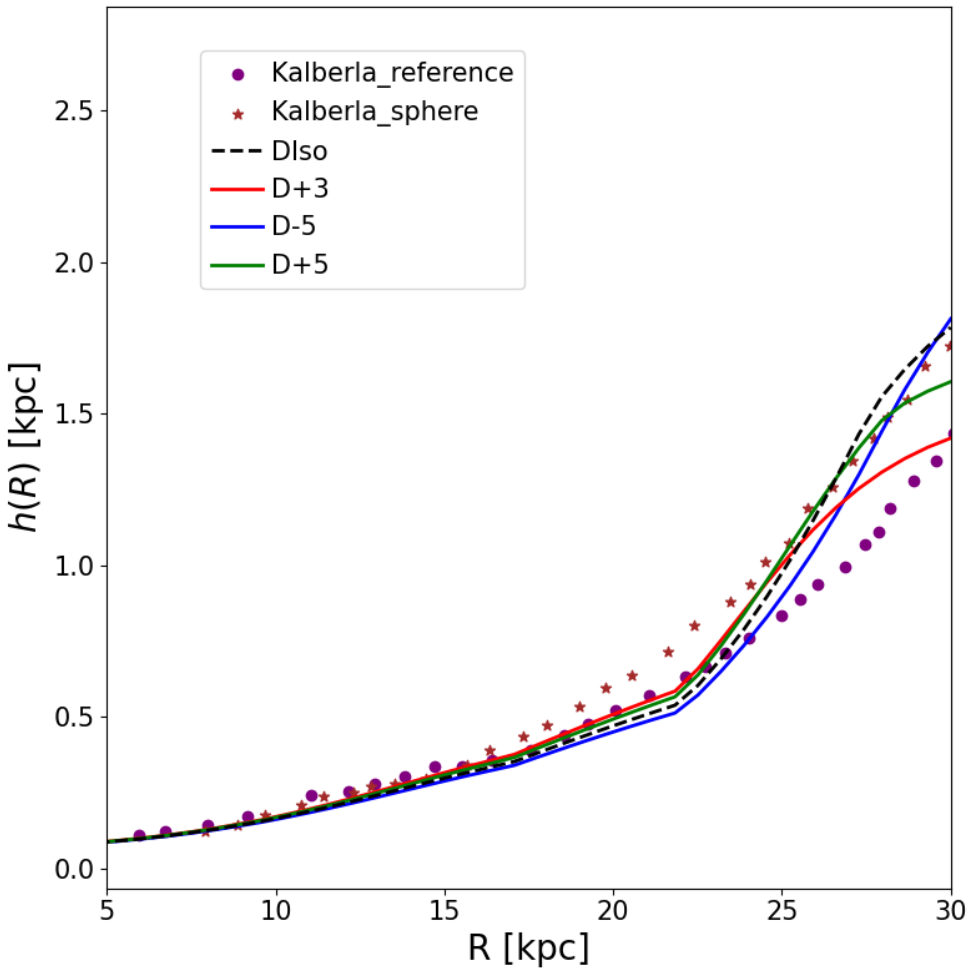

Figure 5.30: Same as Fig. 5.9, but for case D.

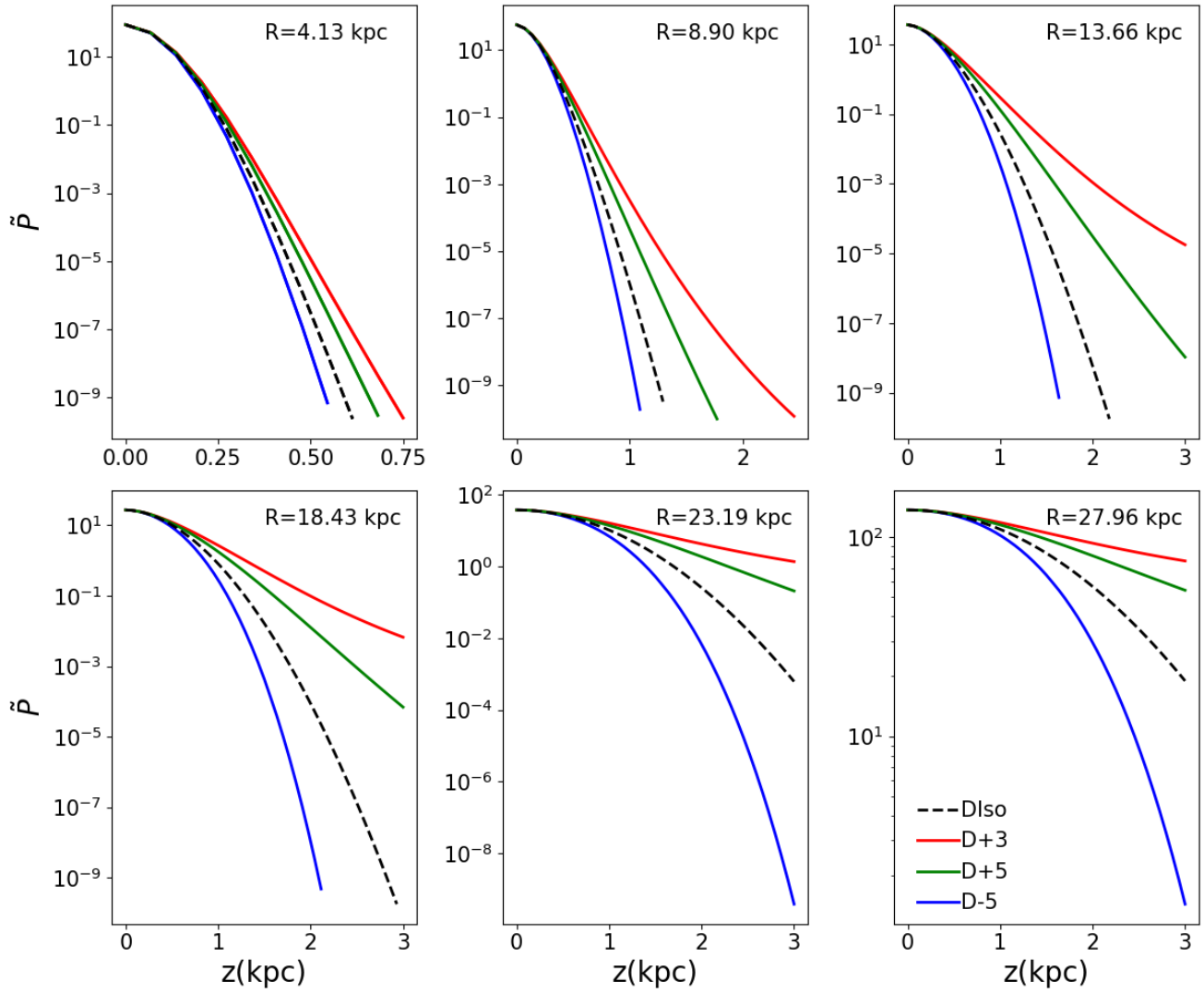

Figure 5.31: Same as Fig. 5.10, but for case D.

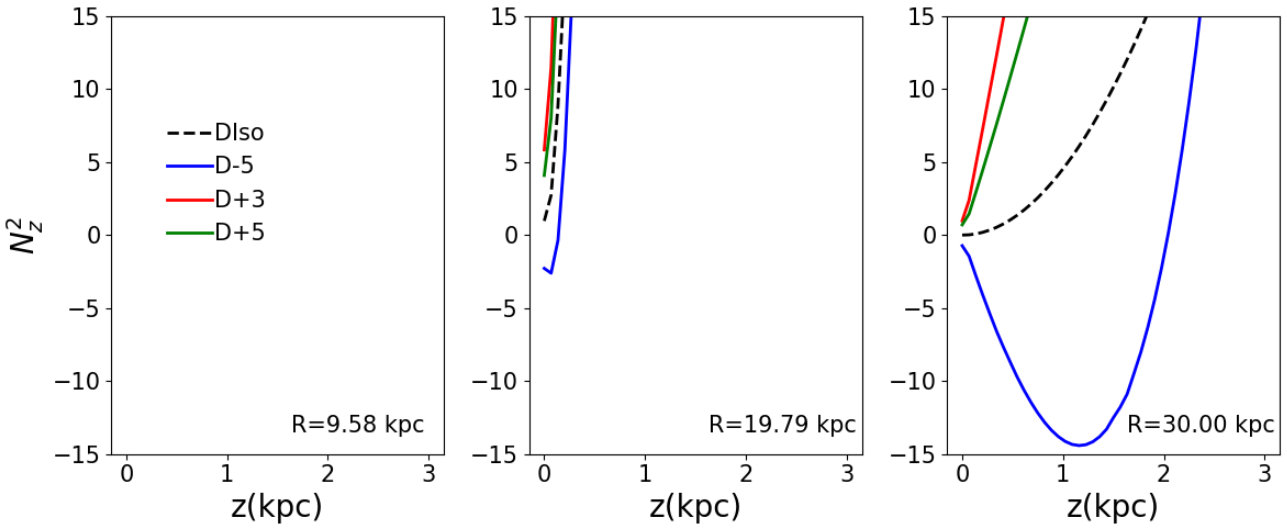

Figure 5.32: Same as Fig. 5.11, but for case D.

5.5 Discussion

In this section, we summarize the results presented in Section 5.4, discussing their implications. In the following subsections, we will use X as a placeholder for A, B, C, and D. For instance, models X-5 means models A-5, B-5, C-5, and D-5.

5.5.1 The density profile and the disc scale-height

Regardless of the radial profile of the velocity dispersion, we have that for models X-5 the peak of the normalized vertical density profile is shifted from $z = 0$ for certain values of R. This has two main implications: first, we deviate from a Gaussian profile, since we now expect to see two peaks when considering the entire z-axis, and second, the vertical gradient of the density is not always negative, which is especially important when studying the stability of the system. Interesting enough, however, the X-5 models tend to have the mass more concentrated in a neighborhood of $z = 0$ compared to the XIso ones, while the opposite usually holds true for the X+3 and X+5 ones. This means that we can expect a higher scale-height for models with a velocity dispersion that increases with z, but we see that it depends on the case, as for example the model A+3 has a lower scale-height compared to AIso for $R \gtrsim 28$ kpc. A possible explanation for these discrepancies might be that the choice of the radial profile of the velocity dispersion matters more than the vertical profile: depending on $\sigma(R)$, we can expect different trends for different vertical profiles of

the velocity dispersion. A thorough investigation to properly explain this phenomenon is needed, but it is beyond the scope of this work.

5.5.2 The mass discarded: the comparison with Kalberla et al. (2007)

In general, what we witness is that the XIso models tend to discard around a bit less than 3% of the mass, which is a bit more than the value we expect for a Gaussian profile, but less than what Kalberla et al. (2007) discards: this is what we were expecting, as the XIso models should follow a distribution similar to a Gaussian profile. For the X-5 models, we instead discard less than 2%, which is not surprising, considering we expect the mass to be more concentrated in a neighborhood of $z = 0$ compared to the XIso models, so of course there is less mass in the tails that can be removed. On the other hand, for the X+3 and X+5 models, the mass discarded is usually much more than 2%, reaching values up to 8% in certain cases. This means, as we were expecting, that a velocity dispersion that increases with z tends to move the mass outwards. This has an interesting implication: the "excess" mass Kalberla et al. (2007) discards might not only be due to extraplanar gas, but it may actually be part of the disc mass, as assuming a velocity dispersion that increases with z gives us a gas distribution that has more mass present is the tails, so using Kalberla et al. (2007) filtering process may remove relevant data.

5.5.3 The $h(R)$ profile: our models vs the ones by Kalberla et al. (2007)

In case A, we obtain $h(R)$ profiles similar to what Kalberla et al. (2007) finds for the theoretical $h(R)$ profile of a model with a spheroidal DM halo, which is not able to reproduce the observed profile. The interesting part is that (just like Kalberla et al. (2007)) we tend to overestimate the region between $R \approx 12$ kpc and $R \approx 25 - 27$ kpc (depending on the observed $h(R)$ profile we are looking at). In case B, on the other hand, we manage to reproduce quite well this depression in the curve, up to $R \approx 17 - 19$ kpc, and all we did was simply assuming a radial profile for σ, which we determined using actual data by Marasco et al. (2017), while in Kalberla et al. (2007), they only manage to reproduce this depression by adding a DM ring to their models. On the other hand, while we have no trouble reproducing well this shallow increase of the $h(R)$ profile, we need a very complex radial profile to explain the sharp increase of $h(R)$ at radii larger than $R \approx 22$ kpc. In case D we manage to reproduce the $h(R)$ profile pretty well, but it is important to notice that the profile we use for $\sigma(R)$ is only partially based on observational constraints. In Kalberla et al. (2007), they find that using a DM disc instead of the more classical spherical

halo can reproduce well the $h(R)$ profile for $R \gtrsim 25$ kpc, but without the DM ring they cannot reproduce the depression in the curve, so maybe a model with a DM disc with a non-constant velocity dispersion may be the best solution. We also want to point out that in both case B and C the best results are obtained with models B+3 and C+3, so the best choice for the velocity dispersion might be one that increases with z.

5.5.4 The vertical Brunt-Väisäla frequency

As we explain in Section 2.5, while a full stability analysis is beyond the scope of this work, we can still make some suppositions. For all cases, we find that models X-5 can have a negative vertical Brunt-Väisäla frequency squared, which implies the vertical gradient of the specific entropy s_0 can be negative. This can result in a violation of one or both of the conditions presented in the Solberg-Høiland criterion. Normally, we have that Eq. (2.5.8) holds true, so to respect the first condition, described in Eq. (2.5.6), if the vertical gradient of the normalized specific entropy is negative we need to have a more relevant contribution from the radial gradients of s_0 and the pressure. Similarly, for the second condition (Eq. (2.5.7)), if $\frac{\partial s_0}{\partial z} < 0$, in order to respect the inequality we need the radial gradient of the specific entropy to be "stronger" than the vertical one.

Chapter 6

Summary and conclusions

In this chapter, we summarize the content of this thesis, and draw our final conclusions.

We first presented the equations needed to describe galactic gaseous discs assuming a generic non-isothermal vertical distribution. We found that, in general, our fluid has a baroclinic distribution, except for some specific profiles of the density and the velocity dispersion (Section 2.4). Moreover, we showed that the density depends on the gravitational potential, which however depends on the density, so we concluded that to determine the structure of our models we needed an iterative process (Section 2.3). Furthermore, we briefly discussed rotational and convective instability, since we saw that, with $\sigma = \sigma(R, z)$, for a velocity dispersion that decreases along z we can have a negative vertical gradient for the density, and it is not guaranteed that the Solberg-Høiland criterion for stability is satisfied (Section 2.5).

We then presented the numerical method we use to create our models; we expanded the Python module `galpynamics`, developing a code that can build gaseous discs with a generic velocity dispersion $\sigma = \sigma(R, z)$, taking into account the self-gravity of the disc. With our method, we can thus find the vertical density profile and the scale-height of our models, as well as the pressure and the vertical Brunt-Väisäla frequency squared, which we use as a check to see if the vertical gradient of the normalized specific entropy s_0 can be negative.

Chapter 4 was dedicated to the building of illustrative models, whose purpose was to illustrate the effects on the vertical structure caused by a velocity dispersion that depends on z. We built two mock galaxies, which had the same stellar disc and surface density of the gaseous disc, but different DM haloes (described by a NFW and a pseudo-isothermal profile respectively). Moreover, the second model was without a bulge. For both galaxies, we showed two different cases, each one

associated to a different radial profile of σ (Tables 4.1 and 4.3), and five models, each corresponding to a vertical profile of the velocity dispersion (Tables 4.2 and 4.4): two have an increasing $\sigma(z)$, two have a decreasing $\sigma(z)$, and one, which is the isothermal model, has a σ that does not depend on z. We summarize below the results:

- For every model with a decreasing $\sigma(z)$, the peak of the vertical density profile can shift from $z = 0$. Moreover, it generally shows a sharper decrease than isothermal models, while models with an increasing $\sigma(z)$ show a density with higher tails.
- For the disc scale-height, depending on the radial profile of σ, we can have two different cases:
    1. For $\sigma(R)$ =const: we do not have a clear trend with $\sigma(z)$, models with an increasing $\sigma(z)$ start with a higher scale-height compared to isothermal models, but then it grows lower, while for models with a decreasing $\sigma(z)$ it starts lower, but sometimes may grow higher, other times it stays lower.
    2. For $\sigma(R)$ not constant, there is a trend associated with $\sigma(z)$: models with an increasing $\sigma(z)$ have a higher disc scale-height than isothermal models, while models with a decreasing $\sigma(z)$ have a lower one.
- The Brunt-Väisäla frequency squared can have negative values for models with a decreasing $\sigma(z)$, which may result in a violation of the Solberg-Høiland criterion.
- The presence of a bulge causes the mass to be more concentrated at small radii, which translates in a scale height that starts smaller but grows bigger at large radii.

Finally, we apply our method to model the vertical distribution of the HI disc of our galaxy, the Milky Way. The gas distribution and kinematics were derived by Marasco et al. (2017), while for the dynamical model we mostly follow the approach used in Bacchini et al. (2024). We then compared the $h(R)$ profile obtained for our models with two of the observed ones presented in Kalberla et al. (2007). Aside from the $h(R)$ profile, what we also want to compare is the mass discarded using the filtering process described in Kalberla et al. (2007). In Kalberla et al. (2007), they filter their data to exclude any extraplanar gas present in the tails of the distribution. Basically, they state that, assuming the gas follows a distribution similar to a Gaussian profile, if no extraplanar gas is present, one should eliminate around 2% of the data when filtering the tails. However, they exclude double that amount, concluding that this excess mass is due to extraplanar gas, which is

thus effectively removed with their method. What we want to test, however, is if this cut may actually be removing part of the gas disc, as assuming a $\sigma = \sigma(R, z)$ may result in profiles that contain much more gas in the tails compared to a Gaussian distribution. We studied four different cases for four different radial profiles of the velocity dispersion (Table 5.3), and for each case we built four models, each one describing a vertical profile of the velocity dispersion (Table 5.4): two with an increasing $\sigma(z)$, one with a decreasing $\sigma(z)$, and one with a σ independent of z, which is the isothermal model. The discussion of the results we obtained is presented in Section 5.5, but here we report the main points.

- Similar to what we found for the illustrative models, the model with a decreasing $\sigma(z)$ showed a shifted peak for the density, and can result in a negative Brunt-Väisäla frequency squared at large radii, which may lead to a violation of the Solberg-Høiland stability criterion.

- Models with an increasing $\sigma(z)$ tend to discard much more mass compared to what one would discard from a Gaussian distribution: this means that a velocity dispersion that increases along z tends to drive more mass outwards, resulting in a profile that deviates from a Gaussian distribution. This means that extraplanar gas might not be only reason we have the "excess" mass present in the tails, so eliminating it might remove part of the disc mass.

- Comparing the $h(R)$ profile of our models to the ones observed by Kalberla et al. (2007), we found that we manage to reproduce the depression in the curve up to $R \approx 17 - 19$ kpc pretty well using the radial profile for σ obtained from the data, while Kalberla et al. (2007) only manages to do this by using a model that includes a DM ring. However, we can only reproduce the sharp increase from $R \approx 22$ kpc using a very complex $\sigma(R)$, something that Kalberla et al. (2007) achieves by using a DM disc instead of the classic spheroidal halo. Moreover, in general our best results are obtained with models that have an increasing $\sigma(z)$.

To conclude, our work showed that the dependence on z of the velocity dispersion can have an impact on both the density and the disc scale-height. In particular, a σ with a decreasing vertical profile can result in a shifted peak from $z = 0$ for the density, which can then lead to a negative Brunt-Väisäla frequency squared, which implies a negative vertical gradient for the normalized specific entropy, and could lead to a violation of the Solberg-Høiland criterion for stability. Moreover, using a velocity dispersion that increases with z drives the mass outwards, deviating from a Gaussian profile. This means that filtering the "excess" mass in the tails, like it is done in Kalberla et al. (2007), may remove part of the actual disc mass. Finally, comparing our

$h(R)$ profile of the HI disc of the Milky Way to the ones obtained by Kalberla et al. (2007), we conclude that assuming a velocity dispersion that is not constant can help in modelling the $h(R)$ profile, without the need to use a much more complex dynamical model, which was the solution adopted by Kalberla et al. (2007), where they found that the best results were obtained with a DM disc combined with a DM ring. A further development of our work could consist in studying more accurately the stability of the system by properly checking if the Solberg-Høiland criterion is respected; moreover, it would be interesting to expand the work on the Milky Way by verifying if a combination of our solution and the one found by Kalberla et al. (2007) can work, combining a model that uses a DM disc with a non-constant velocity dispersion.

Bibliography

[1] K. Aditya. "Stability of galaxies across morphological sequence". In: 522.2 (June 2023), pp. 2543–2552. DOI: 10.1093/mnras/stad1143. arXiv: 2304.07734 [astro-ph.GA].

[2] A. Afruni et al. "The long life of ultra diffuse galaxies inside low-density dark matter haloes: the case of AGC 114905". In: 538.1 (Mar. 2025), pp. 60–75. DOI: 10.1093/mnras/staf281. arXiv: 2502.08717 [astro-ph.GA].

[3] C. Bacchini et al. "A 3D view on the local gravitational instability of cold gas discs in star-forming galaxies at $0 \lesssim z \lesssim 5$". In: *A&A* 687 (2024), A115. DOI: 10.1051/0004-6361/202449925.

[4] C. Bacchini et al. "Evidence for supernova feedback sustaining gas turbulence in nearby star-forming galaxies". In: 641, A70 (Sept. 2020), A70. DOI: 10.1051/0004-6361/202038223. arXiv: 2006.10764 [astro-ph.GA].

[5] C. Bacchini et al. "Volumetric star formation laws of disc galaxies". In: 622, A64 (Feb. 2019), A64. DOI: 10.1051/0004-6361/201834382. arXiv: 1810.03616 [astro-ph.GA].

[6] S. A. Balbus and W. J. Potter. "Surprises in astrophysical gasdynamics". In: *Reports on Progress in Physics* 79.6, 066901 (June 2016), p. 066901. DOI: 10.1088/0034-4885/79/6/066901. arXiv: 1603.06489 [astro-ph.HE].

[7] S. Basu and T. C. Mouschovias. "Magnetic Braking, Ambipolar Diffusion, and the Formation of Cloud Cores and Protostars. I. Axisymmetric Solutions". In: 432 (Sept. 1994), p. 720. DOI: 10.1086/174611.

[8] M. Behrendt, A. Burkert, and M. Schartmann. "Structure formation in gas-rich galactic discs with finite thickness: from discs to rings". In: 448.1 (Mar. 2015), pp. 1007–1019. DOI: 10.1093/mnras/stv027. arXiv: 1408.5902 [astro-ph.GA].

[9] G. Bertin and S. Casertano. "Excitation of WARPS in galaxies - Fluid model of disk-halo interaction". In: 106.2 (Feb. 1982), pp. 274–286.

[10] J. Binney and S. Tremaine. *Galactic Dynamics: Second Edition*. 2008.

[11] P. F. Byrd and M. Friedman. "Handbook of Elliptic Integrals for Engineers and Physicists (Ref. U. Wegner)". In: *Mitteilungen der Astronomischen Gesellschaft Hamburg* 5 (Jan. 1954), p. 99.

[12] A. Cimatti, F. Fraternali, and C. Nipoti. *Introduction to Galaxy Formation and Evolution: From Primordial Gas to Present-Day Galaxies*. 2019.

[13] L. Ciotti and G. Bertin. "Analytical properties of the $R^{1/m}$ law". In: 352 (Dec. 1999), pp. 447–451. DOI: 10.48550/arXiv.astro-ph/9911078. arXiv: astro-ph/9911078 [astro-ph].

[14] P. Cuddeford. "On the potentials of galactic discs". In: 262.4 (June 1993), pp. 1076–1086.

[15] G. de Vaucouleurs. "Recherches sur les Nebuleuses Extragalactiques". In: *Annales d'Astrophysique* 11 (Jan. 1948), p. 247.

[16] P. Di Matteo et al. "Why the Milky Way's bulge is not only a bar formed from a cold thin disk". In: 577, A1 (May 2015), A1. DOI: 10.1051/0004-6361/201424457. arXiv: 1411.1416 [astro-ph.GA].

[17] D. B. Fisher et al. "Extreme Variation in Star Formation Efficiency across a Compact, Starburst Disk Galaxy". In: 928.2, 169 (Apr. 2022), p. 169. DOI: 10.3847/1538-4357/ac51c8. arXiv: 2202.00024 [astro-ph.GA].

[18] F. Fraternali et al. "Deep H I Survey of the Spiral Galaxy NGC 2403". In: 123.6 (June 2002), pp. 3124–3140. DOI: 10.1086/340358. arXiv: astro-ph/0203405 [astro-ph].

[19] S. Fujimoto et al. "Primordial Rotating Disk Composed of ≥15 Dense Star-Forming Clumps at Cosmic Dawn". In: *arXiv e-prints*, arXiv:2402.18543 (Feb. 2024), arXiv:2402.18543. DOI: 10.48550/arXiv.2402.18543. arXiv: 2402.18543 [astro-ph.GA].

[20] P. Goldreich and D. Lynden-Bell. "I. Gravitational stability of uniformly rotating disks". In: 130 (Jan. 1965), p. 97. DOI: 10.1093/mnras/130.2.97.

[21] P. Goldreich and D. Lynden-Bell. "II. Spiral arms as sheared gravitational instabilities". In: 130 (Jan. 1965), p. 125. DOI: 10.1093/mnras/130.2.125.

[22] L. Hernquist. "An Analytical Model for Spherical Galaxies and Bulges". In: 356 (June 1990), p. 359. DOI: 10.1086/168845.

[23] G. Iorio. *galpynamics*. 2018. URL: https://gitlab.com/iogiul/galpynamics.

[24] P. M. W. Kalberla et al. "Dark matter in the Milky Way. II. The HI gas distribution as a tracer of the gravitational potential". In: 469.2 (July 2007), pp. 511–527. DOI: 10.1051/0004-6361:20066362. arXiv: 0704.3925 [astro-ph].

[25] P. M. W. Kalberla et al. "The Leiden/Argentine/Bonn (LAB) Survey of Galactic HI. Final data release of the combined LDS and IAR surveys with improved stray-radiation corrections". In: 440.2 (Sept. 2005), pp. 775–782. DOI: 10.1051/0004-6361:20041864. arXiv: astro-ph/0504140 [astro-ph].

[26] R. C. Kennicutt Jr. "The Global Schmidt Law in Star-forming Galaxies". In: 498.2 (May 1998), pp. 541–552. DOI: 10.1086/305588. arXiv: astro-ph/9712213 [astro-ph].

[27] R. S. Klessen and P. Hennebelle. "Accretion-driven turbulence as universal process: galaxies, molecular clouds, and protostellar disks". In: 520, A17 (Sept. 2010), A17. DOI: 10.1051/0004-6361/200913780. arXiv: 0912.0288 [astro-ph.CO].

[28] K. Kratter and G. Lodato. "Gravitational Instabilities in Circumstellar Disks". In: 54 (Sept. 2016), pp. 271–311. DOI: 10.1146/annurev-astro-081915-023307. arXiv: 1603.01280 [astro-ph.SR].

[29] M. Kregel and P. C. van Der Kruit. "Structure and kinematics of edge-on galaxy discs – III. The rotation curves in the gas". In: *Monthly Notices of the Royal Astronomical Society* 352.3 (Aug. 2004), pp. 787–803. ISSN: 0035-8711. DOI: 10.1111/j.1365-2966.2004.07978.x. eprint: https://academic.oup.com/mnras/article-pdf/352/3/787/18489366/352-3-787.pdf. URL: https://doi.org/10.1111/j.1365-2966.2004.07978.x.

[30] C. J. Law et al. "CO Line Emission Surfaces and Vertical Structure in Midinclination Protoplanetary Disks". In: 932.2, 114 (June 2022), p. 114. DOI: 10.3847/1538-4357/ac6c02. arXiv: 2205.01776 [astro-ph.EP].

[31] F. Lelli et al. "A massive stellar bulge in a regularly rotating galaxy 1.2 billion years after the Big Bang". In: *Science* 371.6530 (Feb. 2021), pp. 713–716. DOI: 10.1126/science.abc1893. arXiv: 2102.05957 [astro-ph.GA].

[32] E. S. Levine, L. Blitz, and C. Heiles. "The Vertical Structure of the Outer Milky Way H I Disk". In: 643.2 (June 2006), pp. 881–896. DOI: 10.1086/503091. arXiv: astro-ph/0601697 [astro-ph].

[33] G. B. Lima Neto, D. Gerbal, and I. Márquez. "The specific entropy of elliptical galaxies: an explanation for profile-shape distance indicators?" In: 309.2 (Oct. 1999), pp. 481–495. DOI: 10.1046/j.1365-8711.1999.02849.x. arXiv: astro-ph/9905048 [astro-ph].

[34] G. R. Mamatsashvili and W. K. M. Rice. "Axisymmetric modes in vertically stratified self-gravitating discs". In: 406.3 (Aug. 2010), pp. 2050–2064. DOI: 10.1111/j.1365-2966.2010.16825.x. arXiv: 1004.1662 [astro-ph.EP].

[35] P. E. Mancera Piña et al. "A tight angular-momentum plane for disc galaxies". In: 651, L15 (July 2021), p. L15. DOI: 10.1051/0004-6361/202141574. arXiv: 2107.02809 [astro-ph.GA].

[36] P. E. Mancera Piña et al. "The impact of gas disc flaring on rotation curve decomposition and revisiting baryonic and dark matter relations for nearby galaxies". In: 514.3 (Aug. 2022), pp. 3329–3348. DOI: 10.1093/mnras/stac1508. arXiv: 2205.12977 [astro-ph.GA].

[37] A. Marasco et al. "Distribution and kinematics of atomic and molecular gas inside the solar circle". In: 607, A106 (Nov. 2017), A106. DOI: 10.1051/0004-6361/201731054. arXiv: 1707.00743 [astro-ph.GA].

[38] P. J. McMillan. "The mass distribution and gravitational potential of the Milky Way". In: 465.1 (Feb. 2017), pp. 76–94. DOI: 10.1093/mnras/stw2759. arXiv: 1608.00971 [astro-ph.GA].

[39] S. E. Meidt. "Molecular Clouds as Gravitational Instabilities in Rotating Disks: A Modified Stability Criterion". In: 937.2, 88 (Oct. 2022), p. 88. DOI: 10.3847/1538-4357/ac86ce. arXiv: 2208.01888 [astro-ph.GA].

[40] L. Mestel. "On the galactic law of rotation". In: 126 (Jan. 1963), p. 553. DOI: 10.1093/mnras/126.6.553.

[41] F. Nakamura and T. Hanawa. "Nonaxisymmetric Evolution of Dynamically Contracting Disks and Its Implication for Binary Formation". In: 480.2 (May 1997), pp. 701–704. DOI: 10.1086/304010.

[42] J. F. Navarro, C. S. Frenk, and S. D. M. White. "The Structure of Cold Dark Matter Halos". In: 462 (May 1996), p. 563. DOI: 10.1086/177173. arXiv: astro-ph/9508025 [astro-ph].

[43] C. Nipoti. "Local gravitational instability of stratified rotating fluids: three-dimensional criteria for gaseous discs". In: 518.4 (Feb. 2023), pp. 5154–5162. DOI: 10.1093/mnras/stac3403. arXiv: 2211.09831 [astro-ph.GA].

[44] C. Nipoti, C. Caprioglio, and C. Bacchini. "Local gravitational instability of two-component thick discs in three dimensions". In: 689, A61 (Sept. 2024), A61. DOI: 10.1051/0004-6361/202450462. arXiv: 2405.13123 [astro-ph.GA].

[45] R. P. Olling. "On the Usage of Flaring Gas Layers to Determine the Shape of Dark Matter Halos". In: 110 (Aug. 1995), p. 591. DOI: 10.1086/117545. arXiv: astro-ph/9505002 [astro-ph].

[46] R. P. Olling and M. R. Merrifield. "Two measures of the shape of the dark halo of the Milky Way". In: 311.2 (Jan. 2000), pp. 361–369. DOI: 10.1046/j.1365-8711.2000.03053.x. arXiv: astro-ph/9907353 [astro-ph].

[47] H. C. Plummer. "On the problem of distribution in globular star clusters". In: 71 (Mar. 1911), pp. 460–470. DOI: 10.1093/mnras/71.5.460.

[48] F. Rizzo et al. "The ALMA-ALPAKA survey. I. High-resolution CO and [CI] kinematics of star-forming galaxies at z = 0.5-3.5". In: 679, A129 (Nov. 2023), A129. DOI: 10.1051/0004-6361/202346444. arXiv: 2303.16227 [astro-ph.GA].

[49] A. B. Romeo. "From massive spirals to dwarf irregulars: a new set of tight scaling relations for cold gas and stars driven by disc gravitational instability". In: 491.4 (Feb. 2020), pp. 4843–4851. DOI: 10.1093/mnras/stz3367. arXiv: 1905.05752 [astro-ph.GA].

[50] A. B. Romeo and N. Falstad. "A simple and accurate approximation for the Q stability parameter in multicomponent and realistically thick discs". In: 433.2 (Aug. 2013), pp. 1389–1397. DOI: 10.1093/mnras/stt809. arXiv: 1302.4291 [astro-ph.CO].

[51] F. Schmitz. "The stability of a differentially rotating thin disk". In: 200.1-2 (July 1988), pp. 120–126.

[52] J.-L. Tassoul. *Theory of rotating stars*. 1978.

[53] B. Terzić and A. W. Graham. "Density-potential pairs for spherical stellar systems with Sérsic light profiles and (optional) power-law cores". In: 362.1 (Sept. 2005), pp. 197–212. DOI: 10.1111/j.1365-2966.2005.09269.x. arXiv: astro-ph/0506192 [astro-ph].

[54] A. Toomre. "On the gravitational stability of a disk of stars." In: 139 (May 1964), pp. 1217–1238. DOI: 10.1086/147861.

[55] T. S. van Albada et al. "Distribution of dark matter in the spiral galaxy NGC 3198." In: 295 (Aug. 1985), pp. 305–313. DOI: 10.1086/163375.

[56] P. C. van der Kruit and L. Searle. “Surface photometry of edge-on spiral galaxies. I - A model for the three-dimensional distribution of light in galactic disks.” In: 95 (Feb. 1981), pp. 105–115.

[57] P. Virtanen et al. “SciPy 1.0: Fundamental Algorithms for Scientific Computing in Python”. In: *Nature Methods* 17 (2020), pp. 261–272. DOI: 10.1038/s41592-019-0686-2.

[58] H.-H. Wang et al. “Equilibrium initialization and stability of three-dimensional gas discs”. In: 407.2 (Sept. 2010), pp. 705–720. DOI: 10.1111/j.1365-2966.2010.16942.x. arXiv: 1004.5593 [astro-ph.GA].

[59] K. Yim et al. “The Interstellar Medium and Star Formation in Edge-On Galaxies. II. NGC 4157, 4565, and 5907”. In: 148.6, 127 (Dec. 2014), p. 127. DOI: 10.1088/0004-6256/148/6/127. arXiv: 1408.5905 [astro-ph.GA].

Appendix A

The best choice to find the vertical density profile

To find the normalized vertical density distribution we first need a method to solve the integral in Eq. (2.2.4). To do this, we use the SciPy[57] submodule `scipy.integrate`. The two best working methods for our case are `cumulative_simpson` and `quad`.
We evaluate the normalized density vertical profile $\tilde{\rho} = \rho(R, z)/\rho(R, 0)$ using a model consisting of an halo with a Navarro-Frank-White density profile, a bulge with a Hernquist profile, and a stellar disk with finite thickness and exponential profile and no self-gravity: here we try to replicate the iter-0 of `galpynamics` submodule `discHeight` relative to a massless disc, where the potential is calculated ignoring the presence of the gas disc.
For the velocity dispersion, we choose the following formulation:

$$\sigma(R, z) = 10e^{-R/a} g(z) \text{ km s}^{-1}. \tag{A.0.1}$$

While the code allows $g(z)$ to be in any form, for the purpose of our test we selected the following four functions:

$$g_1(z) = \exp\left(-\tfrac{z}{b}\right), \tag{A.0.2}$$
$$g_2(z) = \exp\left(\tfrac{z}{b}\right), \tag{A.0.3}$$
$$g_3(z) = -\tfrac{z}{b}, \tag{A.0.4}$$
$$g_4(z) = +\tfrac{z}{b}. \tag{A.0.5}$$

A.1 First test: numerical errors on the integration by parts

While Eq. (2.2.4) and Eq. (2.2.1d) are mathematically the same, they might give slightly different results due to numerical errors. For a first test, we try using both methods with both Eq. (2.2.4) and Eq. (2.2.1d) at a fixed R. We test our model at $R = 5$ and 30 kpc, while for a and b we use either 20 or 30 kpc.

We show in Fig. A.1 the residuals obtained for every functional form of $g(z)$ with $R = 30$ kpc, $a = 30$ kpc, and $b = 20$ kpc. We can see how, for a given formulation of the velocity dispersion and regardless of the used method, both equations give extremely similar results, especially at low values of z. We do expect the relative error to grow with the vertical coordinate: this is because the density reaches very low values at higher z, which naturally translates in bigger errors since we are dealing with small numbers. In Fig. A.2 we show the residuals obtained with $g(z) = e^{-z/b}$ for different values of R, a, and b, and once again we can see that, for a given combination, the relative errors between the two equations are minimal.

This means that adding the integration by parts does not cause additional problems from a numerical point of view.

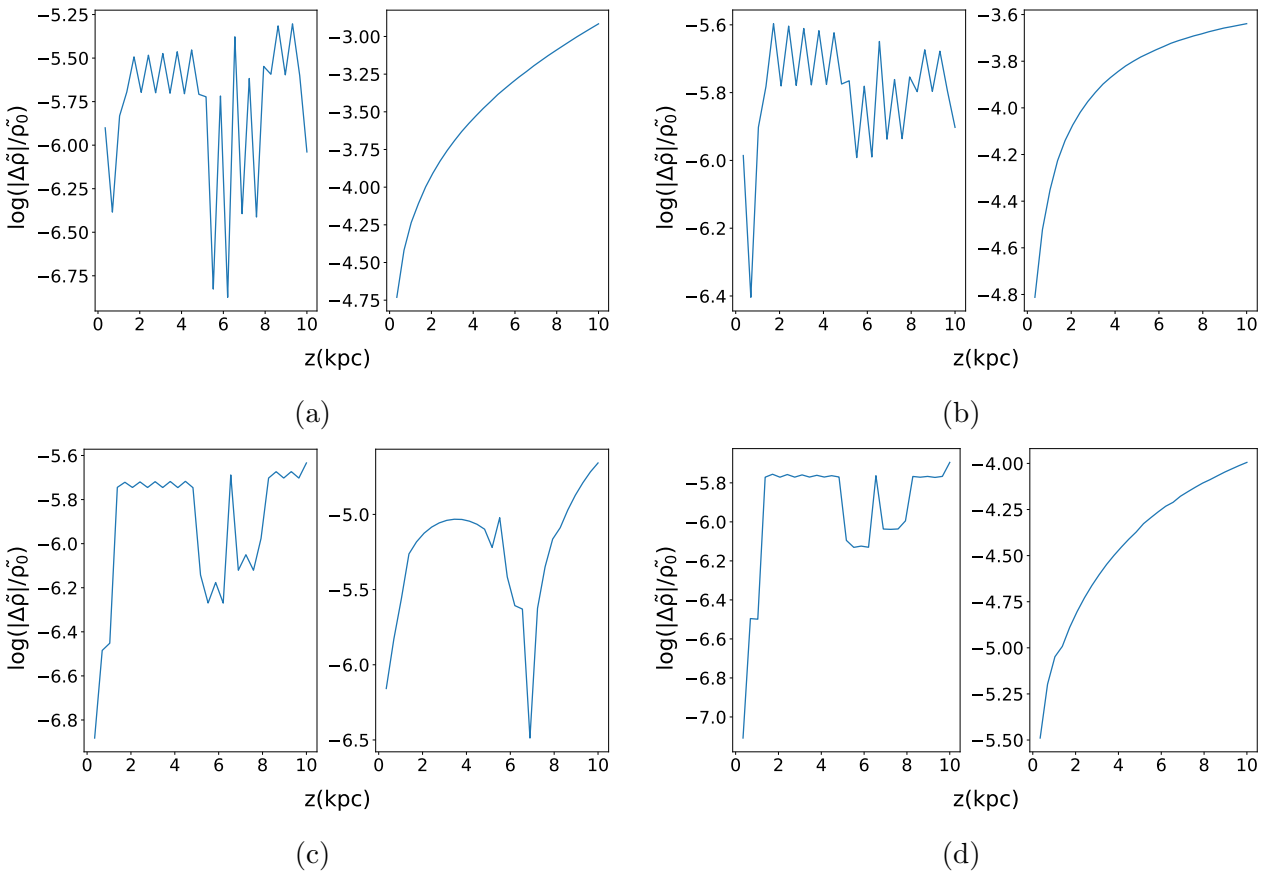

Figure A.1: $\log\left(\frac{|\tilde{\rho}_0-\tilde{\rho}_1|}{\tilde{\rho}_0}\right)$ with a velocity dispersion $\sigma(R,z) = 10e^{-R/a}g(z)$. With $\tilde{\rho}_0$ we refer to the values of the density found using Eq. (2.2.4), while $\tilde{\rho}_1$ refers to Eq. (2.2.1d). In all the four pictures the ones on the leftside are found using the `cumulative_simpson` method, while the ones on the rightside are found with `quad`. For all pictures: $R = 30$ kpc, $a = 30$ kpc and $b = 20$ kpc. (a): $g(z) = e^{-z/b}$; (b): $g(z) = e^{z/b}$; (c): $g(z) = -(z/b)$; (d): $g(z) = +(z/b)$.

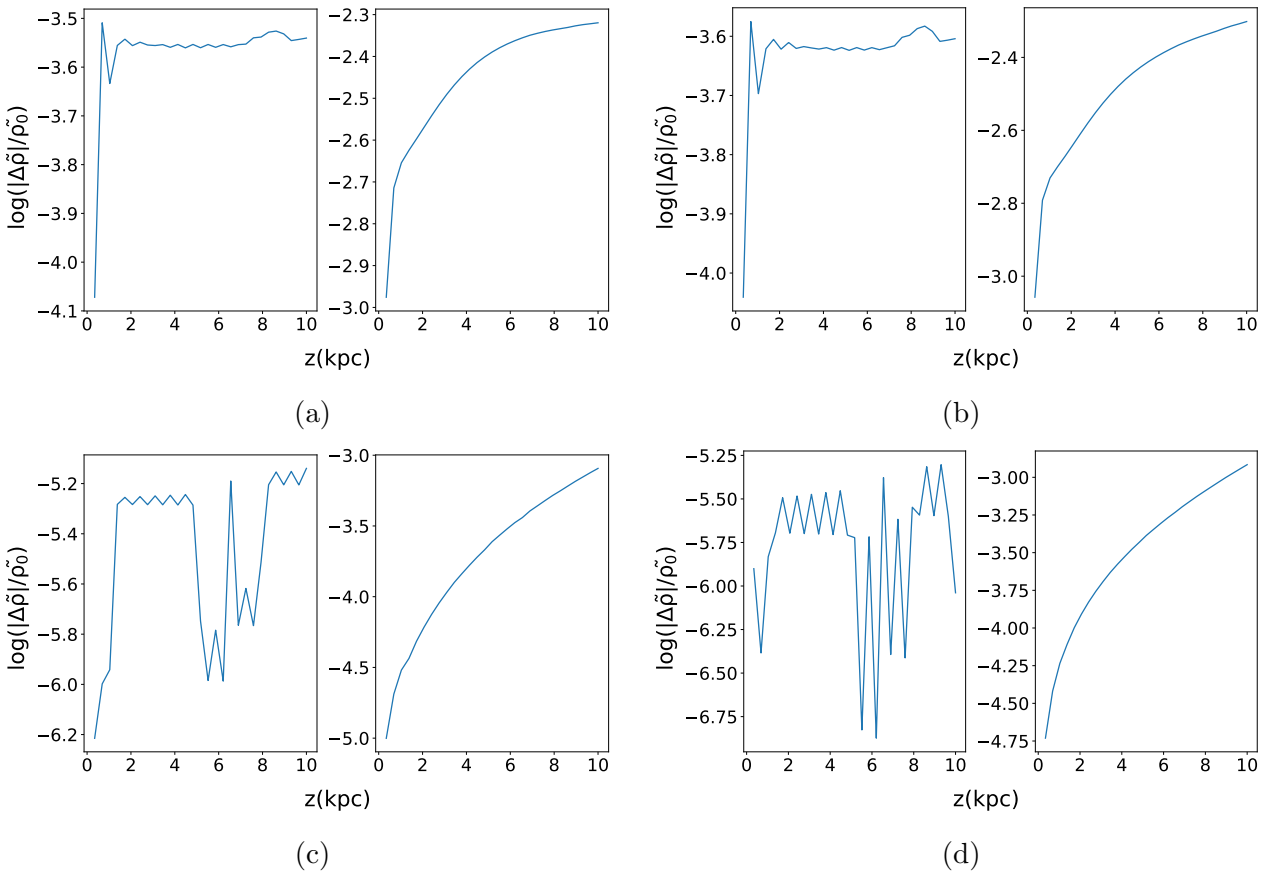

Figure A.2: Same as Fig. A.1, but with $g(z) = e^{-z/b}$ for all pictures. The parameters are: $R = 5$ kpc in Figs. A.2a–A.2b, $R = 30$ kpc in Figs. A.2c–A.2d, $a = 20$ kpc and $b = 30$ kpc in Fig. A.2a and Fig. A.2c, $a = 30$ kpc and $b = 20$ kpc in Fig. A.2b and Fig. A.2d.

A.2 What is the best method?

We now need to determine which method between `cumulative_simpson` and `quad` works best for us. From now on, we use $g(z) = e^{z/b}$, with $a = 20$ kpc and $b = 30$ kpc.

First, we need to check if we get the same profiles at every R, so we calculate the density over a linear interval of 30 points of R, going from 0.01 to 30 kpc. In Fig. A.3 we show the relative error between the two methods obtained at different values of R, and we can see how we obtain pretty small discrepancies.

We then verify which one is the fastest: `cumulative_simpson` is the best one, with an average execution time of 0.03 s, while `quad` has an average of 4.11 s, 137 times slower than the other.

We now want to check the errors associated with each method; while `quad` prints its own error, to find the one for `cumulative_simpson` we used the formula:

$$\text{absolute error} = \frac{1}{180} h^4 (z_{cut} - z_0) \max_{z \in [z_0, z_{cut}]} \left| f^{(4)}(z) \right|, \tag{A.2.1}$$

where $h = \frac{(z_{cut} - z_0)}{n}$, where n is the number of subintervals, while f^4 is the fourth derivative of the function in the integral, found using the following expression:

$$f^4(z) \cong \frac{f(z_{-2}) - 4f(z_{-1}) + 6f(z_0) - 4f(z_1) + f(z_2)}{h^4}. \tag{A.2.2}$$

In Table A.1 we report the absolute errors associated with each method, and it can be seen how both are pretty low, with `quad` performing better at lower values of R. Due to `cumulative_simpson` being faster and having lower relative errors, as shown in Appendix A.1, we choose it as our method.

R (kpc)	`cumulative_simpson`	error	`quad`	error
1.00000e-02	-4.85339e+00	2.61771e-05	-4.85413e+00	3.41988e-06
3.11241e+00	-5.96441e+00	3.74526e-05	-5.96402e+00	2.12823e-07
6.21483e+00	-7.10454e+00	1.92825e-05	-7.10424e+00	3.56336e-06
9.31724e+00	-8.52668e+00	9.45576e-06	-8.52645e+00	1.65549e-06
1.24197e+01	-1.03590e+01	4.59882e-06	-1.03588e+01	1.34352e-06
1.55221e+01	-1.27321e+01	2.22478e-06	-1.27319e+01	7.99286e-07
1.86245e+01	-1.58055e+01	1.05581e-06	-1.58054e+01	6.07058e-08
2.17269e+01	-1.97850e+01	5.06180e-07	-1.97850e+01	1.20567e-07
2.48293e+01	-2.49395e+01	2.17190e-07	-2.49395e+01	3.65515e-07
2.79317e+01	-3.16213e+01	6.87012e-08	-3.16214e+01	3.55507e-07
3.00000e+01	-3.71472e+01	5.00571e-08	-3.71472e+01	3.92891e-07

Table A.1: The value of the integral with its associated error calculated at $z = 10$ kpc with `cumulative_simpson` and `quad` for different values of R.

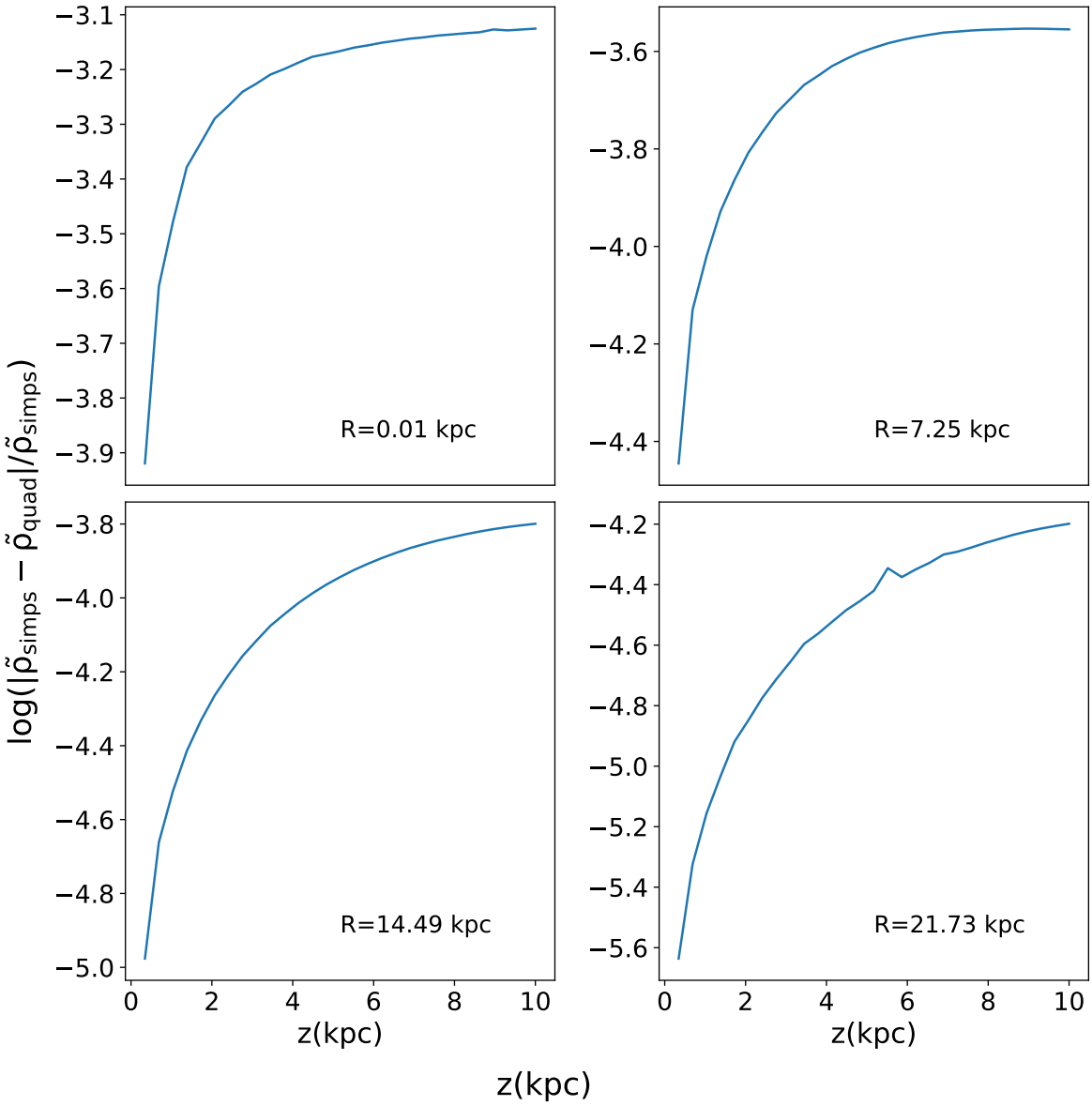

Figure A.3: $\log\left(\frac{|\tilde{\rho}_{simps}-\tilde{\rho}_{quad}|}{\tilde{\rho}_{simps}}\right)$ at different values of R, with a velocity dispersion $\sigma(R,z) = 10e^{-R/a}e^{z/b}$, with $a = 20$ kpc and $b = 30$ kpc.